Summer 2017

EMI measurement and modeling techniques for complex electronic circuits and modules

Satyajeet Shinde

Department: Electrical and Computer Engineering

EMI MEASUREMENT AND MODELING TECHNIQUES FOR COMPLEX ELECTRONIC CIRCUITS AND MODULES

by

SATYAJEET SHINDE

A DISSERTATION

Presented to the Faculty of the Graduate School of the

MISSOURI UNIVERSITY OF SCIENCE AND TECHNOLOGY

In Partial Fulfillment of the Requirements for the Degree

DOCTOR OF PHILOSOPHY
in
ELECTRICAL ENGINEERING

2017

Approved
David J. Pommerenke, Advisor
Victor Khilkevich
Jun Fan
Daryl Beetner
Daniel Stutts

PUBLICATION DISSERTATION OPTION

This dissertation consists of the following four articles, formatted in the style used by the Missouri University of Science and Technology:

Paper I: Pages 3-36 have been accepted by IEEE Transactions on EMC.

Paper II: Pages 37-51 have been accepted by IEEE Transactions on EMC.

Paper III: Pages 52-81 have been submitted to IEEE Transactions on Instrumentation and Measurement.

Paper IV: Pages 82-111 are intended for submission to IEEE Transactions on EMC.

ABSTRACT

This dissertation consists of four papers. In the first paper, a combined model for predicting the most critical radiated emissions and total radiated power due to the display signals in a TV by incorporating the main processing board using the Huygens Equivalence theorem and the radiation due to the flex cable based on active probe measurements was developed.

In the second paper, a frequency-tunable resonant magnetic field probe was designed in the frequency range 900-2260 MHz for near-field scanning applications for the radio frequency interference studies by using a varactor diode providing the required capacitance and the parasitic inductance of a magnetic field loop (i.e., a parallel *LC* circuit). Measurement results showed good agreement with the simulated results.

In the third paper, a wideband microwave method was developed as a means for rapid detection of slight dissimilarities (including counterfeit) and aging effects in integrated circuits (ICs) based on measuring the complex reflection coefficient of an IC when illuminated with an open-ended rectangular waveguide probe, at K-band (18-26.5 GHz) and Ka-band (26.5-40 GHz) microwave frequencies.

In the fourth paper, a method to predict radiated emissions from DC-DC converters with cables attached on the input side to a LISN and on the output side to a DC brushless motor as load based on linear terminal equivalent circuit modeling was demonstrated. The linear terminal equivalent model was extracted using measured input and output side common mode currents for various characterization impedances connected at the input and output terminals of the converter.

ACKNOWLEDGMENTS

I would like to express my sincere gratitude to Dr. David Pommerenke, my advisor, for his guidance and instruction on my research work, financial support to my study and direction for this dissertation during my pursuit of the PhD's degree. I learned not only academic knowledge, but also the rigorous attitude, good manners, and courage to face difficulties.

I would like to sincerely thank Kohei Masuda from Panasonic Corp. for his constant support, help and guidance on the projects and publications.

I would like to thank the committee members, Dr. Victor Khilkevich, Dr. Jun Fan, Dr. Daryl Beetner and Dr. Daniel Stutts, for their teaching in my courses, discussions related to my research, and helpful suggestions on my dissertation.

I would also like to express my thanks to all the other faculty members and students in and out of the EMC lab for their team work and help in my coursework and research.

Finally, my heartfelt gratitude goes to my parents, my sister and friends for their support and encouragement towards achieving this goal.

TABLE OF CONTENTS

LIST OF ILLUSTRATIONS

Figure Page

PAPER I

LIST OF TABLES

SECTION

1. INTRODUCTION

This dissertation consists of four papers, which cover emissions modeling for a complex electronic product, the design and an equivalent circuit model for a frequency tunable H-field probe, measurement method for rapid detection of dissimilar and aging ICs and radiated emissions prediction using terminal equivalent modeling.

In the first paper, a combined model for predicting the most critical radiated emissions and total radiated power due to the display signals in a TV by incorporating the main processing board using the Huygens Equivalence theorem and the radiation due to the flex cable based on active probe measurements was developed.

In the second paper, a frequency-tunable resonant magnetic field probe was designed in the frequency range 900-2260 MHz for near-field scanning applications for the radio frequency interference studies by using a varactor diode providing the required capacitance and the parasitic inductance of a magnetic field loop (i.e., a parallel *LC* circuit). The measured frequency response and sensitivity over a microstrip trace using the fabricated probe showed good agreement with the simulated results of the equivalent circuit model and the full-wave simulation model.

In the third paper, a wideband microwave method was developed as a means for rapid detection of slight dissimilarities (including counterfeit) and aging effects in integrated circuits (ICs) based on measuring the complex reflection coefficient of an IC when illuminated with an open-ended rectangular waveguide probe, at K-band (18-26.5 GHz) and Ka-band (26.5-40 GHz) microwave frequencies.

In the fourth paper, a method to predict radiated emissions from DC-DC converters with cables attached on the input side to a LISN and on the output side to a DC brushless motor as load based on linear terminal equivalent circuit modeling was demonstrated. The linear terminal equivalent model was extracted using measured input and output side common mode currents for various characterization impedances connected at the input and output terminals of the converter.

The primary contributions of this dissertation include:

- A combined full-wave simulation model using advanced methods for predicting radiated EMI due to display signals in a complex electronic product - TV (Paper I).
- A frequency-tunable resonant probe (900 – 2260 MHz) was designed and modeled having 7-8 dB higher sensitivity as compared to an equivalently-sized broadband H-field probe (Paper II).
- A novel method based on wideband microwave reflectometry for rapid detection of slightly dissimilar (including counterfeit) and aging ICs. (Paper III).
- A methodology to predict the radiated emissions from DC-DC converters with attached cables based on terminal equivalent modeling (Paper IV).

PAPER

I. MODELING EMI DUE TO DISPLAY SIGNALS IN A TV

Satyajeet Shinde, *Student Member, IEEE,* Xu Gao, Kohei Masuda, *Member, IEEE,* Victor Khilkevich, *Senior Member, IEEE,* David Pommerenke, *Fellow, IEEE*

ABSTRACT

Modeling the electromagnetic emissions from a complex product such as a TV presents many challenges due to the complexity of electromagnetic interaction between multiple noise sources and interconnected resonant structures. A set of advanced methods such as the design and use of substitution boards for EMI analysis, a practical simulation model for verifying the accuracy of the passive structures of the TV, an empirical scaling factor for incorporating the main processing board using the Huygens Equivalence theorem and modeling the radiation due to the flex cable based on active probe measurements is presented. The combined model comprised of the relevant noise sources and structures allowed the prediction of the most critical radiated emissions and the total radiated power caused due to the display signals.

Index Terms— Huygens Equivalence Theorem, radiated emissions, substitution boards, simulation model, multiple noise sources, total radiated power, TV.

1. INTRODUCTION

EMI analysis and prediction of radiated emissions from electronic products is often desirable to predict a product's compliance to EMC regulation standards and to understand noise coupling mechanisms within the product. For complex systems consisting of multiple noise sources and resonant structures, such as a TV, accurate analysis and prediction of EMI using analytical methods is almost impossible. Full wave electromagnetic solvers are often used for modeling such complex systems. However the process of creating and verifying the models is seldom simple involving accurate measurements of the relevant noise sources and the system geometry. Additionally, composites and alloys are widely used for making chassis and other components in commercial products. The electromagnetic properties of such composites and alloys may not always be known requiring additional empirical methods to assign effective electromagnetic properties for modeling. This paper presents a combination of methods used for modeling the radiated emissions due to the display signals (LVDS) in a TV. A typical TV consists of multiple electronic sub-systems such as the main audio-video processing board, power supply boards, the LCD itself, LED backlight arrays, LCD driver boards, etc. and multiple electrically large structures such as printed circuit boards, flex cables, metallic chassis parts such as the back panel, back cover, etc., as shown in Figure 1.1. The display signals are driven by the main processing board to the distribution boards on the LCD via the flex cables that are routed over the metal back panel. In such a system, the electromagnetic energy can be coupled between various sub-systems via multiple coupling paths.

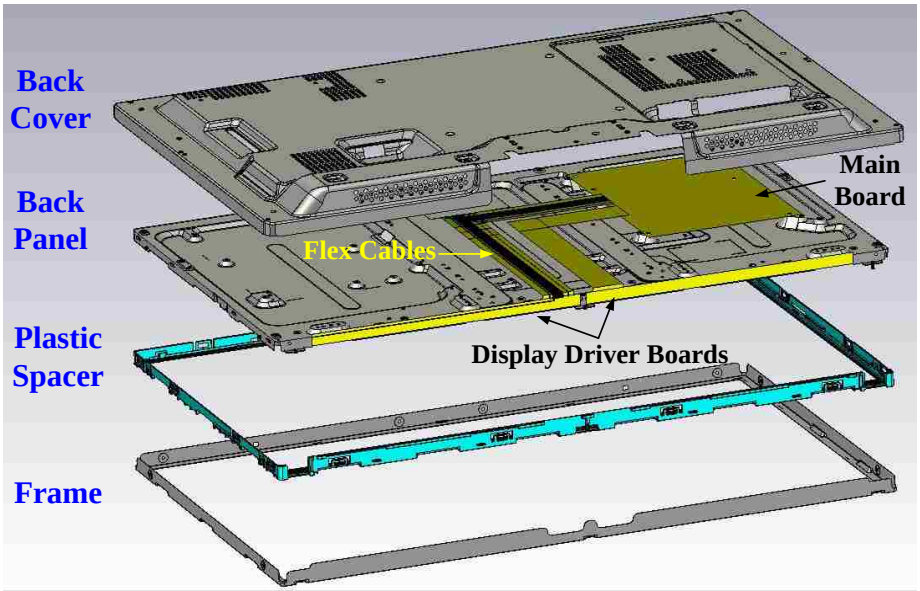

Figure 1.1 Some of the main parts of the LCD TV used for analysis and modeling.

The methods used for the EMI analysis and for modeling of the radiated emissions from the TV are listed as follows:

- Selective shielding while observing the radiation pattern for identifying radiating structures.
- Passive substitution boards for identifying the EMI contribution due to the LCD display. Passive substitution boards were designed to enable the normal operation of the TV display signals when the LCD is disconnected from the flex cables. The signal loading by the LCD is replaced by the substitution boards.
- A practical simulation model for verifying the accuracy of the passive structures and for obtaining the effective conductivity of the metal parts and the effective dielectric constant for the plastic spacer in the TV.

- A multi-step process for incorporating the main processing board using the Surface Equivalence Theorem [1]-[2]. In [3]-[5], the impressed sources were calculated according to Huygens's Equivalence Principle from the NFS data.
- The Huygens Equivalent source of the main board was obtained by measuring only the phase-resolved tangential H-fields and filling the box with PMC to calculate the tangential electric fields on the surface (Love's Theorem [8]). The main board and its mounting geometry were included within the Huygens box to account for scattering between the main board and the back cover.
- Use of an empirical magnitude correction factor for modeling the main processing board using the Huygens Equivalence principle.
- Modeling the flex cable currents using the Keysight N2752A active differential probe [6] for measuring the common mode and differential mode voltages on the flex cable traces.
- Combination of the two noise source models and relevant structures to predict the radiated emissions due to the display signals.

2. TEST SETUP FOR RADIATED EMISSIONS MEASUREMENTS

The test setup for measuring the radiated emissions from the original TV is shown in Figure 2.1. The measurements on the original TV, without any changes or modifications to the chassis or internal components, will be referred to as baseline measurements henceforth. For obtaining maximal emission values the turn table was rotated from 0 to 360 degrees in 10 degree increments using max hold mode. The measurement was performed for two test cases: one with the original DUT and one with the metal back cover removed. An estimate of the shielding effectiveness of the metal back cover is obtained by comparing the results of the two test cases. The measured data for the two test cases is post-processed to plot the maximized radiation from 30 MHz to 1000 MHz over all angles of the turntable rotation, for both polarizations, as shown in Figure 2.1.

The complexity of the EMI of electrically large structures with many gaps becomes apparent if the change in the EMI levels is observed when compared to that of the TV with its back-cover removed. The strongest emissions around 540 MHz are of most interest. Additionally, in vertical polarization, removing the back cover reduces the emissions by 15 dB. To analyze this counterintuitive observation, the radiated patterns for the two test cases are compared at 540 MHz as shown in Figure 2.2. Figure 2.2.-b, demonstrates that the presence of the back cover causes increased emissions from the angles 330 to 60 degrees (front side of the TV) and from 150 to 240 degrees (back side of the TV) in the vertical polarization.

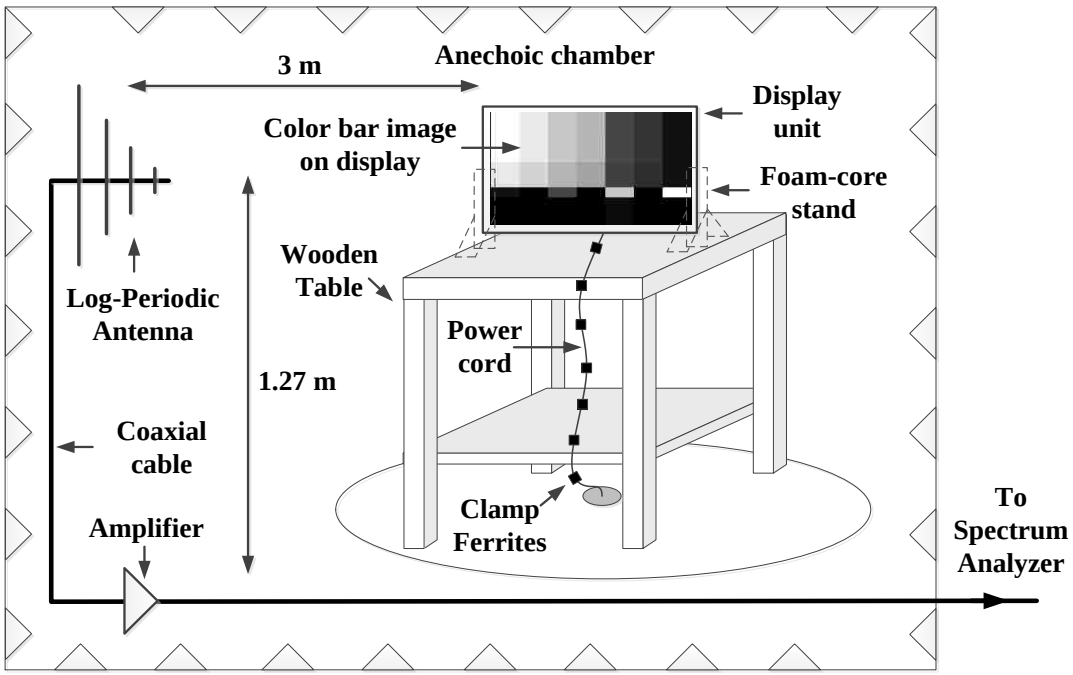

Figure 2.1 Test setup used to measure radiated emissions from the TV.

Additionally, the total radiated power from the TV is measured inside a reverberation chamber. Figure 2.3 shows the comparison between the total radiated powers for the two cases. The result shows that the total radiated power at 540 MHz is lower by about 5 dB when the back cover is present. This indicates that the back cover acts like a shield for radiations from the TV in general, but it also enhances the radiated vertical field component. The results from the measurements in the anechoic chamber show that the presence of the back cover increases the radiation in the vertical polarization at 540 MHz and in certain direction even though the total radiated power is lower.

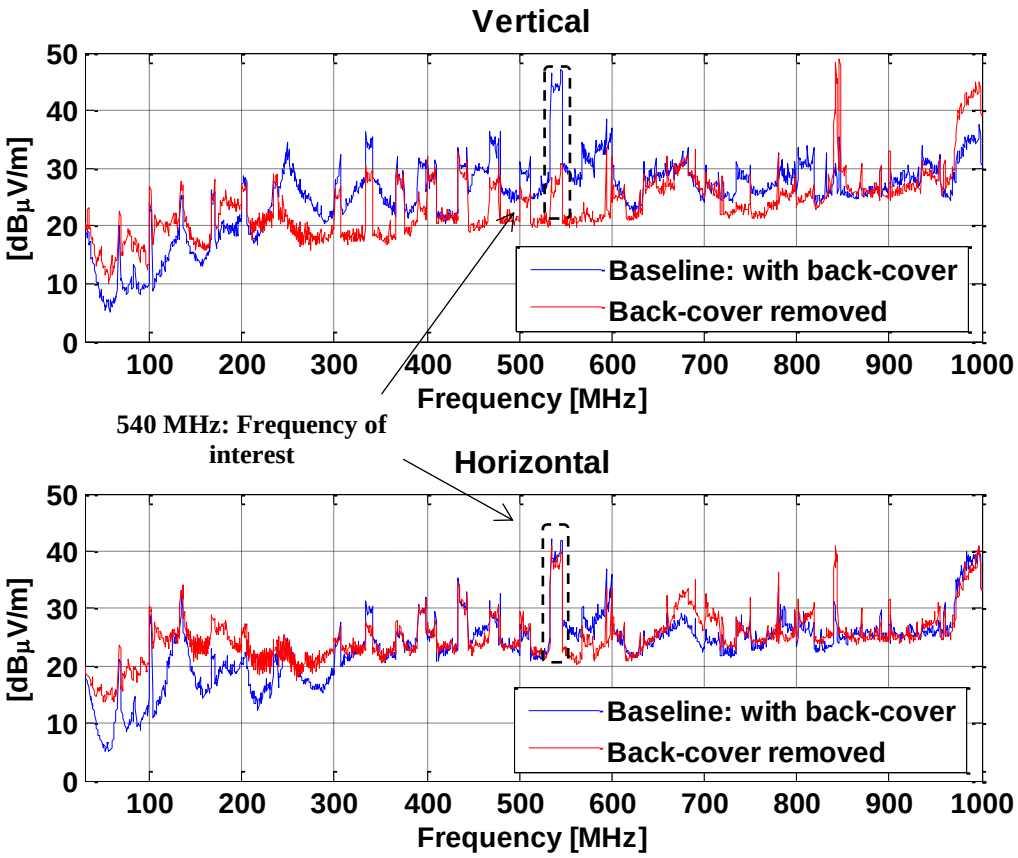

Figure 2.2 Comparison of the maximized radiated emissions for the TV, with and without the back cover for both polarizations.

Correlating the radiation patterns to the TV's geometry, indicates that the increase in the radiation in the front and back side might be a result of the noise voltage between the front and lower horizontal gaps between the back cover and the back panel. To confirm this mechanism, a selective shielding test was carried out.

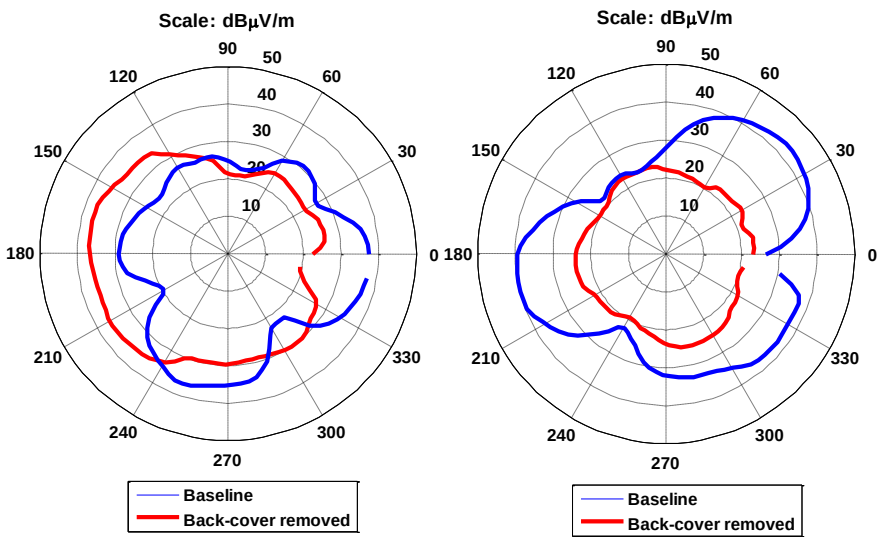

(a) Horizontal polarization (b) Vertical polarization

Figure 2.3 Comparison of the radiation patterns at 540 MHz between the baseline and with the back cover removed for both polarizations.

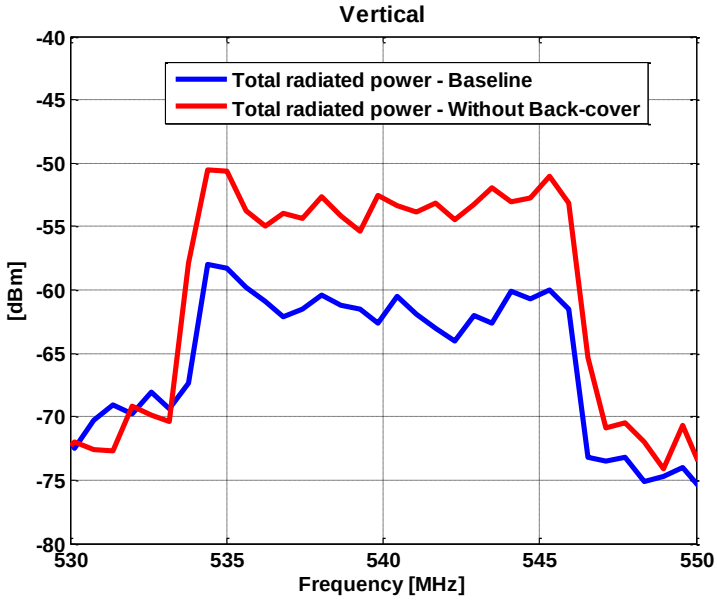

Figure 2.4 Comparison of the total radiated power measured with and without the back cover inside the reverberation chamber. Note the usage of a spread spectrum clock.

3. EMI ANALYSIS

3.1 SELECTIVE SHIELDING: EFFECT OF GAPS

The selective shielding test was conducted by covering the front side and lower side gaps with conductive copper tape (Figure 3.1.). This reduced the noise voltages across the front and bottom gaps significantly. Figure 3.2, shows the comparison of the radiated emissions pattern between the base line condition and when the front and lower gaps were covered with copper tape. The results show a decrease in the radiated emissions in the main lobes at 45, 210 and 310 degrees in the vertical polarization of the receiving antenna. This selective shielding test indicates that the front and lower gaps contribute to the increase in radiation with the back cover in the vertical polarization.

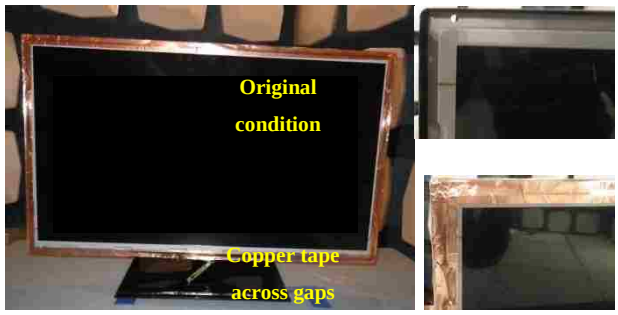

Figure 3.1 The TV with the front gaps between the back cover and the back panel covered with copper tape.

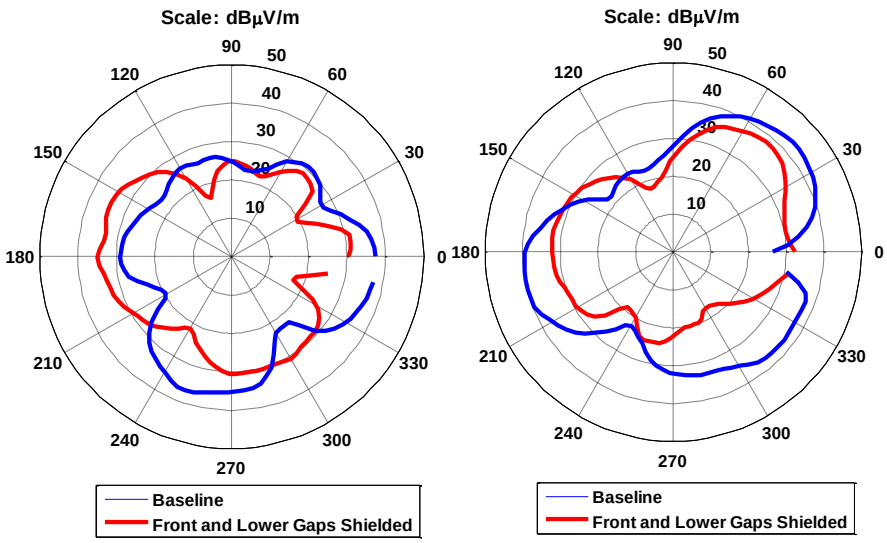

(a) Horizontal polarization (b) Vertical polarization

Figure 3.2 Comparison of the radiation patterns at 540 MHz between the baseline and with the front and lower gaps covered with copper tape for the (b) vertical and (a) horizontal polarizations of the receiving antenna.

3.2 SUBSTITUTION BOARDS

Estimating contribution of different components of an electronic product to the radiated emissions is usually an important goal of EMC analysis. This can be carried out by either physically removing the component, turning off a particular signal or by turning off power to the component. To estimate the contribution of the LCD and the display signal distribution boards (the LVDS signals are passed via the flex cable, to a distribution board and then connect to the LCD via 5 short flex cables at five different, equally spaced locations) in the TV, substitution boards are constructed to replace the LCD display load and distribution boards. The substitution boards provide the same common and differential mode load to the signals carried by the flex cable, but they do not connect to the LCD. They are similar to the original distribution boards in that they

are passive and contain the LVDS trace pairs with termination, and ground connecting metal brackets to emulate the brackets on the original display signal distribution boards.

The substitution boards serve as dummy boards which allow the main board to transmit display signals as in the original condition even though the LCD is disconnected. The substitution boards do not contain any active switching components and therefore do not create any additional signals. Figure 3.3. shows the comparison between the maximized radiated emissions around 540 MHz for the baseline case and with the substitution boards. The levels are very similar indicating no significant contribution from the LCD or the display distribution boards. Figure 3.4 shows the original boards and the constructed substitution boards. The usage of substitution boards allowed to conclude that modeling the LCD or the noise from the display distribution boards is not needed for estimating radiated emissions at 540 MHz from this TV set.

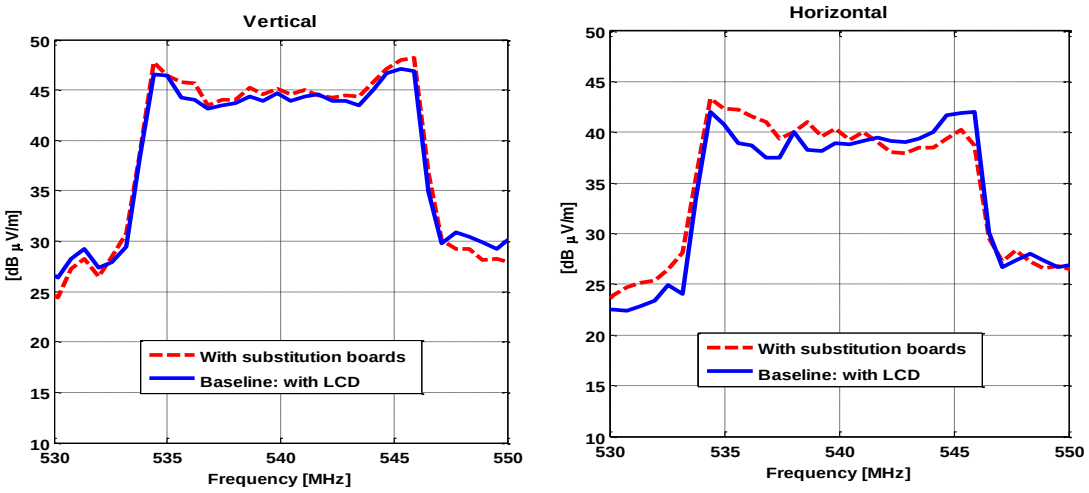

Figure 3.3 Comparison of the maximized radiated emissions between the baseline and the unit with the substitution driver boards for the vertical and horizontal polarizations of the receiving antenna.

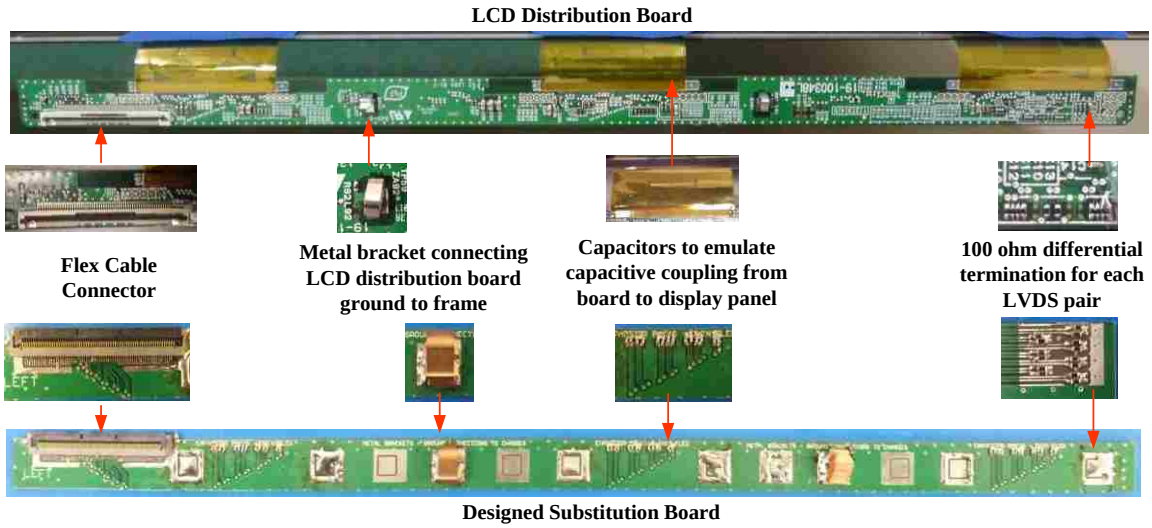

Figure 3.4 Photos of the original LCD distribution board and the designed substitution board.

4. FULL WAVE SIMULATION MODEL

For the frequency spectrum of interest, multiple components inside the TV such as the main board, flex cables, LCD distribution boards and parts of the chassis such as the back panel, back cover, etc. are electrically large. It is difficult to formulate analytical models or equivalent circuits for a system with multiple arbitrarily shaped geometries. The field distribution inside such a system is highly sensitive to the connection and coupling between the components. A full wave solution is needed. For the full wave modeling, the CAD models of the chassis components – back cover, back panel, screws, etc. are imported into the commercial full wave simulation tool – CST microwave studio [7]. The effective conductivity of the metal parts and the dielectric properties of the plastic spacer between the frame and the back panel are unknown. To assign material properties to the imported CAD models of the chassis components and verify the simulations settings, a simplified simulation model was created. The model consists of all the chassis elements, a copper metal board with the same dimensions as that of the original main board, a copper patch 50 x 70 mm with FR-4 dielectric at a height of 1.6 mm above the copper main board. The resonant frequency of the copper patch is much higher than the upper limit of the measurement (1 GHz). The copper patch is excited with the copper metal board as the reference with a 50 ohm discrete port (Figure 4.1). Far-field probes are setup at 3 m away from the model in a horizontal plane that cuts through the center of the model from 0 to 360 degrees in 10 degree steps.

The model is simulated using the time domain solver in CST for the frequency range 30 MHz to 1000 MHz A similar structure is constructed for validation of the simulation model result with measurement. In the measurement, the patch is excited with a 50 ohm coaxial cable connected to the tracking generator of a spectrum analyzer in the frequency range 30 MHz to 1000 MHz as shown in Figure 4.1.

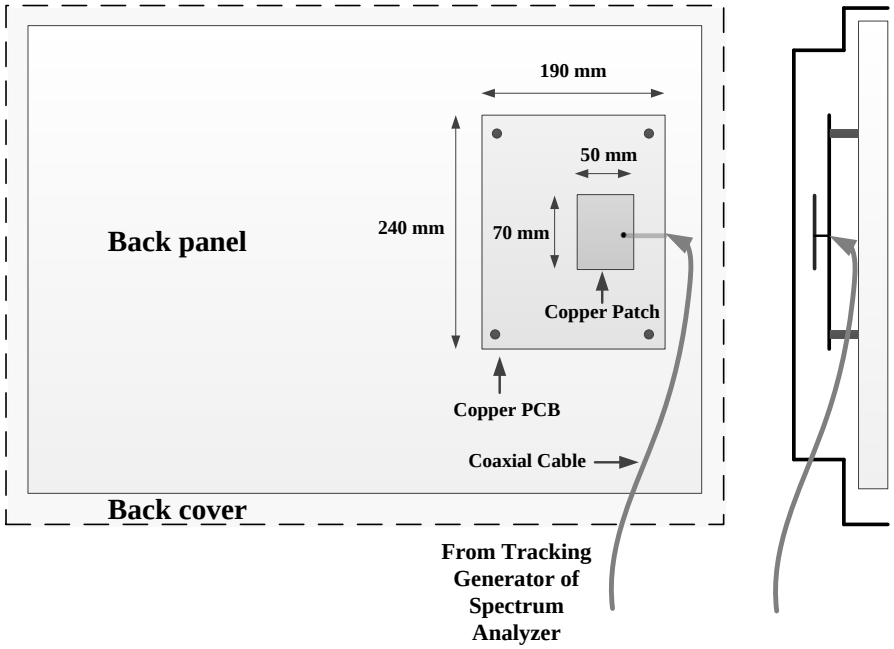

a) (b)

Figure 4.1 Test setup for radiated emissions measurements using broadband RF injection in to the patch board. (a) Front view, (b) side view.

Multiple ferrites suppress the common mode current on the cable such that it does not need to be modelled. The radiated emissions resulting from this broadband RF injection at the patch are measured using a similar setup to the one shown in Figure 2.1. The simulated far-field emissions were compared with the measured far-fields and the

material conductivities of the chassis and the dielectric constant (ε_r) of the plastic spacer were optimized iteratively to 59700 S/m and 2.1 respectively. The low conductivity is in line with our experience.

Prior experience with modeling of multiple complex electronic systems has shown that the effective conductivity of metal parts if often much lower than the bulk conductivity of the materials. Using the bulk conductivity usually leads to unreasonably high Q-factors. The comparison between the simulated and measured maximized far-fields and patterns at 540 MHz, for horizontal and vertical polarizations of the receiving antenna are shown in Figure 4.2 and Figure 4.3 respectively. The results in Figure 4.2 and Figure 4.3 indicate that material properties of the chassis are similar to the original chassis, the chassis is mechanically stable and the simulation setup can be used for simulation which incorporates measured noise sources from the original DUT.

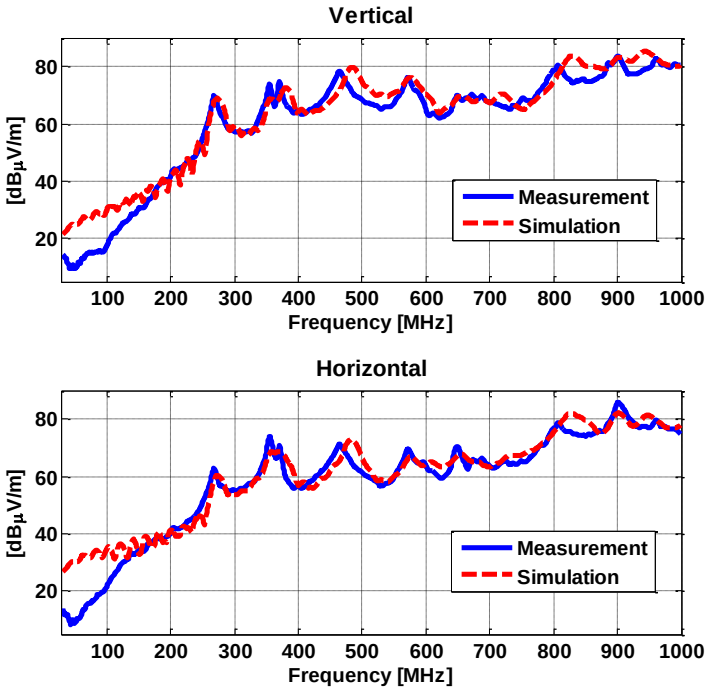

Figure 4.2 Comparison of maximized radiated emissions between measurement and simulation for broadband RF injection into the patch board.

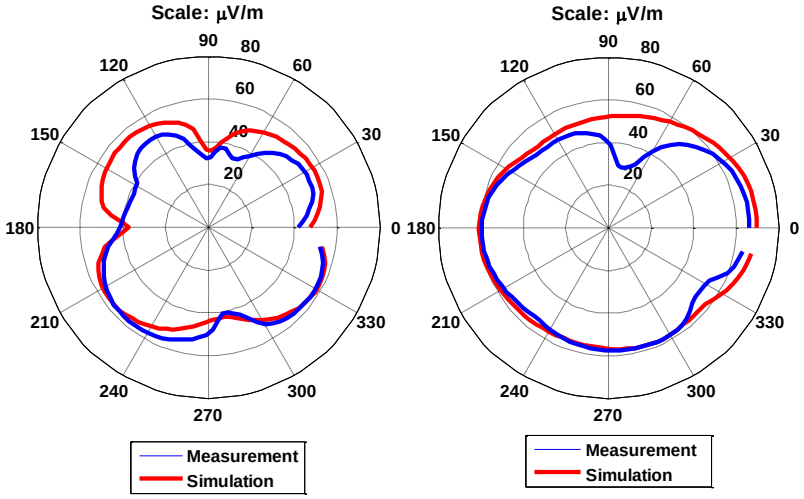

(a) Horizontal polarization (b) Vertical polarization

Figure 4.3 Comparison of the radiation patterns at 540 MHz between the measurement and simulation for the horizontal and vertical polarizations of the receiving antenna.

5. MODELING EMI DUE TO THE FLEX TRACE COMMON MODE NOISE

The LVDS display signals are driven from the main board to the LCD distribution boards via the flex cables. The common mode noise of the LVDS signals through the flex cables and the LCD distribution boards also contributes to the radiated emissions from the TV. To predict the radiated emissions from the TV, common mode LVDS noise source must be included in the TV model along with the main board noise source. The common mode and differential mode LVDS noise injected into the clock trace pair and one of the data trace pairs of the flex trace pairs were measured using a Keysight N2752A active differential probe [6] with a bandwidth of 6 GHz. The flex cables were disconnected from the main board and the LVDS trace pairs were terminated with 100 ohm on the main board. The measurement setup is shown in Figure 5.1. The frequency of interest – the 540 MHz signal corresponds to the 3rd harmonic of the clock signal that has a fundamental frequency of 133 MHz in the LVDS interface which is used for transmitting display signal from the main digital processing board to the LCD distribution board. The measured spectrum around 540 MHz is shown in Figure 5.2. The LVDS clock common mode spectrum is about 20 dB larger than the spectrum due to the next strongest signal component. This result allowed simplifying the modeling of the far field contribution of the flex cable. As the common mode of the clock signal mainly contributes to the far-fields at 540 MHz, only one trace pair of the clock signal is considered in the model described in the section-7. The measured common mode voltage magnitude is used in the model.

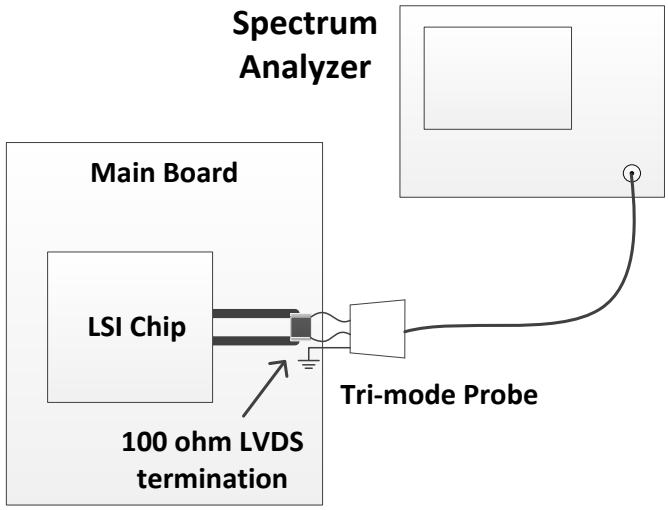

Figure 5.1 Test setup for measuring the common mode and differential mode spectrums of the LVDS clock and data signal on the main board. A special adapter was used for connecting the oscilloscope probe (Keysight N2752A) to the spectrum analyzer.

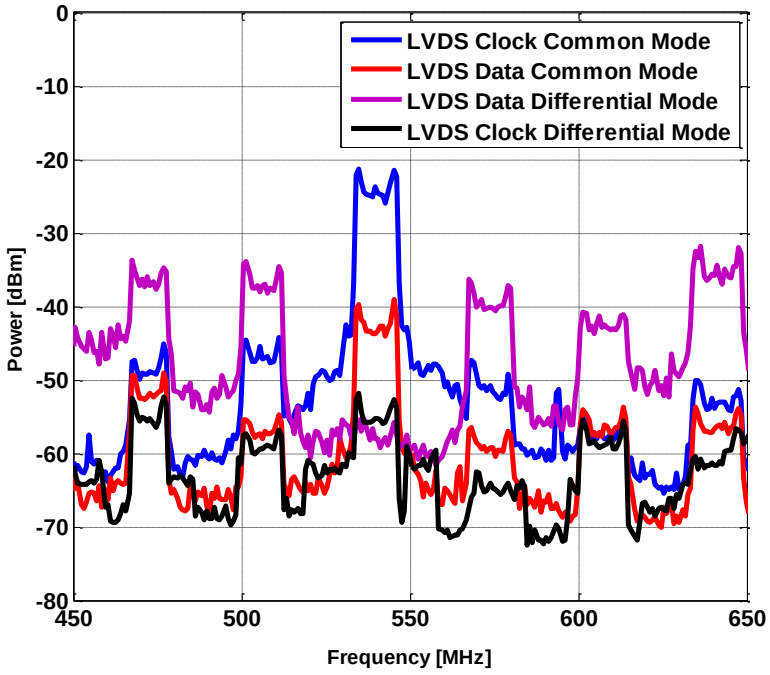

Figure 5.2 Comparison of the measured common mode and differential mode spectrums of the LVDS clock and data signals.

6. MODELING THE MAIN BOARD AS A NOISE SOURCE

The main board of this TV forms the other important source for 540 MHz emissions. The main board consists of a multi-layer printed circuit board with multiple ICs such as the media processors, memory, etc., other circuits such as DC-to-DC converters, external interfaces such as HDMI, USB connectors. In order to model the main board as a noise source using an equivalent Huygens box, the near-fields at 540 MHz around the main board needed to be measured. The inside surface of the back cover is 10 mm above the main board. This requires the top surface of the equivalent field sources of the main board must be placed no more than 10 mm above the main board. To obtain not only magnitude information but also capture the phase of the fields the LVDS clock signal is used as a phase reference for the measured near-fields (Figure 6.1). The LVDS signal uses a spread spectrum; further the data signals and DC/DC converters also contribute to the near field in the 540 MHz spectral band. As a result, the 540 MHz signal is time varying and it has added random like noise that is uncorrelated to the 540MHz signal of interest. To obtain the near-fields corresponding to the 540 MHz LVDS clock signal signals, the LVDS clock signal is used as a reference source for the near-field measurement. A two channel VNA was set to tuned receiver mode in zero-span at the center frequency of 540 MHz. The reference signal, represented as V_A, was connected to port 1, while the scanning signal, represented as V_B, was connected to port 2. The probe factor P was measured using a TEM cell [10]. The number of sample points N was set to 1601. Assuming the scanning probe's signal forms channel B and the reference probe's signal forms channel A, the phase of B can be retrieved from the averaged B/A on the vector network analyzer set to tuned receiver mode. Supposing the reference signal is V_A

and the scanning probe signal is V_B, then the field above the main board, V_S, can be calculated by (1).

$$V_s = P\left[\frac{1}{N}\sum_{i=1}^{N}\frac{v_B^i}{v_A^i}\right]\frac{1}{N}\sum_{i=1}^{N}\left|v_A^i\right| \qquad (1)$$

It can be shown numerically that the arithmetic mean of the measured samples of the ratio V_B/V_A, converges to a number that is proportional to the complex magnitude of the EM-field distribution on the scanning surface under the assumption that the coupling of the reference probe to the unwanted signal is negligible. To achieve this in the measurement of the fields above the main board of the TV, the reference probe was directly connected to the LVDS clock traces. Thus the signal-to-noise ratio of the reference channel was high. To verify this, a number of numerical experiments with different SNRs in the reference channels were conducted.

The work-flow for constructing an equivalent noise source for the main board is described in Figure 6.2. The tangential H-fields were measured using a 5 mm H-field probe at a height of 18 mm above the main board, using API's automatic scanning system [9].

Inductors of DC-to-DC converters had very strong fields at 540 MHz which need to be removed by the averaging process (1). However, since the signal is relatively strong as compared to the LVDS signal, a large number of sample points (>5000) are required which increases the scanning time.

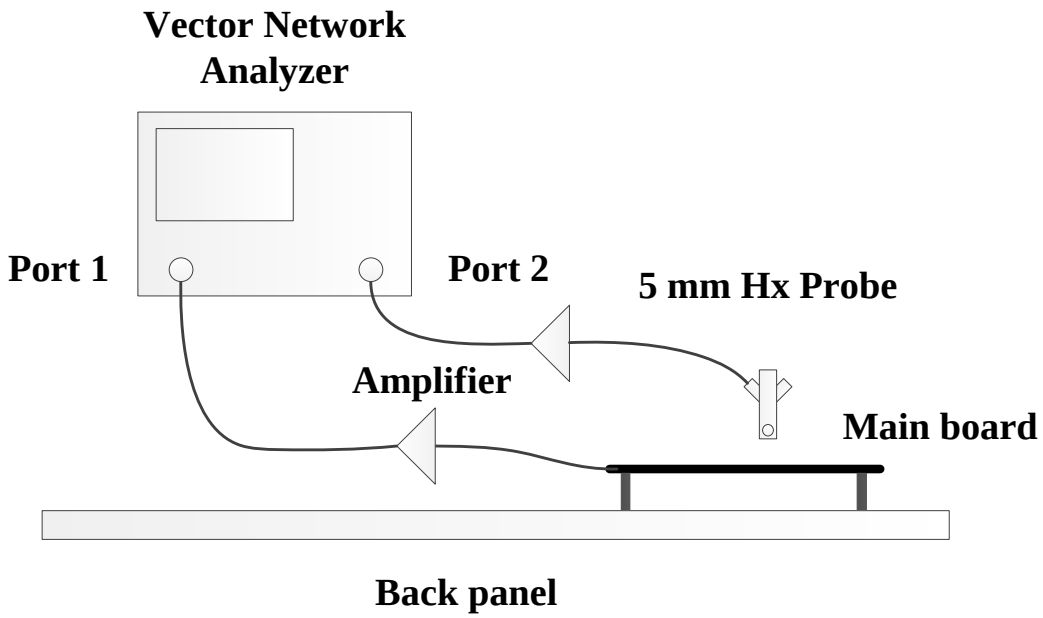

Figure 6.1 Test setup for measuring the tangential H-fields over the main board using the LVDS clock signal as the reference for relative phase measurement.

Scanning the fields at a higher height (18 mm) enabled the use of relatively fewer sample points (1601) for removing the noise by the averaging process. A few random locations were selected over the main board where the noise due to the inductors is lower. At each of these locations, the 540 MHz signal is measured at two heights – 18 mm and 8 mm. The mean of the ratios of the magnitudes at the two heights measured at the different locations is used as a scaling factor that is applied to the magnitude of the near-fields measured at 18 mm to shift the plane to 8 mm above the main board. The total time required for the H-field measurement was about six hours for both components. The steps for calculating the Huygens equivalent surface are summarized in Figure 6.3 [2]. Figure 6.3 (a) represents the original problem for which an equivalent surface is desired.

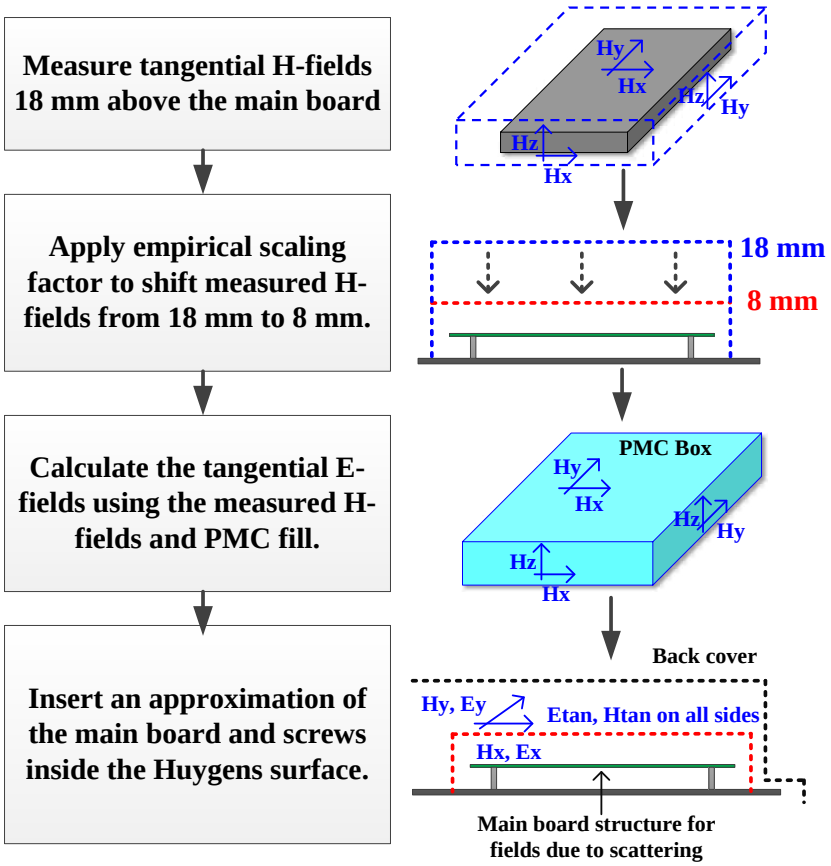

Figure 6.2 Work-flow for modeling the main board as a noise source using an equivalent Huygens box.

The original problem can be simplified to Figure 6.3 (b) using Love's Theorem [8]. From electromagnetic uniqueness concepts, it is known that the tangential components of only E or H are needed to determine the fields. Assuming that the volume is filled with PMC, Figure 6.3 (c) and then impressing Js on its surface S allows the total radiation (E_1, H_1) outside S to be recreated. Thus, only the tangential magnetic field needs to be scanned [12]. To obtain the Huygens equivalent source, the surface enclosed by the measured tangential magnetic fields, shown in Figure 6.4, was filled with PMC to calculate the tangential electric fielsds on the surface (Love's Theorem [8]). According to

the Induction Theorem [11], the fields of an arbitrary source and a structure in close proximity in free space can be considered as the superposition of three parts: 1) the emissions of the source (E_1, H_1) as they would be in the absence of the nearby structure, 2) the scattered field caused by the presence of the nearby structure (E_s, H_s), and 3) the fields re-scattered by the source structure (E_{ss}, H_{ss}), as shown in Figure 6.3 (d). To account for the field scattering between the back cover and the main board, an approximation of the main board and its mounting was used inside the Huygens surface based on the Induction Theorem. The method of including the source structure inside the Huygens box to account for scattering with a nearby obstacle was demonstrated in [13]. The back cover was added to the model and the far-field was calculated in CST microwave [7]. To verify the results of the simulation model, the far-fields and the total radiated power at 540 MHz from the TV were measured. For the measurement, the flex cables, LCD and LCD distribution boards were removed from the DUT and the LVDS pair were terminated on the main board. The comparison between the measured and simulated maximized far-field emissions at 3 m distance from the TV and the total radiated power is shown in Figure 6.5 and Table 6.1 respectively.

The simulated data at 540 MHz is used for the 534 MHz to 546 MHz frequency range to compare with the spread spectrum signal at 540 MHz. Figure 6.5 and Table 6.1 show a maximum difference of 5 dB and 6.8 dB between the measured and simulated radiated emissions which are reasonable considering tolerances of compliance tests.

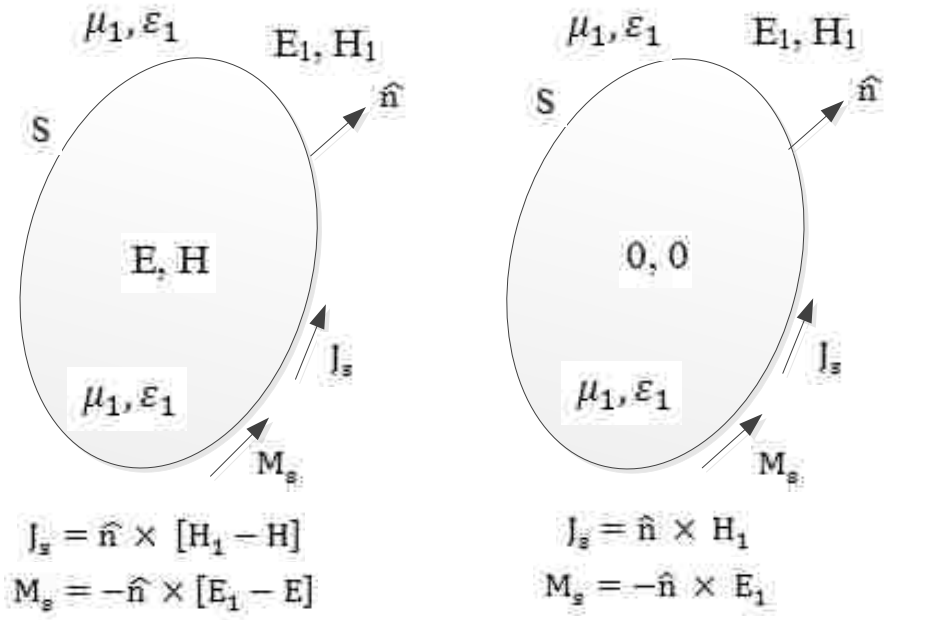

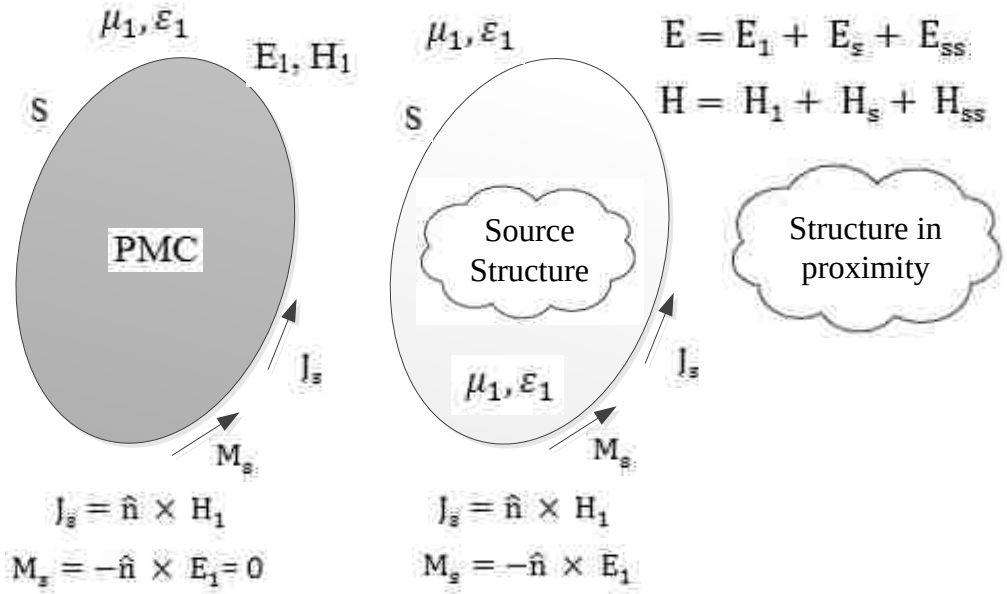

Figure 6.3 Steps for calculating Huygens equivalent of the main board: (a) Original problem, (b) using Love's Equivalent Theorem [8], (c) PMC fill to calculate tangential electric fields for impressed measured magnetic fields, (d) Including the source structure inside the Huygens equivalent surface (Induction Theorem [11]).

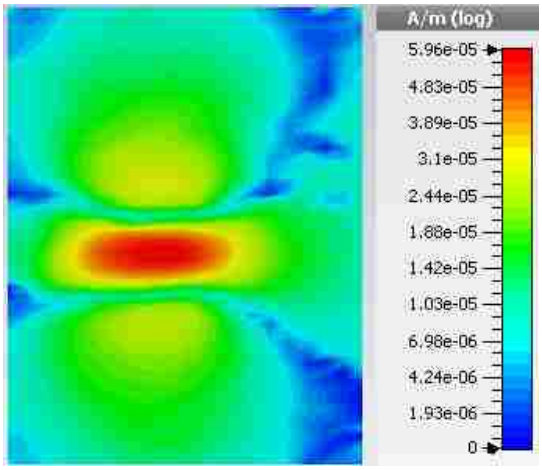

(a) Hy (A/m)

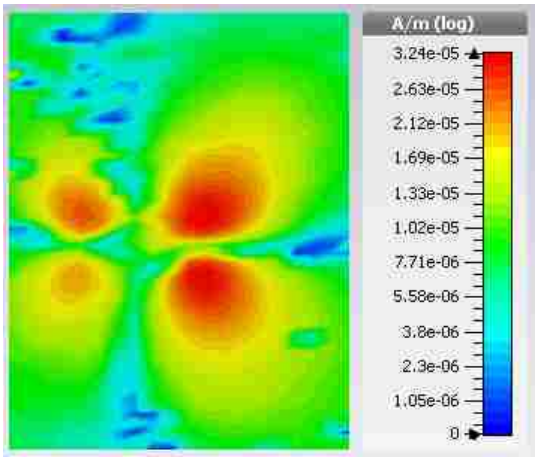

(b) Hx (A/m)

Figure 6.4 Measured tangential H-fields over the main board used as field source in the full wave simulation model.

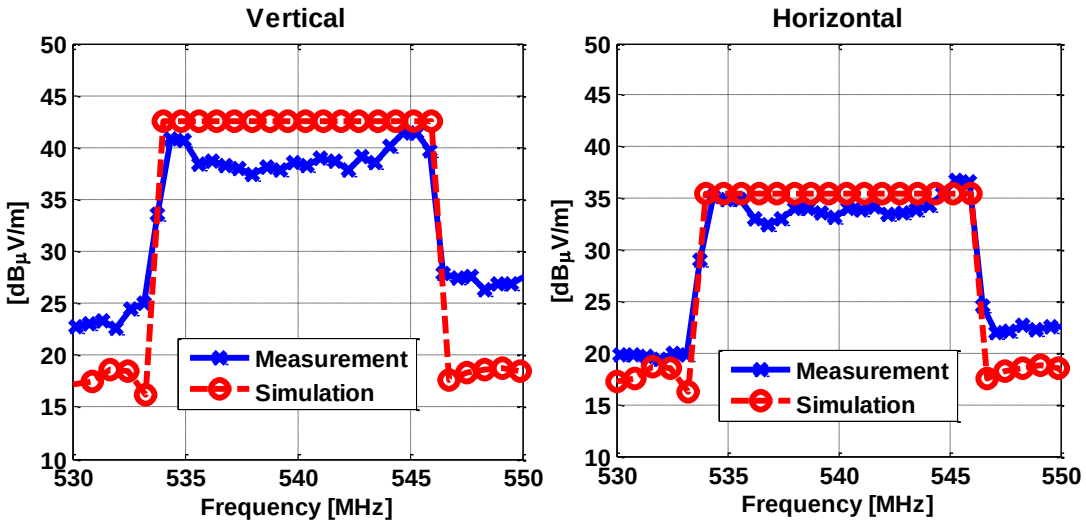

Figure 6.5 Comparison of the maximized radiation around 540 MHz between the measurement and full wave simulation model with the main board as field source.

Table 6.1 Comparison of the total radiated power between the measurement and full wave simulation model for with and without back cover.

Condition	Measurement (dBm)	Simulation (dBm)	Error (dB)
With Back cover	-55	-61.8	6.8
Back Cover Removed	-53	-56.8	3.8

7. INTEGRATED MODEL FOR EMI PREDICTION

The common mode current in the LVDS trace pairs, as shown in Section-V, also contributes to the radiated emissions and needs to be considered in the model for predicting the radiated emissions. The LVDS common mode noise source is included together with the main board field source to obtain the final full wave model, shown in Figure 7.1. The common mode noise source is modeled as a discrete voltage port with a source impedance of 25 ohms that drives a single trace pair in common mode against the main board ground. The common mode noise voltage at 540 MHz obtained from the active differential probe measurement result as shown in Figure 5.1 is used as the discrete port voltage. The phase difference between the common mode noise source and the main board field source is kept at zero, since the field source was measured with a reference probe at the same location as that of the common mode noise source measurement using the active differential probe. The comparison between the measured and simulated far-field radiation at 540 MHz at 3 m distance from the TV is shown in Figure 7.2. The difference between the measured and simulated data is within 10 dB. It must be pointed out that the difference between the simulation and measurement result at 540 MHz is higher for the vertical polarization as compared to the horizontal. A similar difference can be observed in Figure 4.2 for the patch model. The exact reason for this difference is not clear and might be due to reflections in the measurement chamber. The comparison between the measured and simulated total radiated power is listed in Table 7.1.

Table 7.2 lists the approximations used for modeling the noise sources and their relative impact on the accuracy of the simulated results in the TV under investigation. The final simulation model running on a machine with four GPUs, reached the

convergence criteria in seven hours. Modeling the entire frequency band can become numerically expensive.

Table 7.1 Comparison of the measured and simulated radiated emissions around 540 MHz for the main board and LVDS common mode voltage excitation.

Measurement (dBm)	Simulation (dBm)	Error (dB)
-55.7	-61.6	5.9

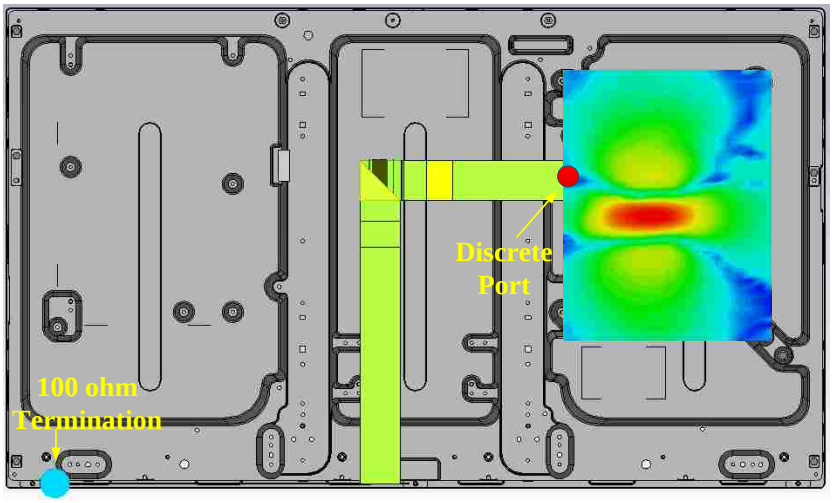

Figure 7.1 Test setup for simultaneous excitation of the discrete port common mode voltage source and the main board Huygens box field source for calculating the radiated emissions.

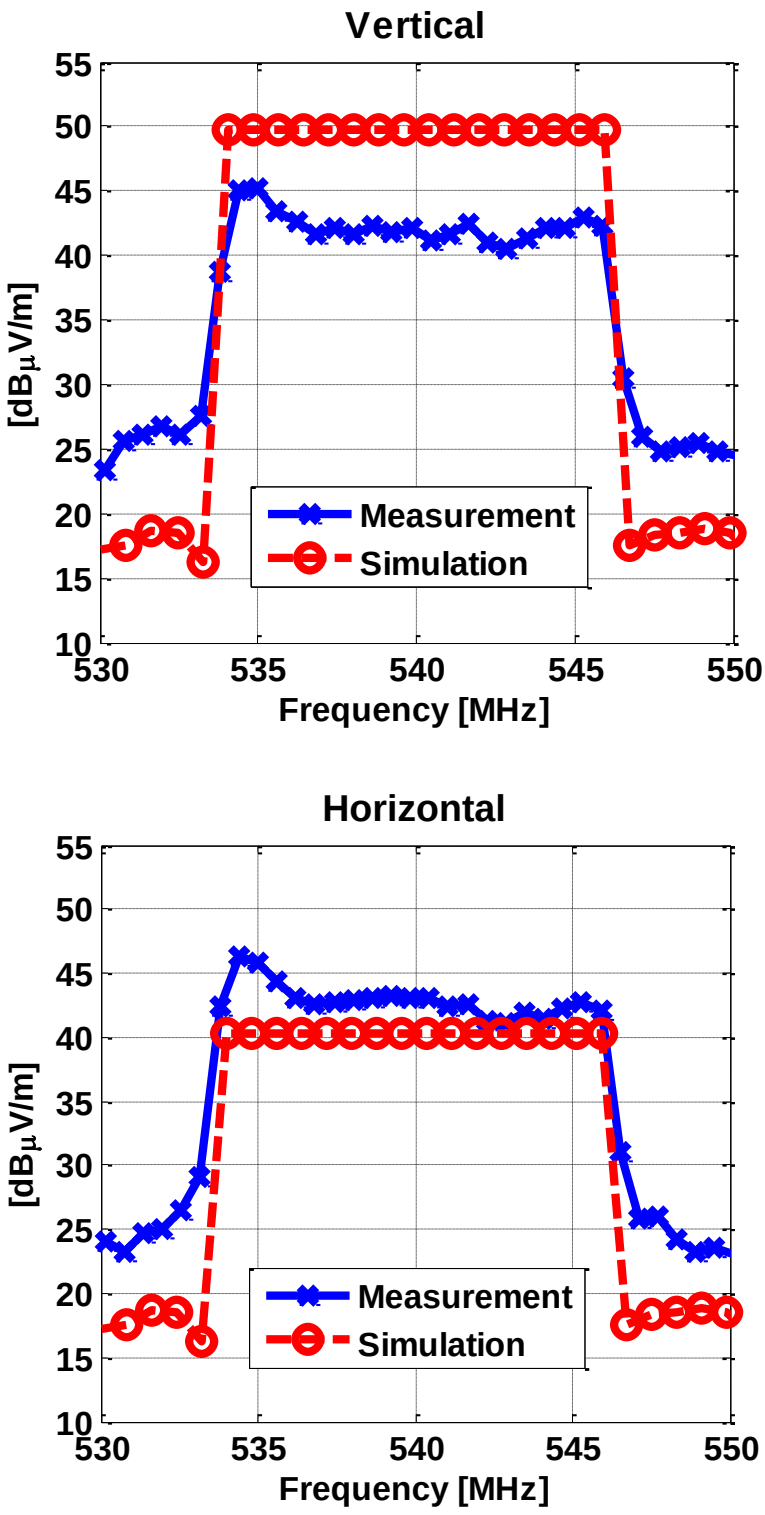

Figure 7.2 Comparison of the measured and simulated radiated emissions around 540 MHz for the combined model.

Table 7.2 Summary of the modeling difficulties and approximations used in the integrated model.

Modeled Physical Quantity	Actual condition		Modeling Difficulty	Approximation Used	Impact on Accuracy and Reasoning
Main Board: Huygens Equivalent source	1.	Physical structure is a complex layout of traces, ground planes, ICs, discrete components	Requires: • Significantly large mesh density. • Long simulation time.	Modeled as metal plate with a FR-4 dielectric layer.	Low. The impact of the accuracy of the source geometry on accuracy of the calculated scattered field is low.
	2.	540 MHz noise sources: Multiple sources contribute to the 540 MHz signal – LVDS clock, LVDS data, broadband noise from DC-to-DC converter, etc.	Repeated near-field measurements taking all the potential noise sources as reference are extremely time consuming, numerically expensive and results are difficult to combine into one field source.	The 540 MHz signal corresponding to the most dominant source – LVDS clock signal is measured.	Low. Measurement confirmed the LVDS clock signal as the strongest source for the 540 MHz signal over the area of the main board.
	3.	Requirement to measure the near-field at less than the back cover height (10 mm) above the main board.	Cancellation of strong broadband noise from uncorrelated sources such as DC-to-DC converters - requires extremely large number of sample points > 5000 pts.	Near-field at 8 mm above the main board calculated by measuring the near-fields at 18 mm and correcting using a scaling factor.	Moderate. The scaling factor is obtained by measurements by taking the average of the ratio of scanned fields at two different heights at multiple locations on the main board.

Table 7.2 Summary of the modeling difficulties and approximations used in the integrated model (cont.)

Modeled Physical Quantity	Actual condition		Modeling Difficulty	Approximation Used	Impact on Accuracy and Reasoning
Noise through Flex cables	1.	Differential and Common mode noise at 540 MHz signal due to 1-LVDS clock pair and 3-LVDS data pairs.	Measurement of currents and voltages for all modes within the 4x2 wire system would require complex probing.	Common mode noise at 540 MHz due to LVDS clock pair injected into 1-trace pair.	Low. Results from section-V indicate that the common mode LVDS-clock noise is 20 dB higher than the next strongest.

8. CONCLUSION

A variety of methods partially novel were combined to create a simulation model of a TV to predict the most critical radiated emissions caused due to the display signals. For identifying which aspects of the TV need to be modeled, radiated emissions measurements, total radiated power measurements, substitution boards and voltage and current measurements are used. Next a simulation model is created to verify sufficient accuracy of the modeling of the passive structure of the TV and to determine the effective conductivity and dielectric constant of metal and plastic parts respectively. The next step is to determine the sources. Two sources contributed to the far field, one being the common mode current on the complex flex cable due to the LVDS clock, the other is the excitation of the TV structure by the fields from the main board. To model the contribution of the flex cable the common mode current was measured using an active differential probe. The main board was modeled as an equivalent Huygens source based on phase resolved near-fields measured around it using an H-field probe. For including the near fields of the main board a multi-step process was used resulting into a Huygens box that includes an approximation of the main board structure following Love's and Induction principle. The combined model allowed to predict the most critical emissions at 540 MHz for radiated fields and total radiated power caused due to the display signals

REFERENCES

[1] S. A. Schelkunoff, "Some equivalence theorems of electromagnetics and their application to radiation problems," Bell System Technical J. vol. 15, no. 1, pp. 92-112, 1936.

[2] C. A. Balanis, Advanced Engineering Electromagnetics, Hoboken, NJ, USA: Wiley, 1989, pp. 323–325.

[3] P. Peter, and T. K. Sarkar, "Planar near-field to far-field transformation using an equivalent magnetic current approach," IEEE Trans. Antennas Propag., vol. 40, no.11, pp. 1348-1355, Nov. 1992.

[4] H. Weng, D. G. Beetner, and R. E. DuBroff, "Prediction of radiated emissions using near-field measurements," IEEE Trans. Electromagn. Compat., vol. 53, no. 4, pp. 891-899, Nov. 2011.

[5] J. Shi, M. Cracraft, J. Zhang, R. E. DuBroff, and K. Slattery, "Using near-field scanning to predict radiated fields," in Proc. IEEE Int. Symp. Electromagn. Compat., Santa Clara, CA, 2004, pp. 14-18.

[6] Keysight N2752A active differential probe datasheet: http://literature.cdn.keysight.com/litweb/pdf/5991-0560EN.pdf

[7] CST Microwave Studio. [Online]. Available: http://www.cst.com

[8] A. E. H. Love, "The integration of the equations of propagation of electric waves," Phil Trans. Roy. Soc. London, Ser. A, vol. 197, pp. 1- 45, 1901.

[9] Smart Scan EMI 350. [Online]. Available: http://www.amberpi.com

[10] Myron L. Crawford, "Generation of standard EM fields using TEM transmission cells", IEEE Trans. Electromagn. Compat., vol EMC-16, No. 4, 1974.

[11] C. A. Balanis, Advanced Engineering Electromagnetics, Hoboken, NJ, USA: Wiley, 1989, pp. 323–325.

[12] X. Gao, J. Fan, Y. Zhang, H. Kajbaf, and D. Pommerenke, "Far-field prediction using only magnetic near-field scanning for EMI test," IEEE Trans. Electromagn. Compat, vol.PP, no.99, pp.1-9, May 2014.

[13] O. Franek, M. Sorensen, H. Ebert, and G. F. Pedersen, "Influence of nearby obstacles on the feasibility of a Huygens box as a field source," in IEEE Int. Symp. Electromagn. Compat, pp. 600-604, 2012.

II. A FREQUENCY TUNABLE HIGH SENSITIVITY H-FIELD PROBE USING VARACTOR DIODES AND PARASITIC INDUCTANCE

Satyajeet Shinde, *Student Member, IEEE*, Shubhankar Marathe, Guanghua Li, Reza Zoughi, *Fellow, IEEE,* David Pommerenke, *Fellow, IEEE*

ABSTRACT

A frequency tunable resonant magnetic field probe is designed for near-field scanning applications for radio frequency interference (RFI) studies. Tunable resonance is achieved by using a varactor diode providing the required capacitance and the parasitic inductance of a magnetic loop (i.e., a parallel LC circuit). An equivalent circuit model for the probe is described, analyzed, and used for designing the probe for achieving maximum sensitivity. The resonance frequency of the designed probe is tunable in the frequency range of 900-2260 MHz that covers multiple radio bands, such as the GSM900, UMTS, and GPS bands. The sensitivity of the probe at the resonance frequency is about 7-9 dB higher than that of an equivalently-sized broadband magnetic field probe throughout the tunable frequency range. The measured frequency response and sensitivity over a microstrip trace using the fabricated probe shows good agreement with the simulated results of the equivalent circuit model and the full wave simulation model.

Index Terms— Frequency tunable, GSM band, GPS band, radio frequency interference, resonant magnetic field probe, receiver desensitization, varactor diode.

1. INTRODUCTION

Recent trends in modern mobile computing and communication devices show integration of an increasing number of radio frequency bands and antennas for implementing wireless interfaces for communication and high-speed data-transfer capabilities. For example, a typical modern mobile phone contains various RF sub-systems such as GSM, GPS, Wifi, NFC, and Bluetooth. High-speed digital circuits can generate high-frequency noise due to their switching nature. When the noise contains spectral components in the wireless bands, it becomes a potential noise source for radio-frequency interference (RFI). On-chip DC-DC converters, high-speed memory clocks, I/O busses, and LCD clock harmonics are a few typical examples of such noise sources. Other trends show an increasing volume density in electronic products which is calculated as the ratio of the volume of space taken up by electronic parts to the total available volume inside the electronic product. The combined effect of all these trends results in the placement of potential noise sources and victim circuits in close proximity to each other. This has the potential to cause severe RFI issues such as receiver desensitization, noise coupling, antenna detuning, etc. Various types of techniques for investigating RFI in mobile devices have been studied in [1]-[3]. Near-field scanning probes provide an effective approach to measure and quantify electromagnetic fields in the vicinity of the probes. RFI issues such as receiver desensitization require the measurement of electromagnetic noise well below -100 dBm to identify potential noise sources (i.e., low trace currents lead to very low magnetic field strengths).

Researchers have investigated ways to improve the bandwidth, spatial resolution, and suppression of unwanted field-components of near-field probes [4]-[5]. Methods for

enhancing the probe sensitivity by modifying the near-field characteristics close to the device such as the use of single negative metamaterials and single split ring resonators have been demonstrated in [6]-[7]. Resonant probes are an attractive option for investigating receiver desensitization issues since the receivers usually operate in narrow frequency bands and enhancing the probe sensitivity at the particular frequency band of interest is sufficient for this purpose. Resonant probe design techniques for electric and magnetic fields have been demonstrated in [8]-[10]. However, these probes exhibit enhanced sensitivity only at a fixed frequency and by design are limited in their use at a fixed RF frequency. For identification of noise sources at multiple frequency bands within the same device under test, multiple probes each designed for a fixed resonant frequency would then be required. This requires additional design and manufacturing efforts and necessitates stringent manufacturing tolerances to ensure that the target resonant frequency is achieved.

This problem is alleviated with a frequency tunable probe since the resonant frequency of a frequency tunable probe can be tuned to practically any frequency within the designed tunable frequency range of the probe. Furthermore, automated scanning systems are widely used for near-field scanning over a device under test by attaching a probe to the scanning arm of a robot. Scanning for multiple RF bands on a device would require multiple scans one for each fixed resonant probe. An electronically-tunable resonant frequency probe facilitates measurement of fields at multiple frequencies, in a single scan setup, by conducting measurements at multiple frequencies at each scan point resulting in shorter scanning times and higher level of automation by eliminating the requirement for changing probes.

The tunable probe described in this paper is designed by creating a parallel LC resonance that is implemented incorporating a tuned varactor diode with the parasitic inductance of the probe's (magnetic) loop. An equivalent circuit model for the probe is described, analyzed, and used for designing the probe for achieving maximum sensitivity in the target operating frequency range of 900-2260 MHz. The sensitivity of the probe at the resonance frequency is shown to be about 7-9 dB higher than that of an equivalently-sized broadband magnetic field probe, throughout the tunable frequency range. The measured frequency response and sensitivity over a microstrip trace using the fabricated probe shows good agreement with the simulated results of the equivalent circuit model and the full wave simulation model.

2. EQUIVALENT CIRCUIT AND FULL-WAVE SIMULATION MODEL

When using a varactor diode to represent a capacitance in a resonant circuit, the resonance frequency can easily be changed by reverse biasing (using a DC voltage) the varactor. Then, by incorporating a magnetic loop in the probe, which produces the necessary shunt parasitic inductance, the resonant frequency of the probe can be changed. In practice the parasitic inductance (ESL), the equivalent series resistance (ESR) of the varactor diode, DC blocking capacitors, and other parasitics also affect the resonant frequency. The schematic in Figure 2.1 illustrates the idea of using a varactor diode with a magnetic loop for this purpose.

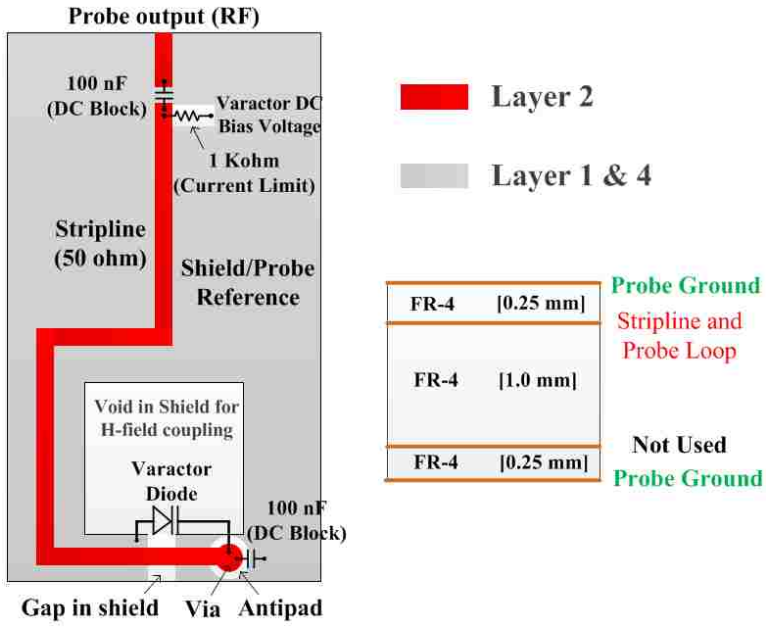

Figure 2.1 Illustration of the proposed probe: a varactor diode and magnetic loop for achieving tunable resonance along with the PCB stack up information.

Considering the relevant circuit parasitics, the equivalent circuit of the proposed probe, created using Agilent ADS® [11], is presented in Figure 2.2. The equivalent circuit is used to obtain the voltage developed at the probe output due to the magnetic field coupling to the probe placed 2 mm above a 50 ohm microstrip line (commonly the objective of such RFI measurements). The coupling between the microstrip trace and the probe loop is represented by two coupled inductors. The probe parasitic parameters such as L and C are calculated from the simulated input impedance obtained by placing an excitation port in between the gap in the probe shield at the probe tip using the full wave model of the probe.

In the fabricated probe, two varactor diodes are used with two parallel DC blocking capacitors for each diode to block the reverse bias voltage applied to the varactor diodes. The ESL, ESR, and the capacitance of the varactor diode are obtained from the specifications of the Skyworks SMV1234-04LF varactor diode used in this investigation [12]. The variation of the capacitance as a function of the reverse bias voltage for the SMV1234-04LF is shown in Figure 2.3. A stripline with an impedance of 50 ohms is used to connect the magnetic loop output to the probe output. Another impedance matching transmission line is connected from the stripline to the probe ground through a DC blocking capacitor. The radiation resistance for the probe was modelled using the expression for radiation resistance of a rectangular loop [13]. The length of the impedance matching transmission line is optimized to obtain maximum power transfer from the magnetic loop to the probe output. To optimize the design of the probe for maximum sensitivity, a full wave simulation model is constructed in Ansys HFSS® [14].

The probe loop structure and the orientation of the probe above the microstrip trace are shown in Figure 2.4.

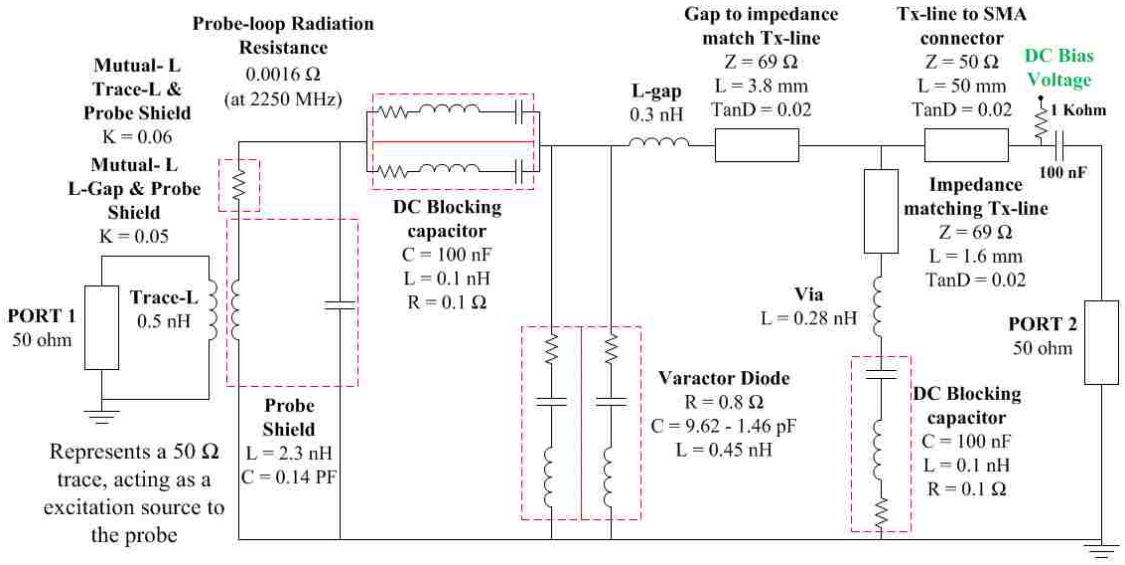

Figure 2.2 Equivalent circuit diagram of the magnetic field coupling from the microstrip trace to the tunable resonance probe.

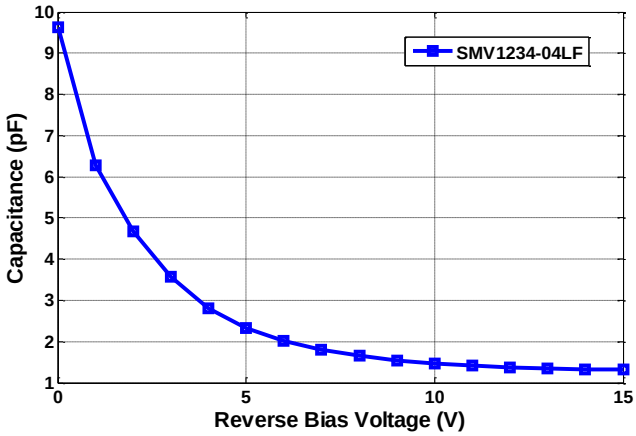

Figure 2.3 Variation of capacitance of the varactor diode (SMV1234-04LF) as a function of applied reverse biased voltage [12].

To emulate the varactor diode, a lumped capacitor is placed in the gap of the probe shield on each side of the loop. The value of the capacitor was parametrically varied to achieve resonances at various frequencies within the desired frequency range of interest. For simplicity, the DC blocking capacitors were not considered in the full-wave simulations since their influence on the RF performance of the probe is negligible. The complete full-wave simulation model consists of the probe model positioned at a height of 2 mm over a microstrip trace such that the magnetic field coupling is dominant. The dimensions of various elements of the probe loop, as shown in Figure 2.4 are optimized to obtain maximum sensitivity of the probe over the desired tunable frequency range.

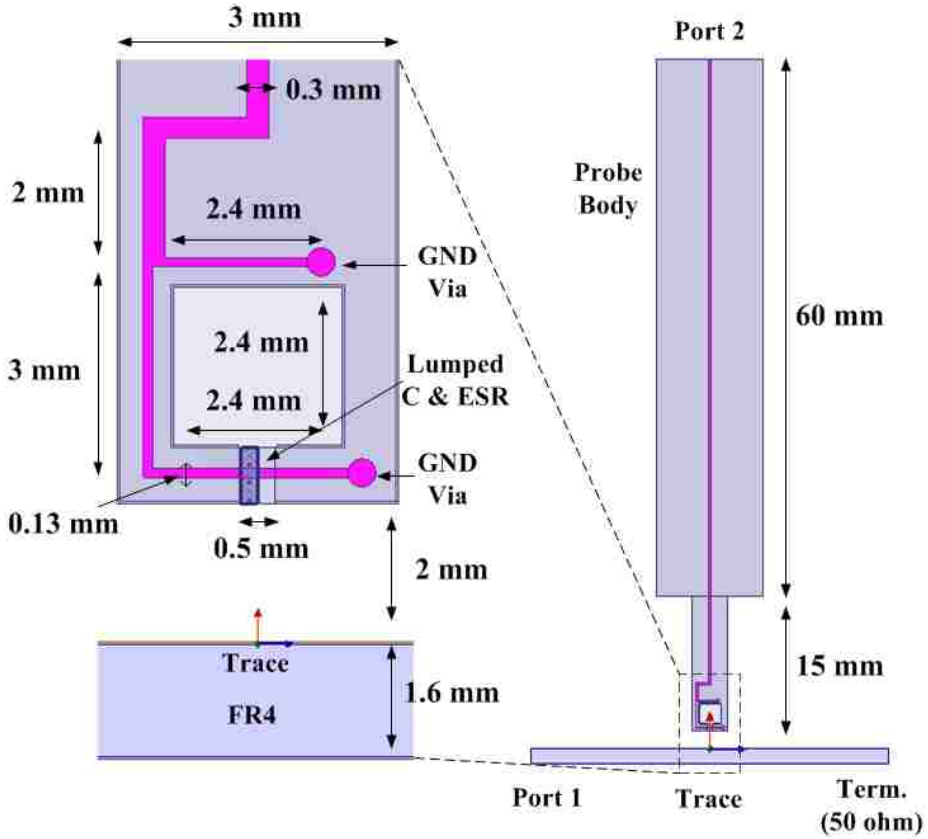

Figure 2.4 Full wave simulation model with probe loop dimensions for obtaining the magnetic field coupling to the probe at a height of 2 mm above the microstrip trace.

3. FABRICATED PROBES AND FREQUENCY RESPONSE

The probe was fabricated using 3 layers of a 4-layer printed circuit board (PCB) using an FR-4 dielectric, as shown in Figure 3.1 (a). The top and bottom copper layers are used as the probe ground. The 2nd layer is used for the stripline and the probe loop. The 3rd copper layer is not used. As a reference and for comparison, a broadband magnetic field probe with an equivalent loop size was also designed and fabricated. The broadband probe and the various parts of the fabricated tunable frequency probe are shown in Figure 3.1. The capacitance of the varactor diode used can be varied in the range 1.32 pF-9.62 pF by varying the reverse bias from 15 V-0 V. To characterize the frequency response and sensitivity of the fabricated probes the measurement setup described in Figure 3.2 was used. Port 1 of the vector network analyzer (VNA) is used as the excitation source for the 50 ohm microstrip trace which is terminated with 50 ohms. The probe output is connected to the Port 2 of the VNA using coaxial cables. The probe is positioned at the height of 2 mm above the microstrip trace. The probe's magnetic loop is oriented in the Y-Z plane such that the H_x component of the magnetic field from the microstrip trace is the dominant measured field.

The comparison between the ADS® circuit model and the measured S_{21} (dB) magnitude for varactor capacitance values of 1.46 pF, 3.1 pF and 9.6 pF corresponding to reverse bias voltages of 15 V, 4.3 V and 0 V along with the broadband probe response is shown in Figure 3.3.

It can be observed that the gain of the resonant probe (for the simulations and measurements) is about 7-9 dB higher than that of the broadband probe at each of the resonant frequencies.

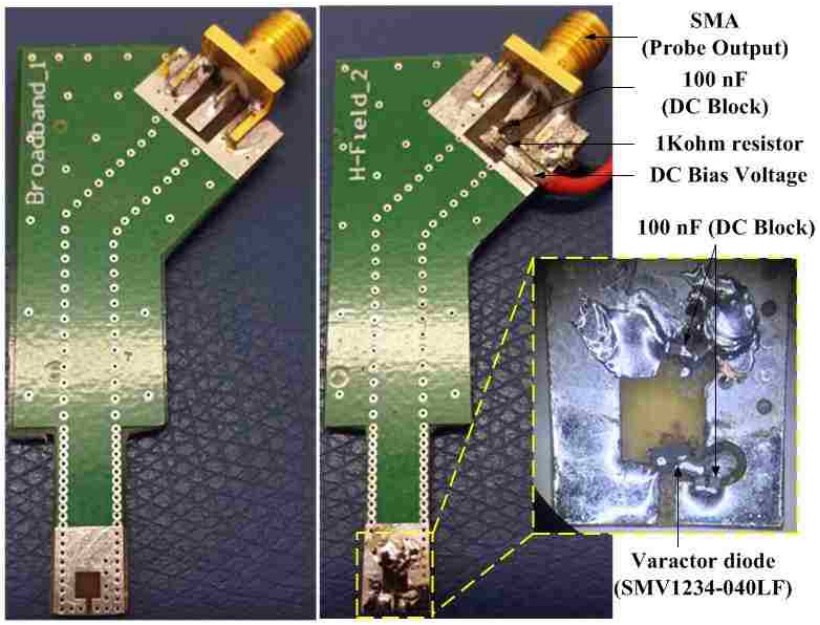

(a) (b)

Figure 3.1 a) Fabricated broadband magnetic-field probe, and b) fabricated tunable resonance magnetic field probe.

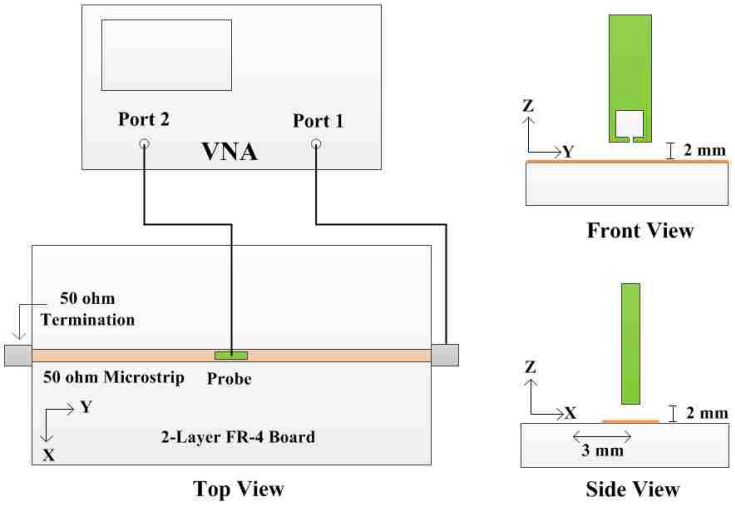

Figure 3.2 Measurement setup showing probe orientation for measuring the field 2 mm above the microstrip trace.

The rejection of unwanted E-field coupling, measured for the probe orientation in the X-Z plane, is about 15 dB at the resonant frequencies. The comparison between the measured and simulated S_{11} (dB) magnitude for the capacitance values is shown in Figure 3.4. The comparison of the S_{21} (dB) magnitude between the measurement and full-wave (Ansys HFSS®) simulation result is shown in Figure 3.5. These results show that the frequency response and sensitivity estimated using the equivalent circuit model and the full wave simulation model shows good agreement with the measured results for the fabricated probe. The probe factor of the H-field probe was measured using a TEM cell to be 7.2 dB A/m/V and 4.4 dB A/m/V at 890 MHz and 1710 MHz, respectively.

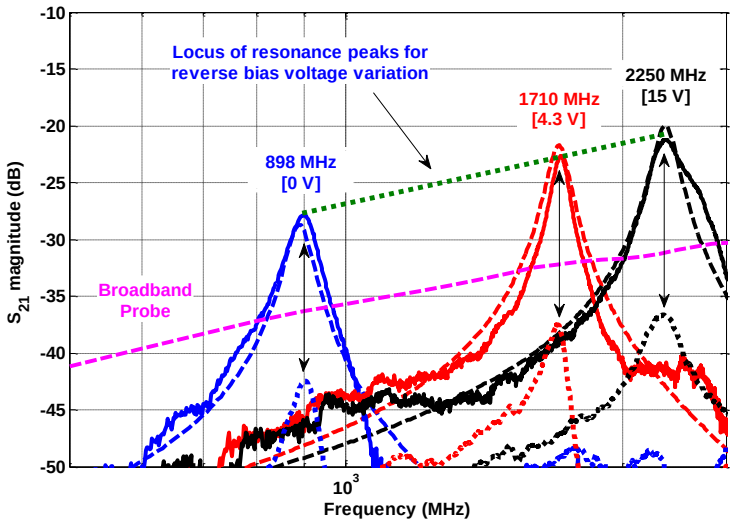

Figure 3.3 Comparison between the measured and circuit model (ADS®) S_{21} (dB) for the tunable resonant frequency probe for 0 V, 4.3 V and 15 V applied reverse bias voltage. dashed line: simulation, solid line: measurement, dotted line: measurement for probe orientation in X-Y plane (unwanted E-field coupling).

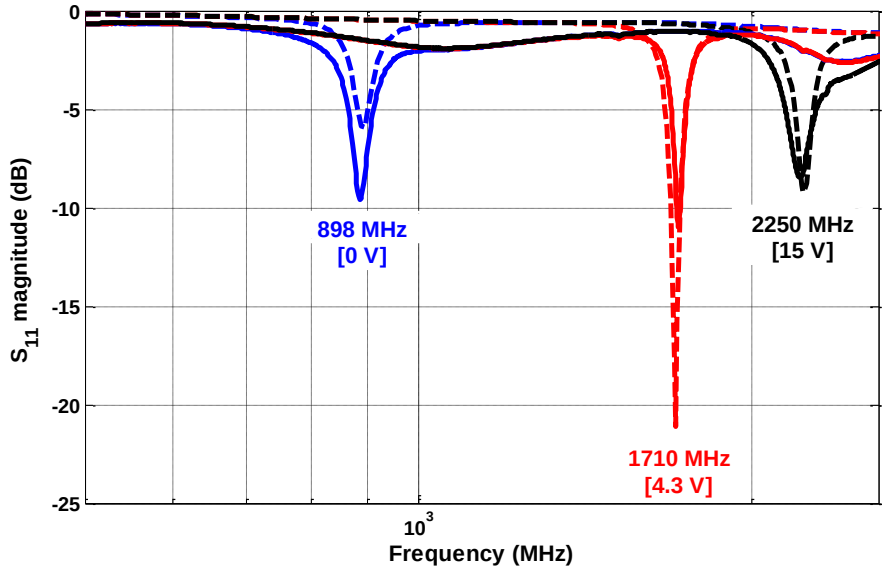

Figure 3.4 Comparison between the measured and circuit model (ADS®) S_{11} (dB) for the tunable resonant frequency probe for 0V, 4.3 V and 15 V applied reverse bias voltage. dashed line: simulation, solid line: measurement.

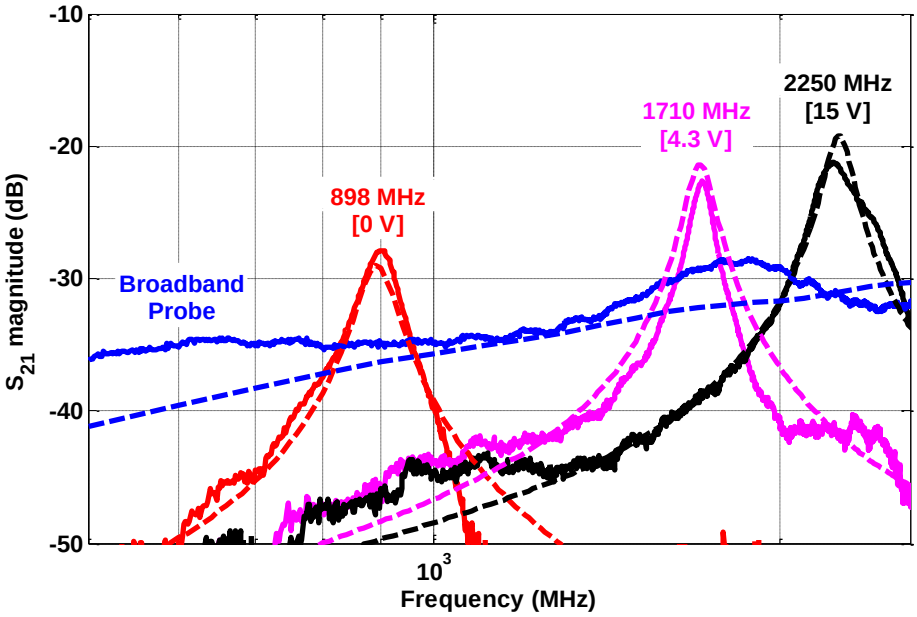

Figure 3.5 Comparison between the measured and full-wave (HFSS®) simulation S_{21} (dB) for the broadband and tunable resonant frequency probe for 0V, 4.3 V and 15 V applied reverse bias voltage. dashed line: simulation, solid line: measurement.

4. CONCLUSION

A frequency tunable probe having an improved sensitivity, relative to an equal size loop probe based on parallel LC resonance, is designed by using a tuned varactor diode and the parasitic inductance of a loop probe. The capacitance across the varactor diode can be varied using the applied reverse bias voltage to control the resonance frequency of the magnetic field probe. The resonance frequency of the designed probe is electronically tunable in the frequency range of 900-2260 MHz that covers multiple radio bands, such as the commonly used GSM900, UMTS, and GPS bands. An equivalent circuit model for the probe is described, analyzed, and used for designing the probe for achieving maximum sensitivity in the target frequency range. The sensitivity of the probe at the resonance frequency is about 7-9 dB higher than that of an equivalently sized broadband magnetic field probe throughout the tunable frequency range. The measured frequency response and sensitivity of the fabricated probe over a microstrip trace show good agreement with the simulated results of the equivalent circuit model and the full wave simulation model.

REFERENCES

[1] K. Slattery and H. Skinner, “Platform Interference in Wireless Systems: Models, Measurement, and Mitigation”. Newnes, 2008.

[2] S. Shinde, A. Radchenko, J. Pan, S.-H. Kang, D. Kim, S. Lee, J. Fan, D. Pommerenke, “Investigation of Interference in a Mobile Phone from a DC-to-DC Converter”, Proceedings of IEEE EMC Symposium 2013, Denver, CO, August 5-9, 2013.

[3] S. Shinde, Liang Li, Koichi Ito, Yoshihiro Kato, Noriyuki Mukai, Kenji Araki, Jun Fan, “Investigating Intra-System Radio-Frequency Interference from High-Speed Traces to a GPS Patch Antenna”, Proceedings of IEEE EMC Symposium 2013, Denver, CO, August 5-9, 2013.

[4] Y. Gao and I. Wolff, “A new miniature magnetic field probe for measuring three-dimensional fields in planar high-frequency circuits,” IEEE Trans.Microw. Theory Tech., vol. 44, no. 6, pp. 911–918, Jun. 1996.

[5] J.-M Kim, W.-T. kim, and J.0G. Yook, “Resonance suppressed magnetic field probe for EM field-mapping system.” IEEE Trans. Microw. Theory Tech., vol. 53, no.9, pp. 2693-2699, Sep. 2005.

[6] M. S. Boybay and O. M. Ramahi, “Experimental and numerical study of sensitivity improvement in near-field probes using single-negative media,” IEEE Trans. Microw. Theory Tech., vol. 57, no. 12, pp. 3427–3433, Dec.2009.

[7] Z. Ren, M. S. Boybay, and O. M. Ramahi, “Near-field probes for subsurface detection using split-ring resonator,” IEEE Trans. Microw. Theory Tech, vol. 59, no. 2, pp. 488–495, Feb. 2011.

[8] Eakhwan Song, Hyun Ho Park, “A High-Sensitivity Electric Probe Based on Board-Level Edge Plating and LC Resonance”, Microwave and Wireless Components Letters, IEEE, Oct. 2014, pp. 908-910.

[9] G. Li, K. Itou, Y. Katou, N. Mukai, D. Pommerenke, and J. Fan, “A resonant E-field probe for RFI measurements,” IEEE Trans. EMC, vol. 56, no. 6, pp. 1719-1722, 2014.

[10] H.-H. Chuang, G.-H. Li, E. Song, H.-H. Park, H.-T. Jang, H.-B. Park, Y.-J. Zhang, D. Pommerenke, T.-L.Wu, and J. Fan, “A magnetic-field resonant probe with enhanced sensitivity for RF interference applications,” IEEE Trans. Electromagn. Compat., vol. 55, no. 6, pp. 991–998, Dec. 2013.

[11] ADS® ver. 2014.01, Keysight Technologies, Available: http://www.keysight.com/main/home.jspx?cc=US&lc=eng.

[12] http://www.skyworksinc.com/uploads/documents/200058Q.pdf.

[13] C. A. Balanis Antenna Theory: Analysis and Design, 1982 :Wiley.

[14] HFSS®, ver. 13, Ansoft Corp., Pittsburgh, PA, USA, 2011. [Online]. Available: http://www.ansoft.com/.

III. WIDEBAND MICROWAVE REFLECTOMETRY FOR RAPID DETECTION OF DISSIMILAR & AGED ICS

Satyajeet Shinde, *Student Member, IEEE,* Sasi Jothibasu, Mohammad T. Ghasr, *Senior member, IEEE* and Reza Zoughi, *Fellow, IEEE*

ABSTRACT

A wideband microwave method is described as a means for rapid detection of slight dissimilarities and aging effects in integrated circuits (ICs). The method is based on measuring the complex reflection coefficient of an IC when illuminated with an open-ended rectangular waveguide probe, at K-band (18-26.5 GHz) and Ka-band (26.5-40 GHz) microwave frequencies. The spatially-integrated reflected electromagnetic (EM) signature of a given IC is a function of its internal material properties, geometry and metallic deposition of circuit element and wire bonds. Consequently, dissimilar (including counterfeit) and aged ICs exhibit markedly different reflection properties than their reference and new (non-aged) counterparts. In addition to measuring *spatially-integrated* complex reflection coefficient (over the waveguide aperture), it is also integrated over the operating frequency band (*spectrally-integrated*), resulting in significant increase in the robustness of the approach. Root-mean-squared-error (RSME), defined as the average Euclidean distance between two reflection coefficient vectors, is used to associate a *quantitative metric* to the complex reflection coefficient difference between two dissimilar ICs. Measurement results on several sets of ICs having the same package (DIP-14) and different functionalities, similar functionalities with slight differences in specifications and aged ICs are presented. The results clearly indicate the

capability of this method to differentiate among ICs having slight differences in packaging material properties and/or electronic circuitry.

Index Terms— aged IC, counterfeits IC, microwave reflectometry, open-ended waveguide, reflection coefficient, nondestructive testing.

1. INTRODUCTION

Reliable detection of minutely dissimilar (in design and properties), counterfeits and old/aged Integrated Circuits (ICs) is an important practical issue as it relates to proper functionality and security risks. Some of the direct risks include system or product failure leading to loss of resources and human lives, financial losses incurred by the original IC manufacturer, reduced mean-time-before-failures (MTBF), and compromised confidential information and data. The indirect risks include negative impact on a company's reputation, valuation and market competitiveness and profitability [1]-[3]. Counterfeit ICs account for about 1% of semiconductor unit sales, totaling about 3 billion US dollars worldwide [4]. Typically counterfeit ICs fall under the following classification and can be detected based on comparing their specific parameters or features with samples from the original manufacturer [5]:

- recycled and remarked ICs,
- cloned as the original IC through reverse engineering with fake documentation and certifications,
- excess or defective ICs sold illegally outside the industry by remarking the package with different grade specifications,
- tampered with ICs that exhibit different functionality under some conditions,
- different die sizes, missing bond wires, different interconnect layout, missing protection circuits,
- degraded performance due to improper design, and

- old or aged ICs that have plastic packaging deterioration or degradation due to environmental effects.

Developing techniques for rapid and reliable detection of slight dissimilarities in IC characteristics (e.g., a counterfeit) and variations in its packaging caused by aging is increasingly desirous by manufacturing, commercial and governmental entities. Several counterfeit IC detection methods currently exist that for example involve: physical and electrical inspection methods, visual inspection methods (using typically less than 10X magnification) to check the authenticity of IC package markings by comparing them to the genuine ICs [5]-[7]. However, physical inspection methods can be extremely time-consuming, unreliable, and impractical for testing large number of ICs and can lead to their destruction. X-ray imaging, optical inspection and Scanning Electron Microscope (SEM) are used to study the internal structure of an IC such as the internal die, bond wires and bond types. Techniques such as X-ray fluorescence and ion chromatography can be used to determine the chemical composition of IC plastic package [8]. Although X-ray imaging methods offer higher resolution than visual inspection and are nondestructive, they require expensive equipment, trained operators, significant safety precautions and special operating permits. External structures can be examined using scanning acoustic microscopy (SAM) technique that uses ultrasonic waves to detect delamination, voids and cracks in the IC package [9]-[10]. Acoustic microscopy offers high resolution for imaging certain on-die features. However, the technique requires long testing time, operator expertise and relatively expensive equipment. Electrical inspection methods include parametric tests, functional tests, burn-in tests and structural tests [9]. Parametric tests measure the AC and DC parameters of an IC. The functionality test is

used to verify different functions of the IC. Electrical, parametric and functionality tests require different test setups for different ICs and several types of counterfeits cannot be completely tested. Commercial and military grade ICs are distinguished by subjecting them to different temperature ranges in the burn-in test [11]. Terahertz imaging is also used for IC package inspection and chemical content mapping in biological objects. However, the resulting images do not offer better resolution than using X-ray imaging and still need to be analyzed and compared either visually or using image processing algorithms to identify differences [12]. Another method for counterfeit IC detection is by measuring and comparing near-field or far-field electromagnetic emissions of a suspect IC with an original [13]. A drawback of this method is that it requires IC-specific test setups, identical operating conditions and may depend on the firmware, if any, running on the IC. This method is also limited to ICs that produce or generate EM emissions and hence maybe not be applicable to low frequency circuits. Detection of the different levels of degradation inside an IC, based on measuring the light emissions from CMOS ICs, can be used to identify a counterfeit IC [14]. However, the method is not suited for high volume analysis, is time consuming and is susceptible to measurement error due to process variations. Recycled and aging ICs can be identified using an on-chip sensor based on the electromigration-induced aging effects [15]. Since this requires an on-chip sensor, the method cannot be used for ICs that do not have such an on-chip sensor and may not be possible to include such as sensor on all ICs due to technical or cost constraints. As discussed earlier, multiple parameters may lead to designating an IC a counterfeit and successful detection typically requires the use of a combination of a number of existing detection methods since each of the methods is focused on detecting a

specific feature or parameter. This makes the process time-consuming, expensive and potentially destructive.

Alternatively, a novel, relatively simple and powerful reflectometry-based measurement technique is proposed in this paper that makes use of measuring a wideband complex reflection coefficient from an IC illuminated with a high-frequency (microwave or millimeter wave) electromagnetic signal using an open-ended waveguide probe operating in its designated frequency band. The reflected electromagnetic (EM) signature of an IC, which is spatially-integrated over the aperture of the waveguide probe, is expected to vary as a function of different packaging material properties and the different interior electronic circuitry. Also as will be seen later, the developed *quantitative metric* used to differentiate between two ICs makes use of all frequency information (i.e., wideband reflection coefficient) over the waveguide frequency band. Hence, this metric is also spectrally integrated over the measured frequency band. The inherent *spatial* and *spectral* integration (i.e., sum of complex reflection coefficient information over spatial and frequency domains) process make this a unique and robust approach. Measurement results on several sets of ICs having the same package (DIP-14) and: *i*) different functionalities, *ii*) similar functionalities with slight differences in specifications, and *iii*) aged ICs are presented. The results illustrate the capability to differentiate ICs having slight differences in packaging material properties and/or electronic circuitry from a reference IC and a high degree of similarity in reflection properties of several ICs with identical specifications (i.e., a sample set of several of the same ICs).

2. METHOD AND MEASUREMENT SETUP

The proposed method for detection of dissimilar ICs is based on measuring their reflection coefficients by irradiating them with high-frequency electromagnetic (EM) signals using open-ended rectangular waveguides in the microwave and millimeter wave regimes, and particularly in this case at K-band (18-26.5 GHz) and Ka-band (26.5-40 GHz). The ICs are positioned over the aperture of a probing waveguide which is connected to the single port of a Vector Network Analyzer (VNA). To measure the single-port reflection coefficient (S_{11}) the system is calibrated at the waveguide aperture. Figure 2.1a shows the schematic of IC positioning over the waveguide aperture with the outer dimensions of the DIP-14 package and K-band (18-26.5 GHz) and Ka-band (26.5-40 GHz) waveguide apertures. It should be noted here that the reflected EM signature of an IC is sensitive to its relative positioning over the waveguide aperture. To ensure measurement repeatability and significantly reduce any differences caused by this aspect of the measurement setup, 3-D printed test fixtures, shown in Figure 2.1b, were designed and fabricated for the two waveguide apertures to facilitate accurate and repeatable positioning of the ICs over the respective waveguide apertures. Modified waveguide flanges were used that reduce unwanted reflections from the edges of the probing waveguide flanges, leading to a more robust reflection coefficient measurement [16]. The advantage of an aperture probe is that it produces a spatially integrated reflected EM signature by averaging the reflected signal over its aperture. Finally, the probing waveguide is connected to an Anritsu® 40 GHz vector network analyzer (VNA) via a coax-to-waveguide adapter to measure the wideband reflection coefficients (S_{11}) of the tested ICs. The entire measurement setup is shown in Figure 2.2a. To illustrate the type of

results obtained with these measurements, Figure 2.2b shows (in polar format) the measured complex reflection coefficient for five separate measurements of a given IC over the K-band (18-26.5 GHz) and Ka-band (26.5-40 GHz) frequency ranges, respectively. The results show excellent measurement repeatability afforded by this measurement method. In addition, it can be observed that the measured complex reflection coefficient (S_{11}) of the same IC is significantly different for the two frequency bands, as expected.

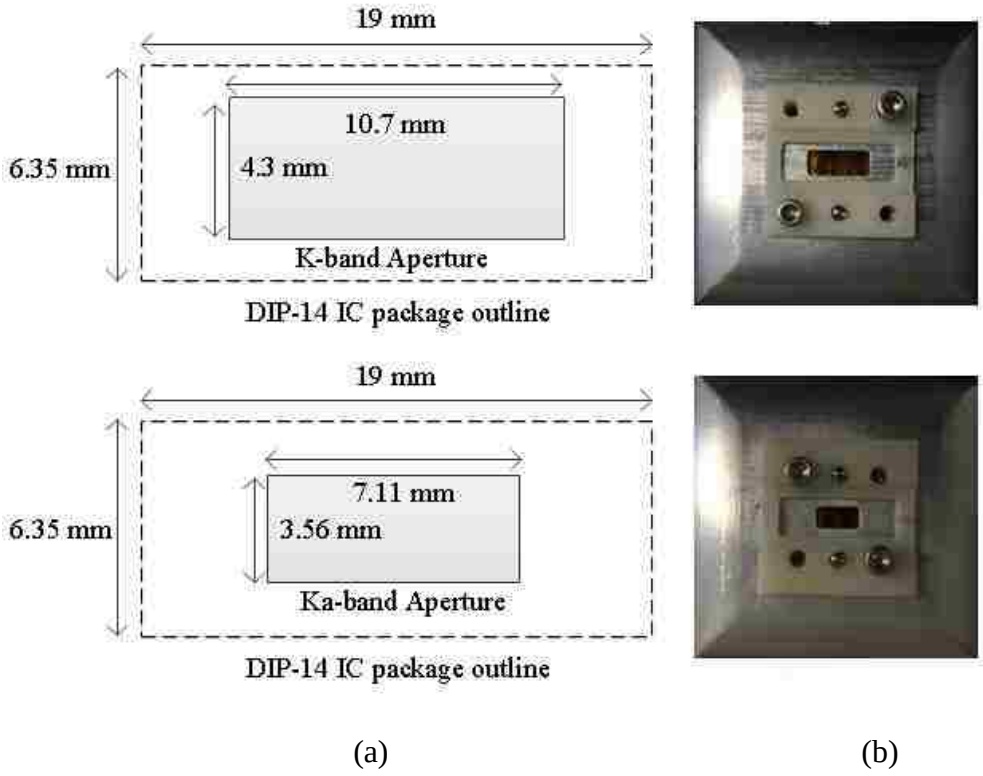

Figure 2.1 a) Schematic diagram of the IC outline positioning relative to the waveguide aperture for the K-band (18-26.5 GHz) and Ka-band (26.5-40 GHz) waveguides (not to scale), and b) pictures of the waveguide apertures with the 3D printed fixtures for accurate IC placement over the apertures.

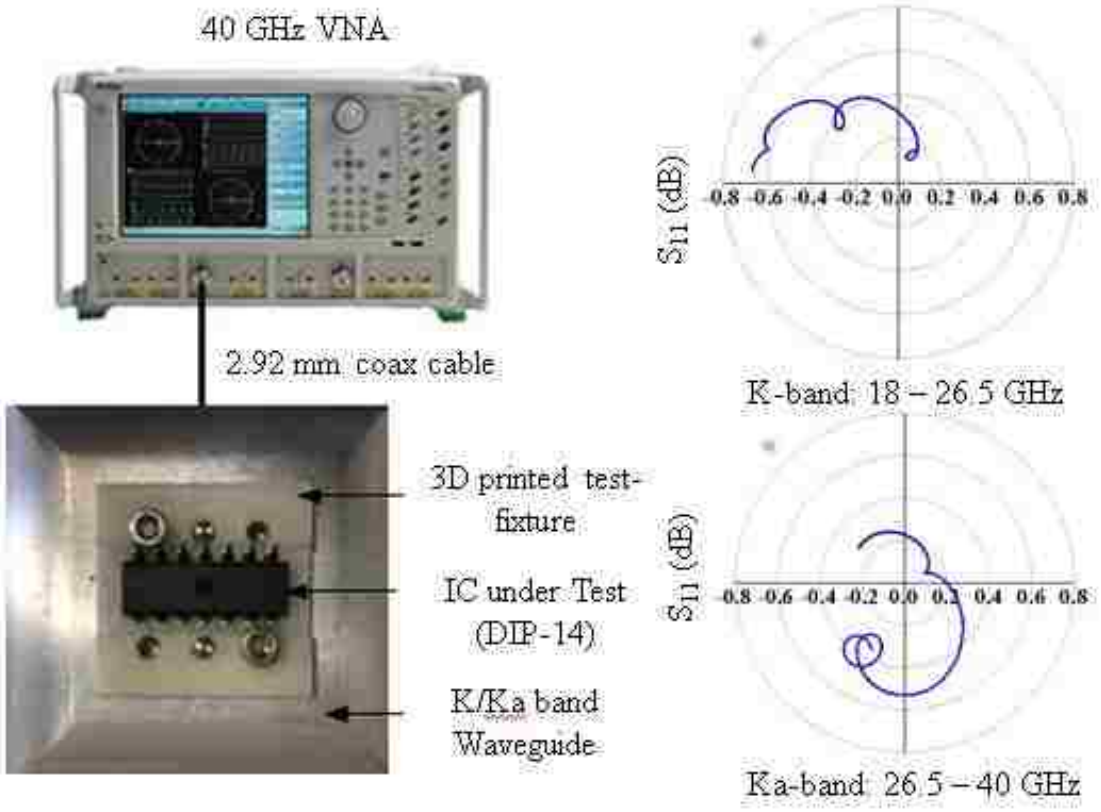

(a) (b)

Figure 2.2 a) Measurement setup for measuring reflection coefficient with K-/Ka-band waveguides and an IC (DIP-14 package), and b) measured complex wideband reflection coefficient (polar format) showing the excellent repeatability associated with five (5) separate measurements of the same IC.

Since the aperture dimensions and the frequency band of the two waveguides are different, the reflected signatures (S_{11}) are expected to be vastly different as well. Figure 2.3 shows the comparison of the measurement results between two functionally different ICs, namely: a dual precision timer (SA556N) and a quad Nand gate (CD4011BE) both having the same package (DIP-14). In addition, five test samples of each IC were measured at K-band (18-26.5 GHz) and Ka-band (26.5-40 GHz) to also check for differences in their wideband reflection coefficients (S_{11}) among different samples/units

of the same IC. These measurements were carried out to obtain a realistic understanding of the differences among the same samples/units of ICs, if any, as a result of manufacturing process and the measurement approach. This information is important for setting a measurement baseline by which slightly dissimilar ICs (i.e., counterfeits) may be detected. The results show that the variations for different samples/units of the same IC are insignificant as compared to differences between functionally different ICs. Furthermore, as also observed earlier, the reflection coefficients of these ICs are significantly different as a function of frequency in both bands. Upon careful observation we can see that the reflection coefficients for the SA556N and CD4011BE intersect or are the same at certain frequencies in both K-band (18-26.5 GHz) and Ka-band (26.5-40 GHz). Consequently, single-frequency measurements, at those specific frequencies, would not have resulted in the ICs being classified as different. On the other hand, wideband measurements are much more comprehensive and yield robust differentiation between two the ICs. These measurement results simply show an example of how the method can be used to differentiate between two ICs having the same package with different internal physical characteristics. Consequently, in practice a suspect or counterfeit IC can be rapidly measured and compared to a reference IC.

The next step in this process requires that a *quantitative metric* be developed and associated to the *differences* between these spatially- and spectrally-integrated (over the waveguide band) reflection coefficient characteristics. Such a metric enables rapid evaluation and comparison of ICs in a large throughput manufacturing or testing environment.

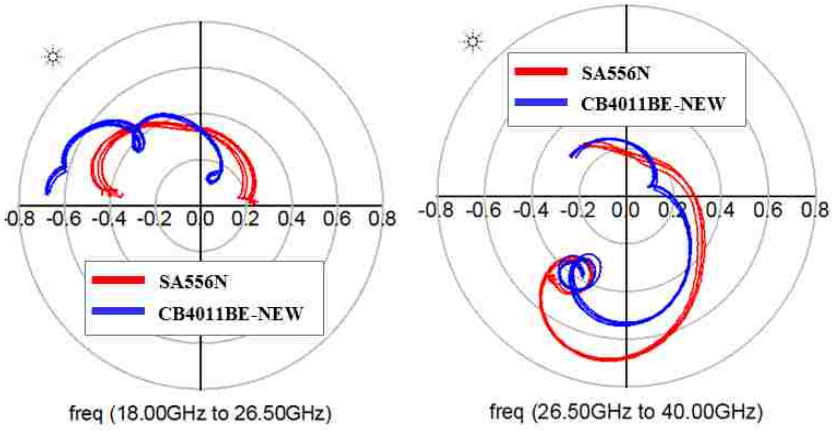

(a) (b)

Figure 2.3 Wideband reflection coefficient comparison between CD4011BE and SA556N at: a) K-band (18-26.5 GHz), and b) Ka-band (26.5-40 GHz).

Consequently, to evaluate the integrated degree of difference between the reflection coefficients, the root-mean-square error (RMSE) which is defined as the average Euclidean distance between two reflection coefficient vectors is used as the metric to distinguish between the measured S_{11} of two different ICs. RMSE values take into account the spatial properties as well as reflection properties of an IC over a wide range of measured frequencies. RMSE values also allows for rapid and automated calculation of the differences between the reflection coefficients of an unknown/suspect IC and its genuine/reference counterpart. RMSE values for measured S_{11} for each IC, $\Gamma(f)$, is calculated with respect to the average S_{11} of a reference IC, $\Gamma_{ref}(f)$, as follows:

$$RMSE = \sqrt{\frac{\sum_f^N |\Gamma(f) - \Gamma_{ref}(f)|^2}{N}} \qquad (1)$$

where *f* is the frequency and *N* represents the number of frequencies used in the measurement and calculation. For each waveguide band in this investigation 401 frequency points were measured. The general use of RSME is not new since it is an effective metric by which one can comprehensively delineate between two measured complex parameters over a wide frequency band or a pair of multi-dimensional vectors. As such similar metrics (i.e., complex or vector differences between two parameters) have been used for determining: *i*) differences between microwave synthetic aperture radar (SAR) images using uniform and non-uniform spatial sampling [17], *ii*) difference between reflection coefficient of a layered composite structure using open-ended waveguide probes with a finite and an infinite waveguide flange [18], *iii*) estimating degree of skin burns [19], and *iv*) cost function minimization when measuring layered fiberglass composites [20]. The use of RMSE as a *quantitative metric* is the first time it has been used in this particular type of reflectometry measurements for determining slight differences between ICs.

3. SELECTION OF TEST ICS

To verify the effectiveness of the proposed method a number of commercially-available ICs were obtained, as listed in Table I. Given the fact that no counterfeit IC was available for these measurements, and to demonstrate the efficacy of the proposed method for detecting counterfeit ICs, several ICs were chosen having slight performance characteristic differences, but with essentially the same functionalities. Also, all ICs had the same packaging specification (DIP-14) such that the external dimensions of all tested ICs were identical and visually indistinguishable. The tested ICs were selected such that they could be categorized into three groups to demonstrate the effectiveness of the method for testing multiple features/parameters that constitute different types of ICs. The objective was to test the method for distinguishing between the following groups:

A. ICs that are functionally different, i.e., having different part numbers.

B. ICs that are functionally similar; however, having slight differences in specifications such as: Mil and Industrial grades, different manufacturers, different supply voltage requirements, etc.

C. New and aged sets of Identical ICs.

ICs in Group C were provided by TRI/Austin which were first tested for basic logic and current draw and then were subjected to the following cyclical environmental stress screening sequence:

- Ten thermal cycles from -30°C to 130°C (below the Tg of the encapsulant) with 15 minute dwells at each temperature extreme, with no supply voltage exposure and subsequently inspected for logic and current draw.

- Forty-eight hours of exposure to mixed flowing corrosive gas (MFCG) at 400 PPM each of H2S, Cl2, NOx and SO4, with no supply voltage exposure, and then inspected for logic and current draw.
- Typically 72 hours of highly accelerated stress test (HAST) at 130°C and 22 PSI in biased mode at 50% duty cycle (1 hour on, 1 hour off), one cycle included only 48 hours of HAST exposure due to schedule conflict, inspect for logic and current draw.

Table 3.1 Table of tested ICs with part numbers, IC type/function, manufacturer, differences in specifications and number of tested samples for part.

Part Number	Type/Function	Manufacturer	Difference between IC's		No. of Samples
CD4011BE	NAND Gate	Hyundai	New	New vs. Aged	4
CD4011BE	NAND Gate	Hyundai	Aged		7
SA556N	Timer/Osc	Texas Instruments	-40–85°C	Temperature Range	5
NE556N	Timer/Osc	Texas Instruments	0–70°C		5
CD4541BE	Timer/Osc	Texas Instruments			5
PIC16F505	Microcontroller	Microchip		Different Parts	5
PIC16F506	Microcontroller	Microchip			5
SN74HC4066N	Analog switch	Texas Instruments	2 – 6 V	Supply Voltage Range	5
SN74AHC4066N	Analog switch	Texas Instruments	2 – 5.5 V		5
LM324AN	Op-Amp	Fairchild		Different Parts & Different Manufacturers	5
LM324N	Op-Amp	Fairchild			5
LM324AN	Op-Amp	Texas Instruments			5
LM324N	Op-Amp	Texas Instruments			5
LM224AN	Op-Amp	Texas Instruments		Different Parts	5

Table 3.1 Table of tested ICs with part numbers, IC type/function, manufacturer, differences in specifications and number of tested samples for part (cont.).

Part Number	Type/Function	Manufacturer	Difference between IC's		No. of Samples
LM224N	Op-Amp	Texas Instruments		Different Parts	5
SN75189N	Receiver	Texas Instruments			5
SN75189AN	Receiver	Texas Instruments			5
SN74HC86N	X-OR	Texas Instruments	2 – 6 V	Supply Voltage Range	5
SN74AHC86N	X-OR	Texas Instruments	4.5 – 5.5V		5
SN74AHC86N	X-OR	Texas Instruments	2 – 5.5 V		5
LM723CN	Linear Reg.	STMicroelectronics		Different Manufacturers	5
UA723CN	Linear Reg.	Texas Instruments			5
TL497ACN	DC-DC Boost conv.	Texas Instruments	0 – 70 °C	Operating Temperature Range	5
TL497AIN	DC-DC Boost conv.	Texas Instruments	-40 – 85°C		5
MCP4902	DAC	Microchip			5

4. RESULTS AND ANALYSIS

The approach described in Section II was used to calculate RMSE values for the ICs listed in Table I, between the CD4011BE-New IC (as the reference IC) and all other functionally different ICs (Group A). For comparison, RMSE values are plotted in Figure 4 and 5 for K-band (18-26.5 GHz) and Ka-band (26.5-40 GHz), respectively. CD4011BE-New was arbitrarily chosen as the reference IC for this comparison in order to illustrate relative numbers associated with RSME values. The red circles indicate the average value of each given set of measurements for the specific IC indicated. In addition, Figure 4 and 5 are drawn with the same scale to facilitate an easier comparison of RMSE values for each frequency band. To have a better understanding of the differences in the reflection coefficient RMSE values, X-ray images of all the ICs were also obtained at the ARTLAB (at Missouri University of Science and Technology). The IC orientation for obtaining the X-ray images is shown in Figure 4.3. To allow for comparison between the X-ray images and identification of differences between the internal structures, all the IC samples were oriented in the same way – with the notch on the right side of the images.

The X-ray images of the ICs compared in Figure 4.1 and 4.2 are shown in Figure 4.4. The results indicate some important facts, namely:

- the five independent RSME measurements associated with each individual IC is tightly grouped indicating the high degree of measurement repeatability and robustness associated with this technique,

- the relative difference between the RSME for each IC and the reference IC is substantial, indicating the relative ease by which ICs may be individually differentiated, and
- the results of the reflected EM signatures are consistent with our expectations, as RMSE values are larger when there is a larger physical difference in the interconnect layout as corroborated by the X-ray images.

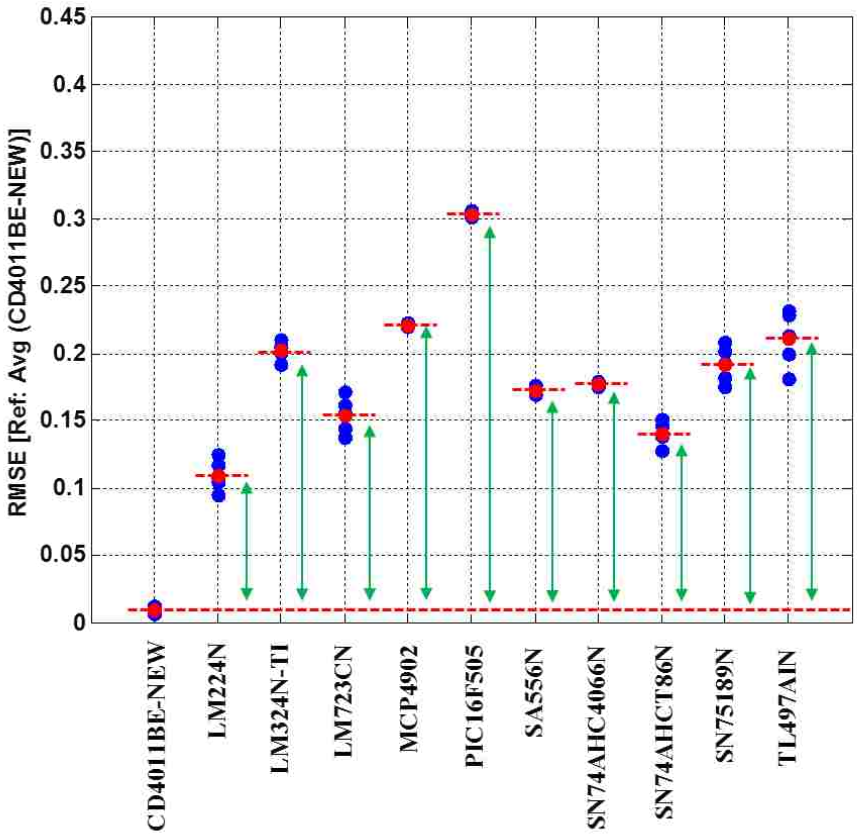

Figure 4.1 RMSE values of the reflection coefficient measured at K-band (18-26.5 GHz) for Group-A ICs (functionally different) referenced to the mean value of RMSE values of the reference IC: CD4011BE-NEW.

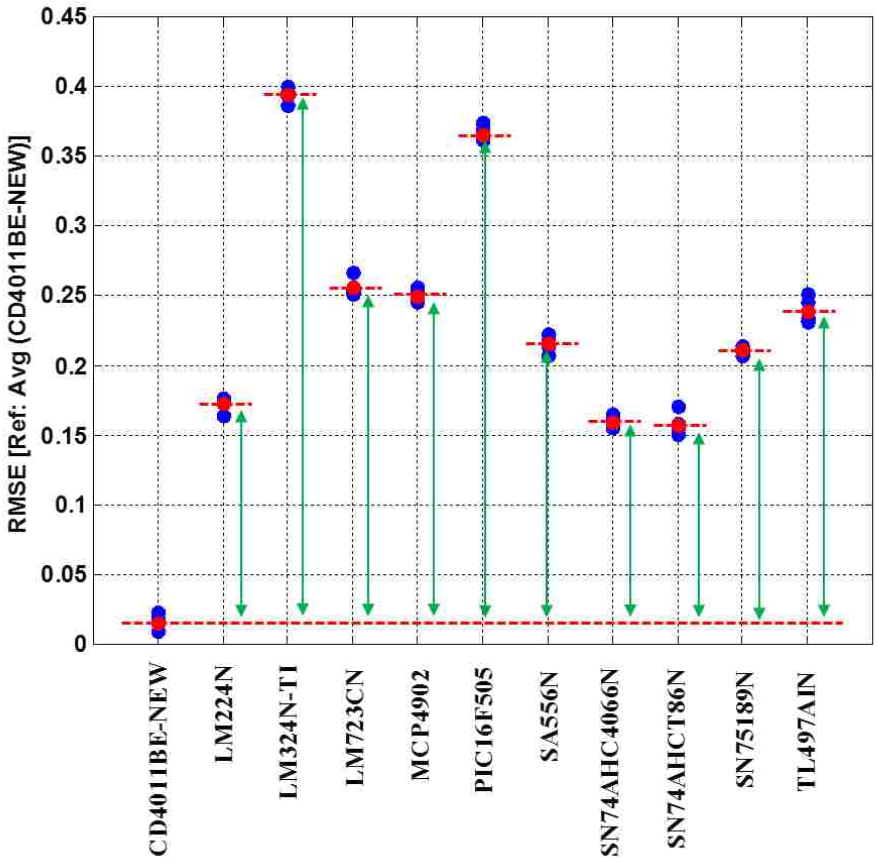

Figure 4.2 RMSE values of the reflection coefficient measured at Ka-band (26.5-40 GHz) for Group-A ICs (functionally different) referenced to the mean value of the RMS error of the reference IC: CD4011BE-NEW.

Figure 4.3 Orientation of the IC samples used for obtaining the X-ray images.

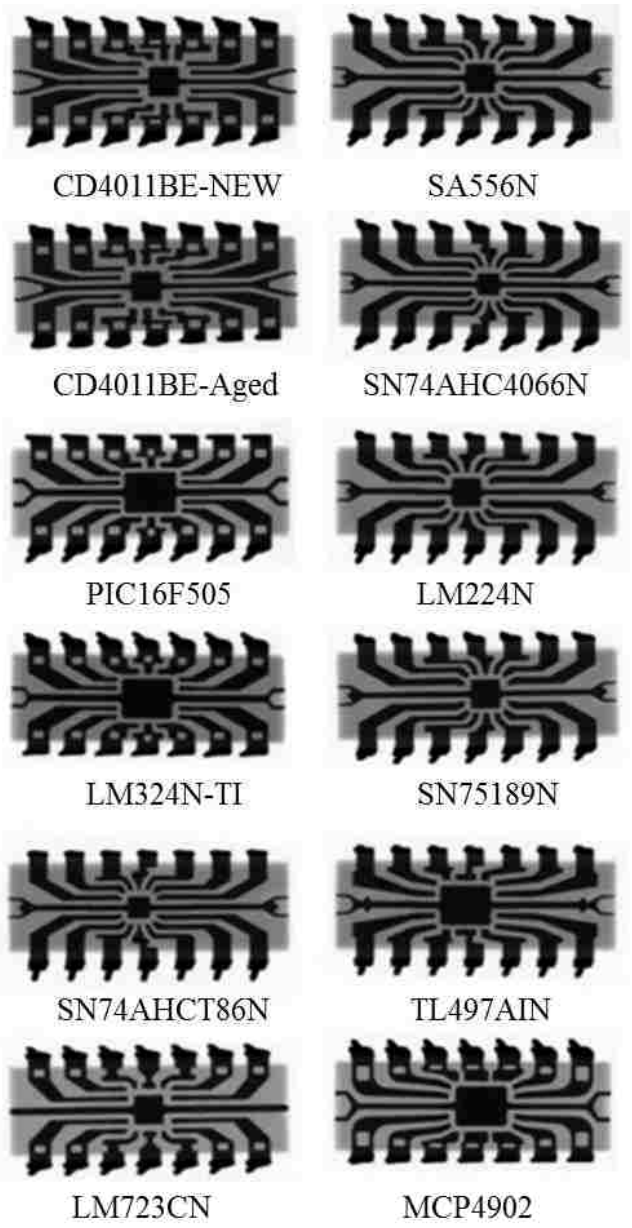

Figure 4.4 X-ray images showing the internal metal structures like die area, bond wires, interconnects and external pins of the tested ICs.

For comparing the differences between functionally similar ICs having slightly different specifications such as: Mil and Industrial grades, different manufacturers, different supply voltage requirements, etc. (Group B) and comparing between “new

(good)" vs. "aged (old)" (Group C) a similar measurement and RMSE value calculation procedure was followed. One of the ICs from each pair was used as the reference for RMSE value calculations of a slightly dissimilar IC. In such cases, differences in RMSE values indicate slight differences in the ICs that may or may not be visually obvious or by other inspection methods. The RMSE value comparisons and the X-ray images of the ICs for Group B and Group C at K-band (18-26.5 GHz) and Ka-band (26.5-40 GHz) are shown in Figure 4.5 and 4.5, respectively. The actual functionality differences in the IC parameters can be obtained by referring to the Table-I. Typically, there may be one or more IC parameters that are different between a given IC pairs being compared, and the combined effects of such differences result in different RMSE values that enable differentiation between the two ICs.

As mentioned earlier, the red circle indicates the mean value of RSME for the reference IC.

Figure 4.5a and 4.6a show RMSE values and X-ray images of two timer ICs (SA556N and NE556N) with identical specifications except different operating free-air temperature ranges. As can be observed from the X-ray images, these ICs have slightly different internal interconnect and relative die location and are also expected to have some differences in the plastic package material since they operate at different temperature ranges [21]. The clear differences between their RMSE values are due to these variations, enabling distinction between the two ICs. In addition and as expected, the higher difference in RMSE values for Ka-band (26.5-40 GHz) is attributed to the smaller aperture size and wavelength at these frequencies that result in these larger differences. It must be mentioned here that although the differences in the internal

physical interconnect layouts can be observed from the X-ray images, differences in the plastic packages of the two ICs, if any, are not apparent from the X-ray images.

Figure 4.5b and 4.6b show RMSE values and X-ray images of two DC-to-DC boost converter ICs (TL497AIN and TL497ACN) with identical specifications except for different operating free-air temperature ranges. The X-ray images are nearly identical for the two ICs. However, RMSE values for the two ICs are measurably different even though the internal interconnect layouts are nearly identical. The differences in RMSE values most likely result from differences in the plastic package materials used, as explained above. RMSE values as a function of frequency also follow the same trends as those in Figure 4.5a and 4.6a.

Figure 4.5c and 4.6c show the comparison of RMSE values and X-ray images between two analog switches (SN74HC4066N and SN74AHC4066N) having identical specifications except slight differences in the supply voltage range of operation. The X-ray images show that the internal interconnect layout is different and may also have slight differences in the electronic circuits in the IC die/chip resulting in differences in RMSE values.

Figure 4.5d and 4.6d shows another comparison of RMSE values and X-ray images of two ICs, XOR gates (SN74HC86N and SN74AHCT4066N), having identical specifications except slight differences in the supply voltage range of operation. The X-ray images show that the internal interconnect layout is quite different and may also have slight differences in the electronic circuits in the IC die/chip resulting in differences in RMSE values.

Figure 4.5e and 4.6e show the comparison of RMSE values and X-ray images between two linear regulators (LM723CN and UA723CN) having identical specifications from two different manufacturers. The X-ray images show that the internal interconnect layout is quite different and may also have slight differences in the electronic circuits in the IC die/chip resulting in differences in RMSE values.

Figure 4.5f, 4.6f, 4.5g and 4.6g show the comparison of RMSE values and X-ray images between two sets of op-amps (LM324N-TI, LM324AN-FC, LM324N-TI and LM324N-FC) having identical specifications from two different manufactures. The X-ray images show that the internal interconnect layout is quite different and may also have slight differences in the electronic circuits in the IC die/chip resulting in differences in RMSE values.

Figure 4.5h, 4.6h, 4.5i and 4.6i show the comparison of RMSE values and X-ray images between two sets of op-amps (LM324N-TI and LM324AN-TI, LM224N-TI and LM224AN-TI) having identical specifications from the same manufacturer with different series of part numbers. The X-ray images show that the internal interconnect layouts are quite different and may also have slight differences in the electronic circuits in the IC die/chip resulting in differences in RMSE values.

Figure 4.5j and 4.6j show the comparison of RMSE values and X-ray images between identical NAND gates (CD4011BE-New and CD4011BE-Aged) with different conditions: “new” and “old/aged”. As expected, the X-ray images show no differences between the two ICs being that they are electronically identical. Nevertheless, differences in the RMSE values are observed between the two ICs, which are attributed to the changes in the plastic package material caused by the aging process, as microwave and

millimeter wave signals interact with different materials differently and can distinguish materials changes [22]. These results show the effectiveness of the proposed method over X-ray imaging to detect changes in the package materials caused by aging. Another important observation is that the variation between RMSE values is larger for the five samples of the “old or aged” ICs as compared to the different samples of the “new” ICs. This is attributed to the likely changes in the plastic package materials of the “old/aged” ICs as compared to the more consistent material properties of the “new” ICs. Therefore, in addition to comparing RMSE values between the “new” and “old/aged”, the variation of the RMSE values among identical ICs could be used as a metric to distinguish between “new” and “old/aged” ICs.

The comparison of RMSE values and X-ray images shown in Figure 4.5 and 4.6 demonstrate the effectiveness of the proposed method for differentiating between ICs having one or more slight dissimilarities in the forms of: internal interconnect layout, die size, missing bond wires, on-die electronic circuitry and plastic package material characteristics. Furthermore, the results indicate that RMSE values are larger when there are larger physical differences in the interconnect layout as corroborated by the X-ray images. The data presented here also clearly point to the significant potential this testing method offers for detecting a wide range of *counterfeit* (intentionally tampered with or illegally manufactured) and *aged* ICs.

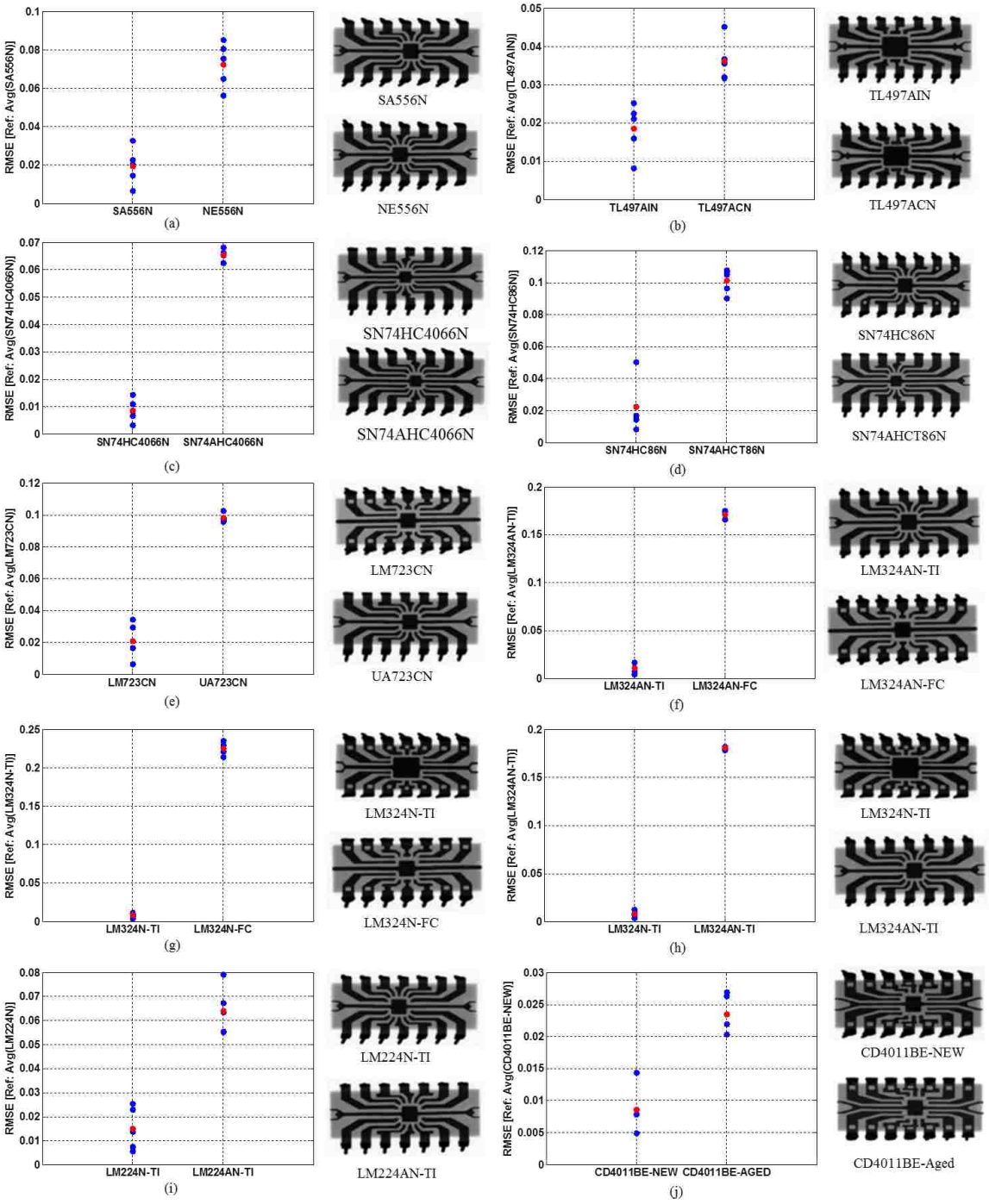

Figure 4.5 RMSE values measured at K-band (18-26.5 GHz) for Group-B and Group-C IC comparisons (functionally the same but with different electrical specifications) referenced to the mean value of the RMSE of one of the ICs from each pair.

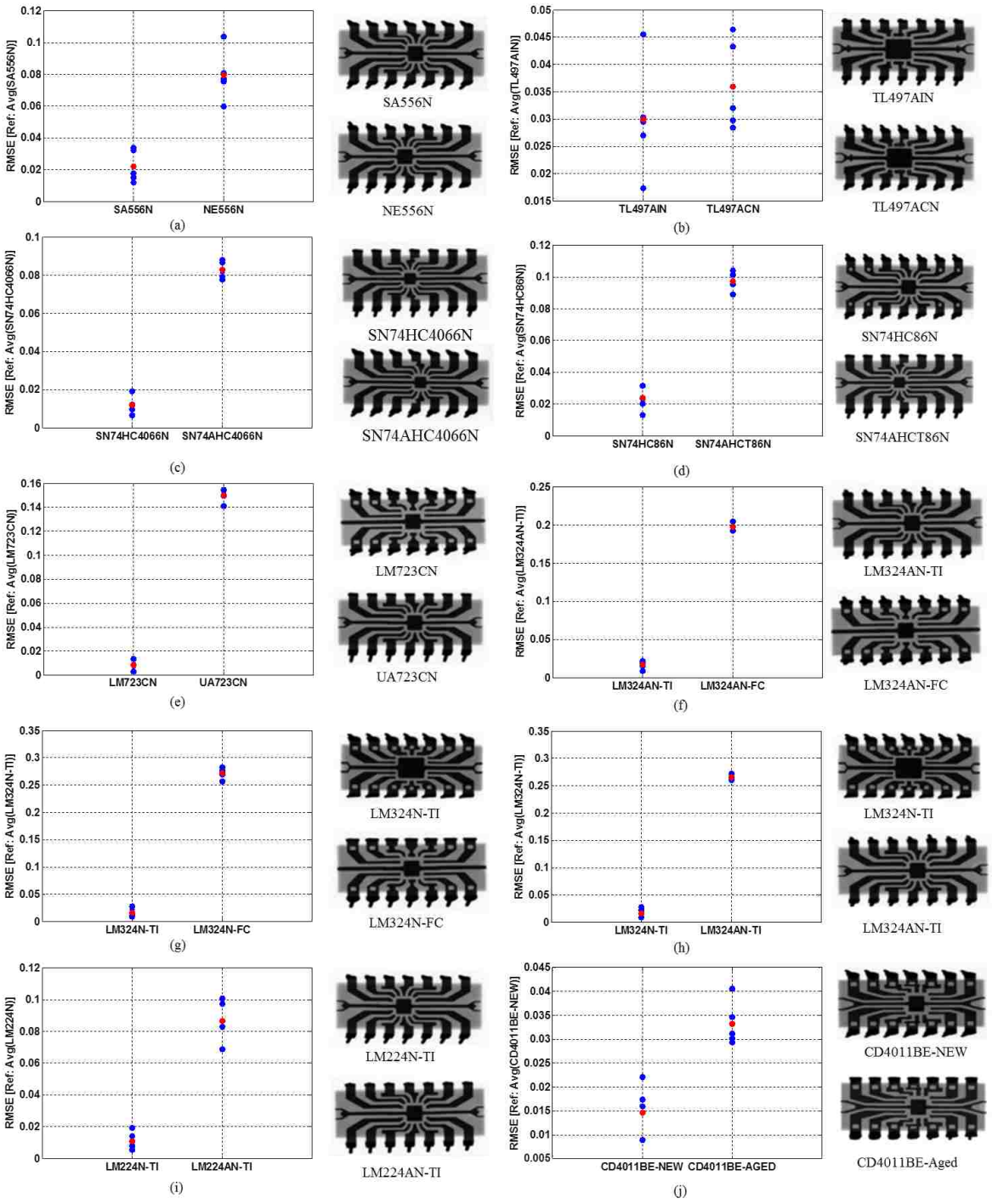

Figure 4.6 RMSE values measured at Ka-band (26.5-40 GHz) for Group-B and Group-C IC comparisons (functionally the same but with different electrical specifications) referenced to the mean value of the RMSE of one of the ICs from each pair.

5. CONCLUSION

A wideband microwave method for the rapid detection of slightly dissimilar and aging integrated circuits (IC) using a wideband microwave reflectometry measurement is presented. The reflected electromagnetic (EM) signature of an IC varies as a function of different material properties and its physical and geometrical interior electronic circuitry which is the basis for this technique. The advantage of this method is in its ability to detect slight changes caused by a plurality of parameters such as: change in interconnect layout, missing bond wires, changes in the material properties of the plastic package due to temperature, humidity and other aging factors, in a single measurement. The effectiveness of the method to detect slight changes caused by change in packaging material as well as electronic circuitry of many ICs were demonstrated by comparing the reflected EM signatures of ICs having the same physical package dimensions (DIP-14) but being: functionally different, functionally similar with slightly different electrical specifications and "new" and "aged" ICs. Root-mean-square error (RMSE) which is defined as the average Euclidean distance between two reflection coefficients was used as the quantitative *metric* to distinguish between the measured S_{11} of two different ICs. In an attempt to better understand the differences in the reflected EM signatures, X-ray images of all the ICs were also obtained for comparison.

The results indicated that RMSE values are larger when there are larger physical differences in the interconnect layout, as expected and corroborated by the X-ray images. Also, the difference between RMSE values are larger for Ka-band (26.5-40 GHz) as compared to K-band (18-26.5 GHz) since at the higher frequencies of Ka-band, the refection coefficient is more sensitive to changes in the various parameters such as

interconnect layout, die size, package material characteristics, etc. Moreover, potential differences in the manufacturing processes of different companies producing the same IC design can be distinguished as observed from the IC samples of LM723CN (STMicroelectronics) and UA723CN (Texas Instruments). The method shows that ICs with slight variations can be distinguished and hence the method has a great potential for detecting counterfeit ICs which may:

- be manufactured by an unauthorized manufacturer and may have been produced using a different manufacturing process,
- have a hardware trojan, malicious additional/modification of circuitry, designed to disable, destroy or leak confidential information,
- be recycled original ICs sold as "new" or different specifications after remarking, and
- be non-functional ICs with missing die or bond wires with the same external package and pin count (e.g., DIP-14, TSOP, etc.).

It is important to note that even though for certain cases the X-ray images did not show obvious differences, clear differences in the RMSE values were observed. These are attributed to differences in the die structures and/or package material differences, etc. These results indicate the advantages of the proposed method over existing counterfeit detection methods. A limitation of the method is that although differences or deviations from the expected EM signatures can be used to distinguish between original and counterfeit or aged ICs, the actual physical differences cannot be determined. However, when one is interested in quickly evaluating differences among a set of ICs, this method is clearly robust, useful and very attractive.

6. ACKNOWLEDGEMENT

The authors would like to thank Ashish Avachat, Ph.D. candidate, and Dr. Hyoung Koo Lee from Advanced Radiography and Tomography Laboratory (ARTLAB) for helping us obtain the X-ray images.

The authors would like to thank Dr. David Pommerenke (EMC-laboratory, Missouri S&T, Rolla, MO) for his help and support towards this work.

The authors would like to thank Mr. R. Austin at TRI/Austin for providing the test samples for the aged ICs for this work.

REFERENCES

[1] M. Pecht and S. Tiku, "Bogus: electronic manufacturing and consumers confront a rising tide of counterfeit electronics," *IEEE Spectrum*, vol. 43, no. 5, pp. 37–46, 2006.

[2] S. Bastia, ''Next generation technologies to combat counterfeiting of electronic components,'' *IEEE Trans. Compon. Packag. Technol.*, vol. 25, no. 1, pp. 175–176, Mar. 2002.

[3] Semiconductor Industry Association (SIA), ''Winning the battle against counterfeit semiconductor products,'' Aug. 2013.

[4] N. Kae-Nune and S. Pesseguier, ''Qualification and testing process to implement anti-counterfeiting technologies into IC packages,'' *Proc. Design Autom. Test Eur. Conf.*, 2013, pp. 1131–1136.

[5] U. Guin, M. Tehranipoor, D. DiMase, and M. Megrdician, ''Counterfeit IC detection and challenges ahead,'' in *ACM SIGDA E-Newslett.*, vol. 43, no. 3, Mar. 2013.

[6] U. Guin, D. DiMase and M. Tehranipoor, ''A comprehensive framework for counterfeit defect coverage analysis and detection assessment,'' *J. Electron. Testing*, vol. 30, no. 1, pp. 25–40, 2014.

[7] U. Guin, D. DiMase, M. Tehranipoor, "Counterfeit Integrated Circuits: Detection, Avoidance, and the challenges ahead," *Journal of Electronic Testing*, 2014.

[8] J. Goldstein et al., Scanning Electron Microscopy and X-ray Microanalysis. New York, NY, USA: Springer-Verlag, 2003.

[9] Jones J (2009) Counterfeit components and acoustic microscopy.

[10] Yong Han Ng; Yew Hock Low; Serge Demidenko, "Improving Efficiency of IC Burn-In Testing," *Instrumentation and Measurement Technology Conference Proceedings*, 2008.

[11] U. Guin et al. , "Counterfeit integrated circuits: A rising threat in the global semiconductor supply chain," Proc. IEEE, vol. 102, no. 8, pp. 1207–1228, Aug. 2014.

[12] B. Hu and M. Nuss, ''Imaging with terahertz waves,'' Opt. Lett. , vol. 20, no. 16, pp. 1716–1718, 1995.

[13] He Huang, Alexandre Boyer, Sonia Ben Dhia, "The detection of counterfeit integrated circuit by the use of electromagnetic fingerprint," *EMC Europe 2014*, Sep 2014, Gothenburg, Sweden, pp.1-5, 2014.

[14] K. He, X. Huang and S. Tan, "EM-Based On-Chip Aging Sensor for Detection of Recycled ICs" *IEEE Design and Test*, vol. 33, no. 5, pp. 56-64, Jun. 2016

[15] P. Song and et. al., "Counterfeit IC detection using light emission," in *ITC*, 2014.

[16] M. Kempin, M.T. Ghasr, J.T. Case, and R. Zoughi, "Modified waveguide flange for evaluation of stratified composites," *IEEE Trans. Instrum. Meas*., vol. 63, no. 6, pp. 1524–1534, Jun. 2014.

[17] J.T. Case, M.T. Ghasr, and R. Zoughi, "Optimum 2-D Non-uniform Spatial Sampling for Microwave SAR-Based NDE Imaging Systems," *IEEE Trans. Instrum. Meas*., vol. 61, no. 11, pp. 3072- 3083, November 2012.

[18] M.T. Ghasr, D. Simms and R. Zoughi, "Multimodal Solution for a Waveguide Radiating into Multilayered Structures - Dielectric Property and Thickness Evaluation," *IEEE Trans. Instrum. Meas*., vol. 58, no. 5, pp. 1505-1513, May 2009.

[19] Y. Gao, and R. Zoughi, "Millimeter Wave Reflectometry and Imaging as Effective Diagnostic Tools for Skin Burn Injuries," *IEEE Trans. Instrum. Meas*., 2016 (available on Early-Access – DOI 10.1109/TIM.2016.2620778).

[20] M.T. Ghasr, M.J. Horst, M. Lechuga, R. Rapoza, C. Renoud and R. Zoughi, "Accurate One-Sided Microwave Thickness Evaluation of Lined-Fiberglass Composites," *IEEE Trans. Instrum. Meas*., vol. 64, no. 10, pp. 2802-2812, October 2015.

[21] Vassighi, Arman; Sachdev, Manoj (2006). Thermal and Power Management of Integrated Circuits. Integrated Circuits and Systems.

[22] R. Zoughi, *Microwave Non-Destructive Testing and Evaluation*. The Netherlands: Kluwer, 2000.

IV. RADIATED EMI ESTIMATION FROM DC-DC CONVERTERS WITH ATTACHED CABLES BASED ON TERMINAL EQUIVALENT CIRCUIT MODELING

Satyajeet Shinde, *Student Member, IEEE,* Kohei Masuda,Guangyao Shen, Abhishek Patnaik, Tamar Makharashvili, , David Pommerenke, *Fellow, IEEE,* Victor Khilkevich, *Member, IEEE*

ABSTRACT

An equivalent two terminal model based on Thevenin equivalents describes the common mode currents on the input and output side of two widely used types of DC-to-DC power converters - buck and boost. Thus, it describes a non linear circuit by a linear equivalent circuit. The maximized spectrum of the common mode currents is extracted for converters with stochastic signals using a novel characterization procedure. The extracted Thevenin model is used in co-simulation combined with a full-wave EM solver to predict the radiated emissions from the system consisting of the shielded DC-DC converters with attached cables and a DC brushless motor as load. The results using the terminal model agree well with the measurements providing that the actual common mode loads are within the range of common mode loads used while obtaining the Thevenin equivalent circuit.

Index Terms— terminal model, characterization loads, stochastic behavior, radiated emissions, co-simulation, DC-DC converter.

1. INTRODUCTION

Modeling the radiated emissions from a power converter circuit with attached cables, as shown in Figure 1.1, is challenging due to the presence of multiple coupling mechanisms within the power electronic system that can influence the radiated EMI from the system. Additional complexity is introduced due to DC-DC converters with stochastic behavior.

Extensive work has been done for predicting conducted and radiated EMI from power converter systems using various methodologies such as Spice-like lumped circuit modeling, full wave electromagnetic modeling, behavioral modeling, etc. The most common methodology is the time domain Spice-like circuit modelling. It is based on adding parasitics to the power converter circuit and using more sophisticated physics based semi-conductor models to obtain a good EMC representation of the actual circuit [1]-[6]. This method has the difficulty that it is very time consuming to obtain, and verify the complete models and it is not always easy to know which parasitics need to be added. The usable frequency range of the final model depends on the added parasitics and accuracy of the semi-conductor models.

Hybrid modeling techniques that involve full wave electromagnetic modeling of the PCB and chassis components along with circuit simulation allow the calculation of the complex electromagnetic interaction between the high dv/dt switching terminals and heat sink to predict the conducted and radiated emissions from the system [7]-[11]. However such models are time consuming to build and verify and are computationally expensive.

Behavioral terminal models based on optimization of the Thevenin equivalents for predicting conducted differential mode (DM) and common mode (CM) noise up to 50 MHz for test impedances within the characterization range have been demonstrated in [12]-[16]. A linear two terminal equivalent noise source model has been proposed to model the common mode noise driven on to the input and output side cables from two common topologies of DC-to-DC power converters [17]. This model however did not consider the stochastic behavior of converters and the accuracy of the model for test impedances outside the characterization range was not analyzed.

A terminal frequency domain equivalent noise source model for power converter circuits does not need the knowledge of the coupling mechanisms as it describes the circuit behavior. DC-to-DC converter emissions are non-linear with respect to various differential and common-mode load impedances. As a result the accuracy of using a linear model for modeling the emissions in a specific application may depend on the load conditions used during the characterization of the converters.

This paper extends the work on terminal modeling and shows for the first time the parameters needed to successfully extract a Thevenin equivalent circuit for EMI prediction of DCDC converters and its application to a real system for EMI prediction. Two examples, one boost and one using a buck converter topology are used to illustrate the process and its limits. The main goal of this research is the prediction of radiated emissions from the cables attached to the converter in setups similar to radiated EMI standards like CISPR 25, DS160E, MIL-STD 461with the power converter circuit and cables placed 5 cm above the horizontal reference plane [18]-[20]. Table I details the advantages and limitations of various existing and proposed modeling methodologies.

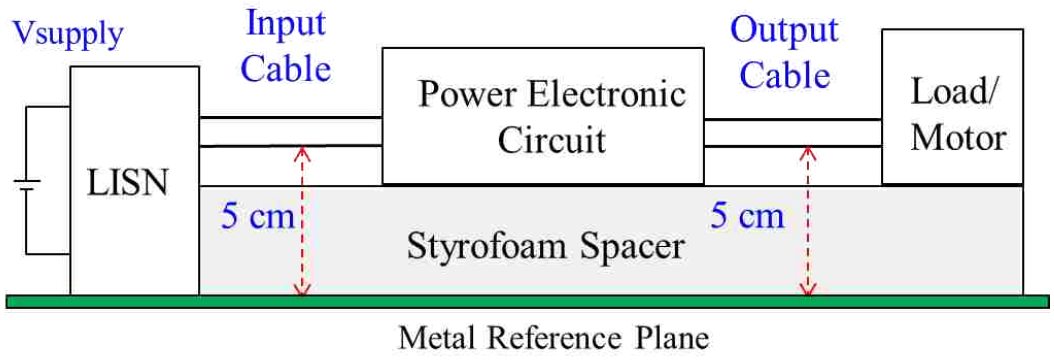

Figure 1.1 Schematic of a typical test setup for a power electronic system for radiated EMI measurements.

The extracted equivalent models are incorporated into a full-wave EM solver along with the common mode structures – attached cables, LISN and a brushless DC motor, used as load, to predict the radiated emissions at 1 m distance. The limitations and sources of error of the proposed two-terminal linear model are discussed with respect to the parameters that are involved during the characterization of the converters.

Table 1.1 Advantages and limitations of various modelling methods used for emissions predictions from power electronic circuits.

Modeling Method	Advantages/Merits	Limitations
Lumped Circuit Modeling	• Accurate representation of the circuit. • Ability to predict differential and common mode emissions. • Influence of individual circuit components on the emissions can be analyzed.	• Usable frequency range of the final model depends on the added parasitics and accuracy of the semi-conductor models. • Time consuming to obtain complete models and not always easy to know which parasitics need to be added.
Hybrid Modeling Techniques (Co-simulation of Spice circuit in Full wave solver)	• Effect of component placement and PCB layout can be evaluated for improving the designs. • Direct radiation from circuit PCB can be predicted.	• Time consuming to build and verify the model. • Computationally expensive. • Needs semiconductor models valid up to a few hundred MHz. • Requires details of the physical geometry details of the structures like heat sink.
Behavioral/Terminal Equivalent Modeling for Maximized spectrum prediction	• Does not need the knowledge of the coupling mechanisms as it describes the circuit behavior. • Relatively fast method to create models for prediction of emissions from different converters. • Maximized spectrum prediction.	• Accuracy of the extracted model depends on the characterization range and actual impedances of the real system/application. • Requires a working electronic circuit. • Influence of the circuit components and PCB layout on the emissions cannot be analyzed. • Direct radiation from circuit PCB cannot be predicted.

2. COMMON-MODE EQUIVALENT TERMINAL MODEL & RADIATED EMI PREDICTION METHODOLOGY

For testing the proposed methodology for radiated emissions based on terminal equivalent circuit modeling, we consider a system consisting of two cables attached to the input and output side of the power converter to a LISN and brushless DC motor respectively placed 5 cm above a horizontal reference plane. Based on the proposed methodology an equivalent linear circuit model of the power electronic circuit needs to be extracted using terminal characterization. As mentioned earlier, for radiated emissions prediction from the described setup, the common mode currents including their return current paths are the dominant sources of radiation from the system. As a result, a terminal model characterization based on common mode and their return path currents is required. While a variety of model topologies are possible we selected the Thevenin's equivalent source model comprising of two sources and three complex impedances to represent the extracted equivalent model of the power converter for its simplicity. The terminal equivalent circuit, shown in Figure 2.1, is derived by measuring the common mode currents on the input side and output side of the converter circuit for various common mode load impedances, henceforth referred to as characterization impedances, connected to the input and output side of the converter. Common mode load impedances refer to the common mode terminations of the input and output side terminals to the measurement reference planes – implemented using resistors via DC-block capacitors. Five sets of currents for different load conditions are required to solve for the five unknown quantities – three impedances and two voltage sources (1). It must be reiterated here that the derived model based on the measured current for various common mode

load impedances is a linear model for modeling the non-linear behavior of the power converter circuit. The common mode currents for various conditions are recorded in time domain using an oscilloscope and converted into frequency domain using FFT with flattop window. The equations are solved at all frequencies in the frequency range (30 MHz-to-250 MHz) to obtain the Vs1, Vs2, Zs, Zsi and Zso complex parameters of the equivalent circuit, shown in Figure 2.1. During these RF measurements the DC load is kept constant and at the same value which is used during the radiated emission measurements.

$$\begin{bmatrix} -Ii1\ 0\ -(Ii1+Io1)1\ 0 \\ 0\ -Io1-(Ii1+Io1)1\ 0 \\ -Ii2\ 0\ -(Ii2+Io2)1\ 0 \\ 0\ -Io2-(Ii2+Io2)1\ 0 \\ -Ii3\ 0\ -(Ii3+I3)1\ 0 \end{bmatrix} \begin{bmatrix} zsi \\ zso \\ zs \\ vs1 \\ vs2 \end{bmatrix} = \begin{bmatrix} Zi1 * Iin1 \\ Zo1 * Io1 \\ Zin2 * Ii2 \\ Zo2 * Io2 \\ Zi3 * Ii3 \end{bmatrix} \quad (1)$$

The steps for calculating the equivalent circuit model and radiated emissions prediction due to the common mode currents of the DC-DC converters are summarized in Figure 2.2. The characterization range is the range of common mode load impedances on both input and output sides of the converter that are used to obtain the equivalent circuit model. The common mode load impedances (complex) on the input and output side of the converters determine the characterization range of the converters.

The characterization range limits the usable range of the derived model to input and output common mode loads that are within the characterization range. For common mode loads that are far away from the characterization range, larger differences between the simulated and actual common mode currents occur, as the converter is a non-linear circuit modeled by a linear model.

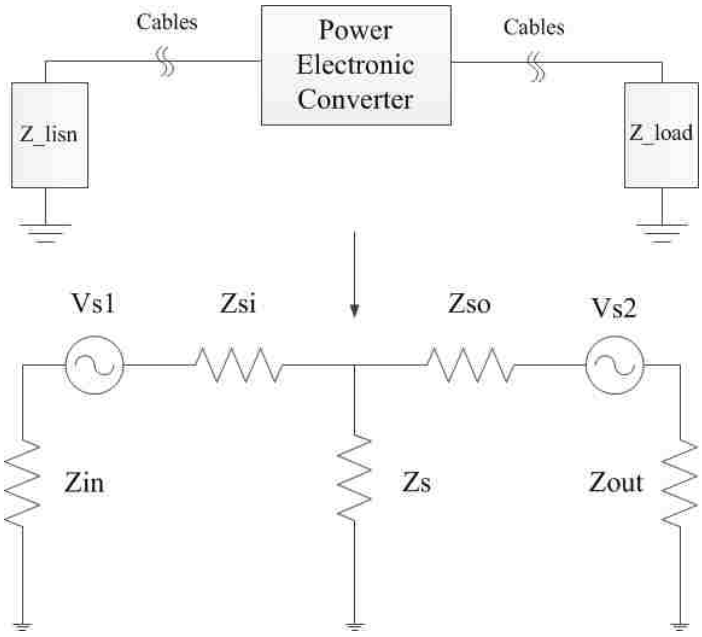

Figure 2.1 Two source terminal equivalent circuit model for the non linear power electronic circuit.

The methodology is tested on two typical DC-DC converters topologies:

- Non-Isolated buck converter (RT8032)
  - V_{in} = 12 V, V_{out} = 10 V, $F_{switching}$ = 1.2 MHz
- Non-isolated boost converter (PTN0405CAD)
  - Vin = 5 V, Vout = 15 V, $F_{switching}$ = 0.525 MHz

For radiated emissions prediction a three-step process is followed. First the Thevenin's equivalent source model is extracted based on common mode characterization of the converter to obtain the source impedances and voltage sources. In the second step the common mode structures of the attached cables, return paths and loads are incorporated in a full-wave EMC solver – CST Microwave studio. The DC-DC converter is substituted with a network of discrete ports that represent the sources and impedances

of the terminal equivalent model. The structure is simulated to obtain the frequency domain transfer function of the radiated fields at 1 m from the excitation ports. This simulation model can be re-used for other converters as long as the cable routing remains unchanged.

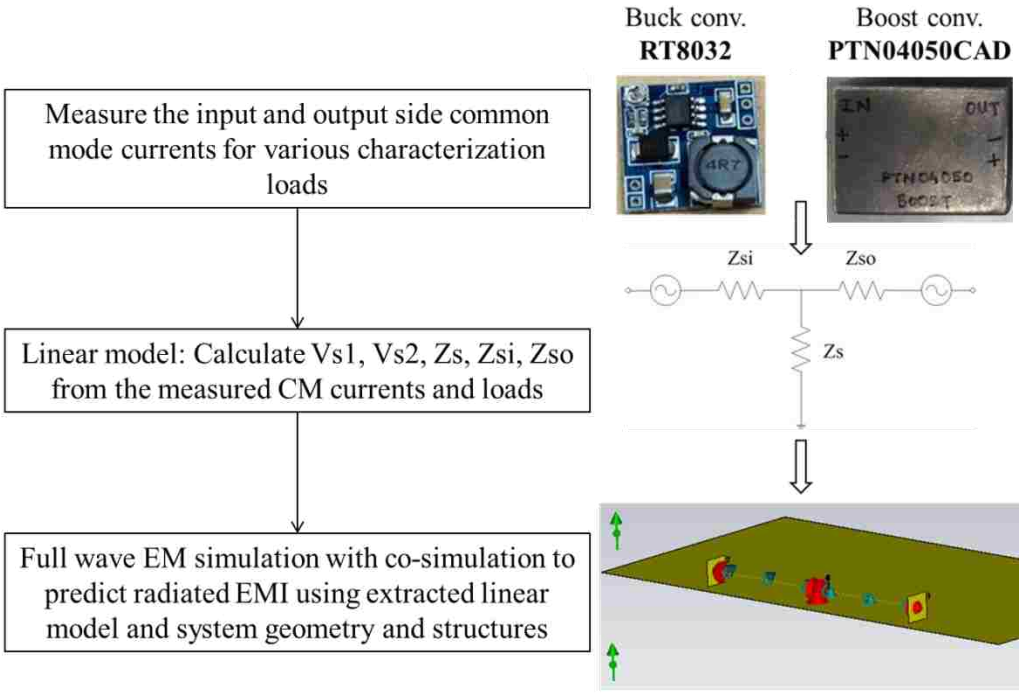

Figure 2.2 Steps for calculating the terminal equivalent model of the DC-DC converter circuits for estimating the common mode currents.

As the third step the calculated source impedances and voltage sources of the terminal equivalent model are incorporated into the transfer function block to recalculate the radiated emissions at 1 m distance using the extracted sources and impedances as a post-processing step. The method allows prediction of the radiated emissions from different power converter circuits based on terminal characterization without requiring

detailed knowledge of the circuit schematic, PCB layout, circuit parasitics or Spice-like simulation models of the components. The extracted model incorporates the complex parasitic coupling between the circuit elements, reference planes and any heat-sinks if present.

3. MEASUREMENT SETUPS & CHARACTERIZATION BOARD

A characterization board was designed as part of the measurement setup for common mode characterization of the DC-DC converters.

3.1 CHARACTERIZATION BOARD AND MEASUREMENT SETUP

The schematic of the characterization board and measurement setup is shown is Figure 3.1. The characterization board consists of the power supply for the converters, DC-block capacitors, capacitors to suppress the differential model noise and resistors at the input and output side of the converter that function as common mode impedances. The common mode current on the input and output side are measured using an oscilloscope.

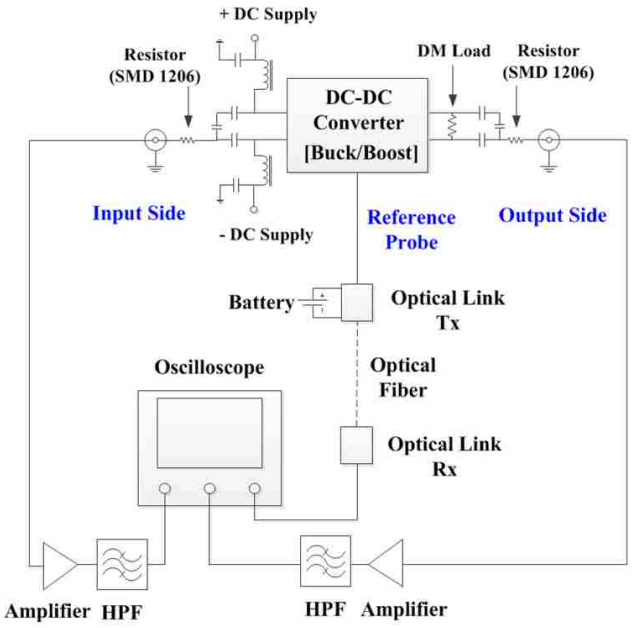

Figure 3.1 Schematic of the test setup used for terminal characterization of the DC-DC converters.

Each current probe output is passed via a first-order high pass filter that suppresses the otherwise dominating frequency components below 30 MHz to ensure sufficient dynamic range for measuring currents up to 250 MHz. An additional oscilloscope channel is used to measure the V_{DS} as a phase reference. A battery powered RF optical link was used for measuring the reference signal (V_{DS}) in the characterization setup to minimize the effect of the phase reference probing on any currents.

3.2 CHARACTERIZATION IMPEDANCES

As described earlier the characterization range is the range of common mode load variation on both input and output sides of the converter that are used to obtain the equivalent circuit model. The common mode load impedances on the input and output side of the converters determine the characterization range of the converters.

In the characterization board the common mode characterization and test impedances are implemented using resistive loads that are soldered between the measurement port and the DC-DC converter terminals. The input side and output side (load) side common mode impedances are measured using a Keysight® E5071C-285 [21] vector network analyzer (VNA). The measured input side and output side common mode load characterization load impedances used are shown in Figure 3.2 and 3.3 respectively. It can be observed that the impedances are different up to 250 MHz.

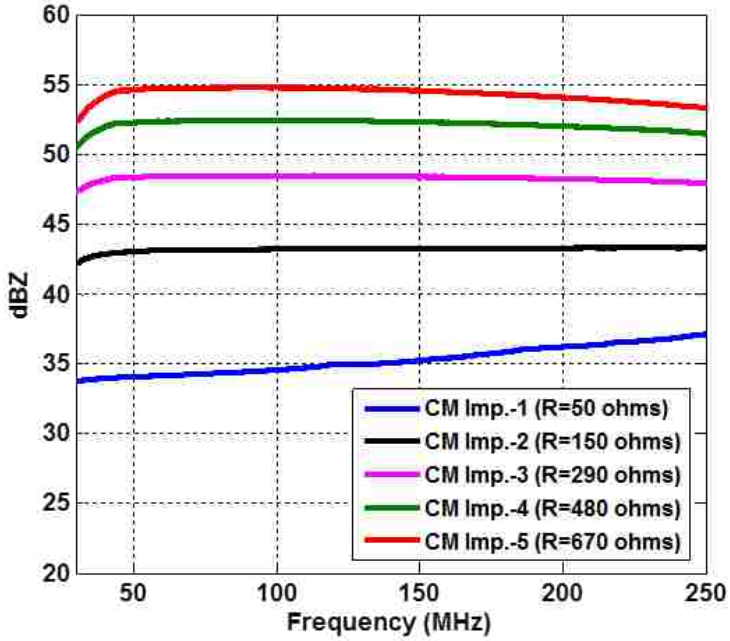

Figure 3.2 The measured common mode impedances on the input (LISN) side using different resistor values for the terminal characterization.

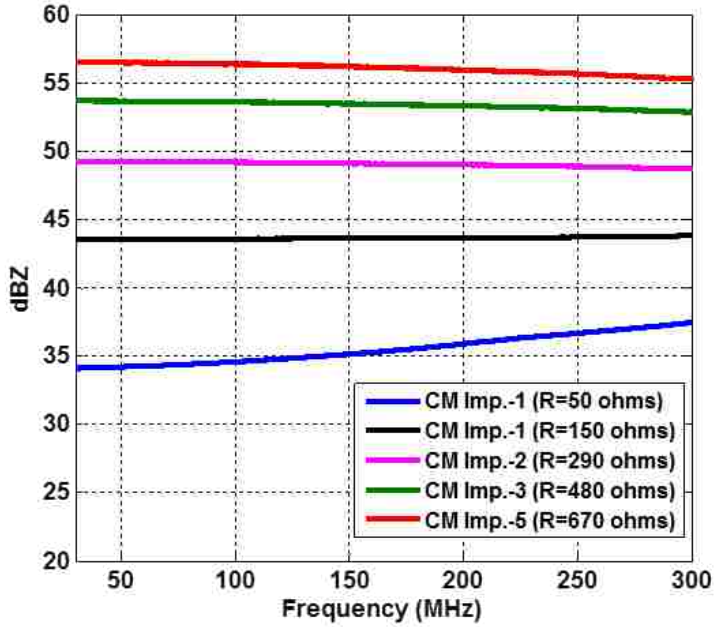

Figure 3.3 The measured common mode impedances on the output (LOAD) side using different resistor values for the terminal characterization.

3.3 METHODOLOGY FOR MAXIMIZED SPECTRUM MEASUREMENT FOR DC-DC CONVERTERS WITH STOCHASTIC BEHAVIOR

Since the common mode noise generated by the DC-DC converters is not purely a deterministic signal due to pulse-width modulation the phase difference between the reference channel and the common mode currents on the input and output side was obtained by averaging over multiple acquisitions or measurements [22]. The black-box representation of the DC-DC converter is shown in Figure 3.4 to explain the procedure for calculating the averaged and maximized spectrum envelope of the common mode currents.

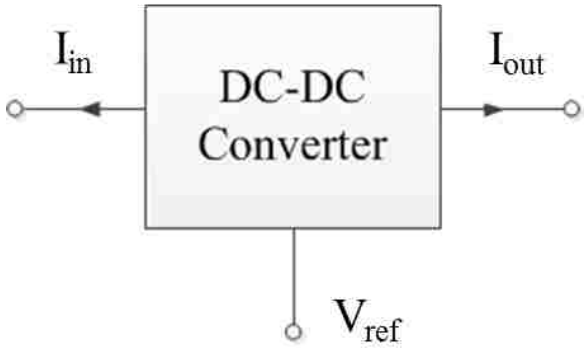

Figure 3.4 Black-box common mode model of DC-DC converter with input, output and reference terminals.

The input, output currents and reference signals measured by the oscilloscope are converted into frequency domain:

$$\left|V_{ref}\right|e^{j\varphi_O} = FFT(Vref) \qquad (2)$$

$$|I_O|e^{j\varphi_O} = FFT(I_{out}), \qquad (3)$$

The measurement is repeated multiple times to calculate the maximized spectrum envelope:

$$|I|_{max} = \max(|I_{out}|) \quad (4)$$

The averaged phase difference between common mode currents and the reference signal was calculated by

$$|Rout|e^{j\varphi_{iavg}} = mean(\frac{FFT(Iout)}{FFT(Vref)}) \quad (5)$$

$$Imax = |I|_{max}e^{j\varphi_{iavg}} \quad (6)$$

3.4 LOADING ON THE DC-DC CONVERTERS

The DC-DC converters are characterized by measuring the common mode currents for various characterization loads using the measurment setup described in section-III for a fixed DC power load. If the DC load is changed the characterization needs to be repeated.

4. SOURCE MODELS AND METHODOLOGY VALIDATION

In the proposed methodology, the fields are calculated using the geometry and the common mode currents driven by the extracted terminal model. As a non-linear circuit is approximated by a linear model it has to be investigated how the model reacts if a common mode load is provided that is outside the characterization range. To illustrate this, the example of the buck converter was selected. To validate the ability to predict the radiated emissions load impedance other than the values of the characterization impedances have been used. Test impedances that are within as well as that are outside the characterization range and are tested to validate the extracted the terminal source model. Data using the boost converter or different DC loads shows similar tendencies.

4.1 TEST IMPEDANCE WITHIN CHARACTERIZATION IMPEDANCE RANGE

The terminal equivalent model was extracted for the buck and boost converters by using the Load-1, Load-2 and Load-5 to predict the common mode currents for the test load impedance (Load-3), as shown in Figure 3.2 and 3.3, that is within the range of the characterization impedances. The comparison between the direct measurement of the common mode current and predicted using the terminal model for the buck and boost converter is shown in Figure 4.1 and 4.2 respectively. It can be seen that the agreement between the measured and predicted common mode currents, both on the input and output side, is within 5 dB across the measurement frequency band.

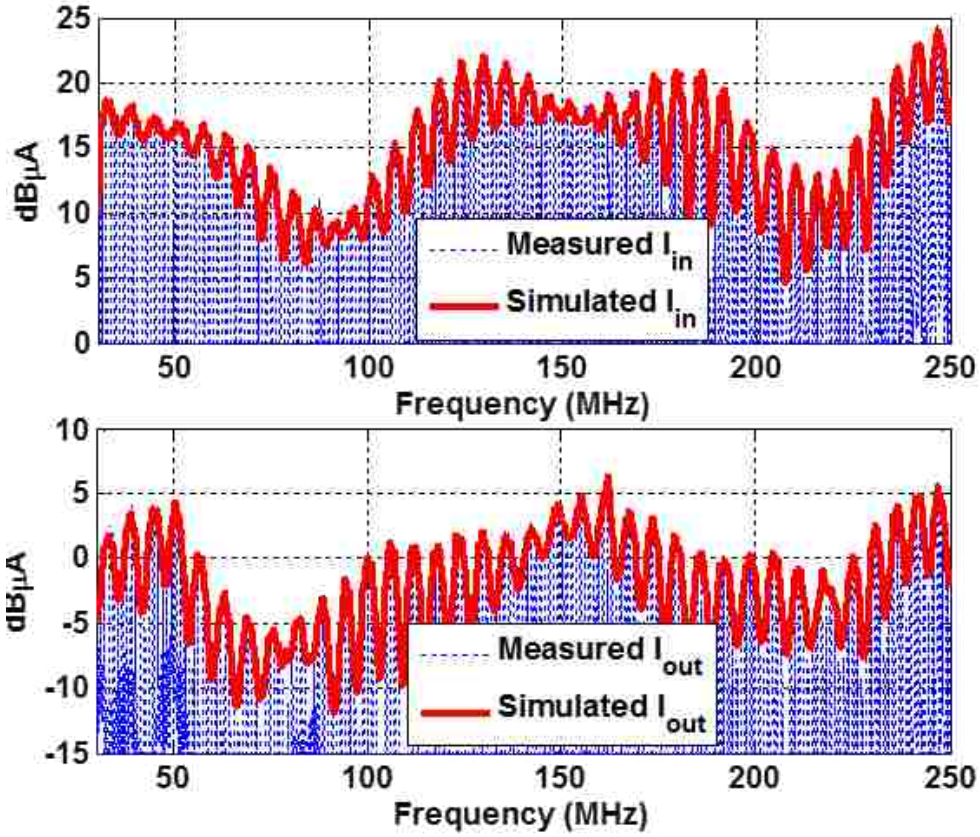

Figure 4.1 Comparison between the measured and predicted common mode current for the buck converter for a test impedance within the characterization range.

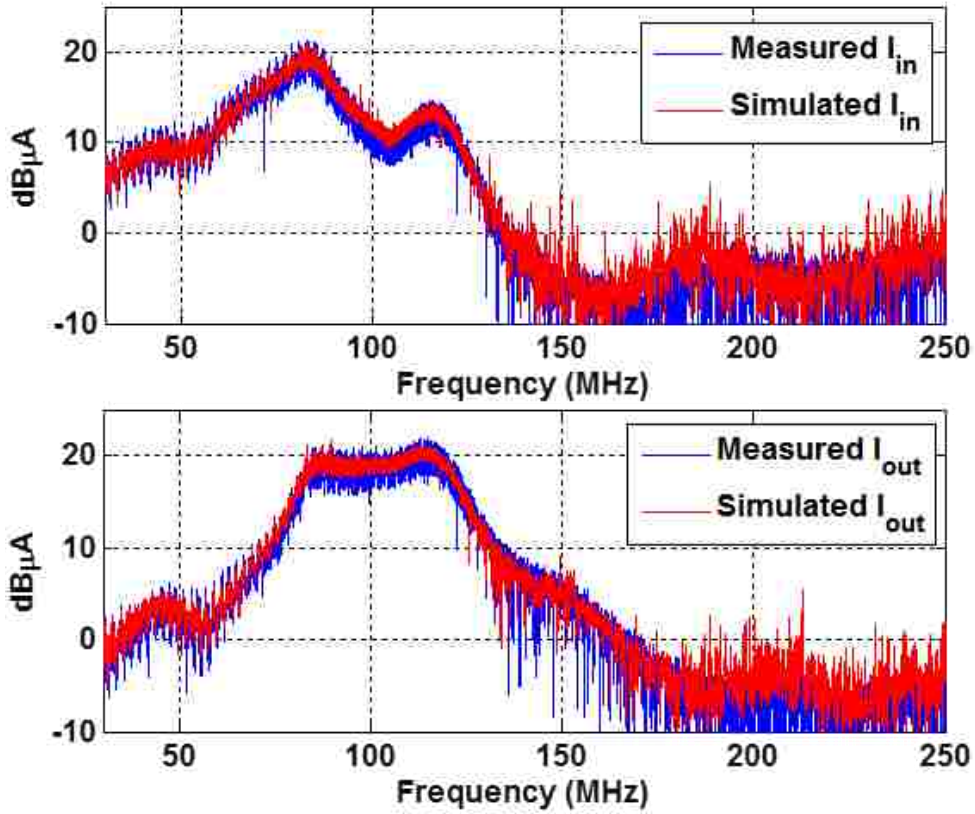

Figure 4.2 Comparison between the measured and predicted common mode current for the boost converter for a test impedance within the characterization range.

4.2 TEST IMPEDANCE OUTSIDE CHARACTERIZATION IMPEDANCE RANGE

The terminal equivalent model was extracted for the buck and boost converters by using the Load-1, Load-3 and Load-4 to predict the common mode currents for the test impedance (Load-5), as shown in Figure 3.2 and 3.3, that is outside the range of the characterization impedances. The comparison between the direct measurement of the common mode current and predicted using the terminal model for the buck and boost converter is shown in Figure 4.3 and 4.4 respectively. It can be seen that the agreement between the measured and predicted common mode currents, both on the input and

output side, is within 7 dB across the measurement frequency band as the power converter is a nonlinear circuit which is modelled by a linear equivalent circuit.

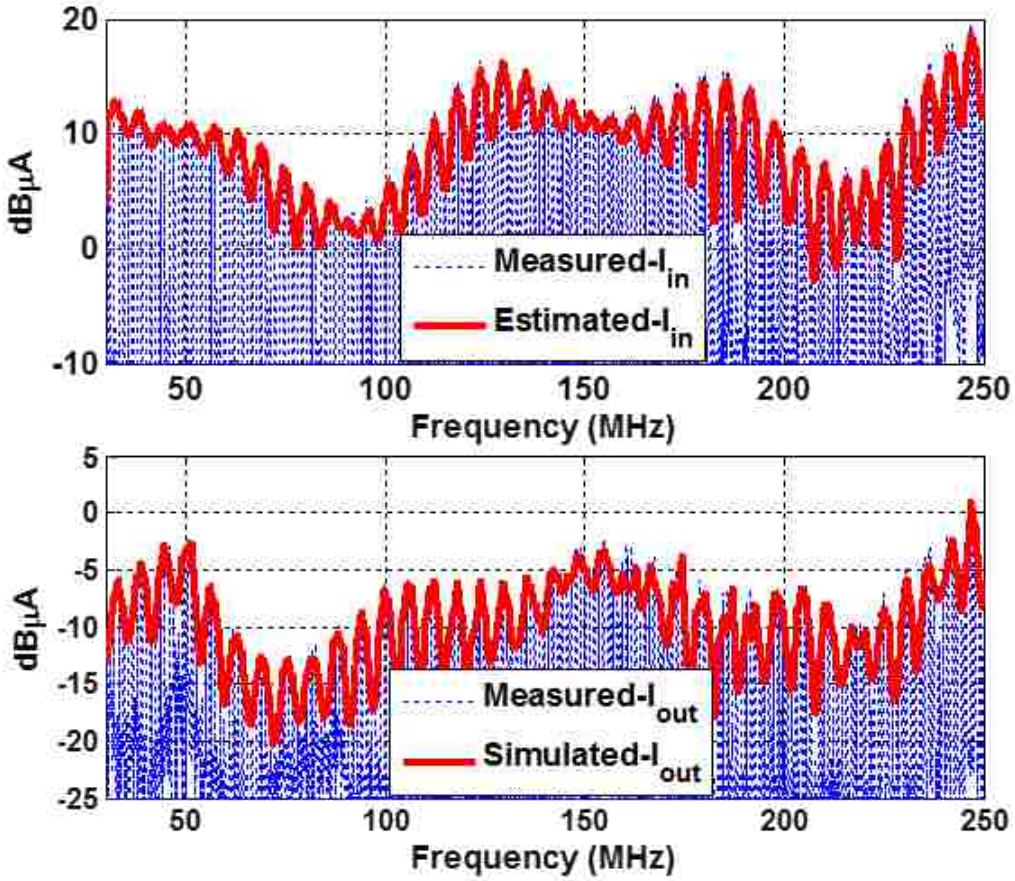

Figure 4.3 Comparison between the measured and predicted common mode current for the buck converter for a test impedance outside the characterization range.

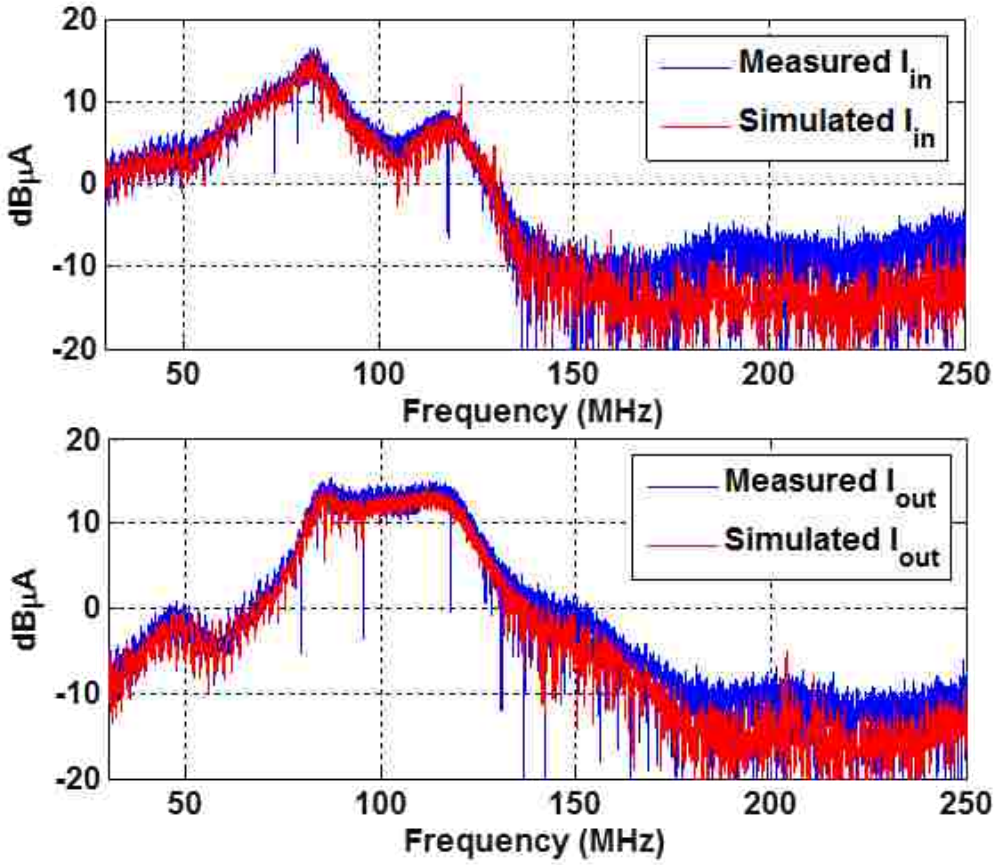

Figure 4.4 Comparison between the measured and predicted common mode current for the buck converter for a test impedance outside the characterization range.

5. RADIATED EMI PREDICTION USING FULL WAVE CO-SIMULATION

The goal of the methodology is the prediction of radiated emissions and describe the limitations of the method for application to a wide range of applications. As mentioned earlier in the steps for estimating the radiated emissions, the extracted linear terminal model is incorporated into the transfer function block of the full wave simulation model that comprises the common mode structures of the system to recalculate the radiated emissions at 1 m distance using the extracted sources and impedances as a post-processing step. As an example, the validation of the methodology to predict radiated fields is demonstrated for the setup shown in Figure 5.1 for two converters – buck and boost. The field is measured using a log-periodic antenna. The full wave simulation model consisting of the geometry of the setup and field probes that are positioned 1 m away from the edge of the metal reference plate is shown in Figure 5.2. It has been shown that simulating the field strength using field probes at the approximate phase center and applying the antenna factor for the measured results leads to acceptable results and avoids the complex simulation of the log-periodic antenna itself [23].

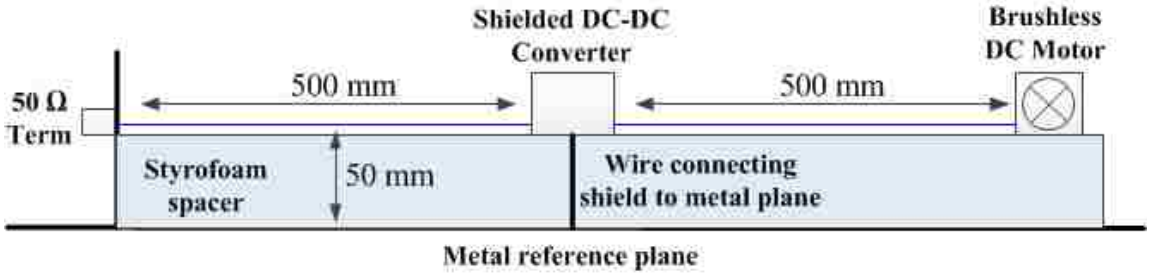

Figure 5.1 System test setup with brushless DC motor.

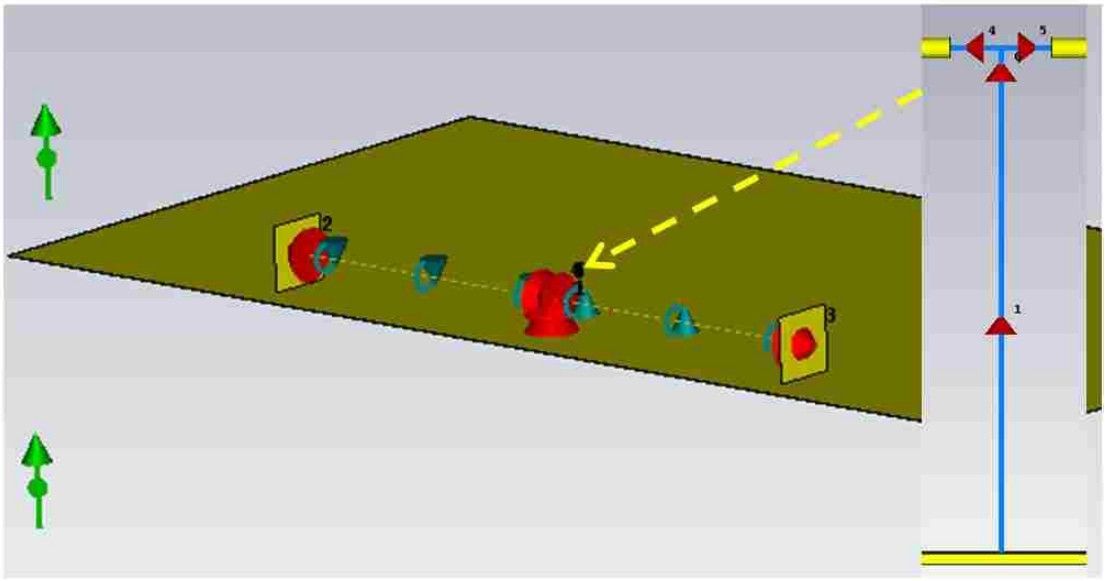

Figure 5.2 Full-wave simulation model of the common mode structure of the system.

The input side of the shielded converter is connected to a 0.5 m long twisted pair cable and to a 50 Ohm termination as the common mode impedance. The output side is connected via a 0.5 m long twisted pair to a brushless DC motor (computer fan). A comparison of the impedance looking into the 0.5 m long cable and the dc brushless motor from the converter's terminals is shown in Figure 5.3. The figure also includes the minimum and maximum values of characterization impedances to illustrate at which frequencies the actual load impedance is within and outside the characteration impedance range. It can be observed that the impedance of the 0.5 m cable and motor is within the characterization range in the frequency range 30 MHz to 90 MHz and 120 MHz – 200 MHz. The impedance is outside the characterization range from 90 MHz - 120 MHz and 200 MHz – 200 MHz. The comparison between the measured and simulated emissions in the frequency range 30 MHz – 250 MHz at 1 m antenna distance using the buck and boost converter is shown in Figure 5.4 and 5.5 respectively. It can be observed that the

predicted fields for the horizontal and vertical polarization are within 6 dB up to 220 MHz. In the frequency range 220 MHz – 250 MHz frequency range, the difference between estimated and measured emissions is about 8-10 dB. The larger difference in the predicted fields can be attributed to larger difference between the characterization impedance and the common mode impedances of the actual test setup. This is a consequence of modeling the non linear DC-DC converter by a linear model.

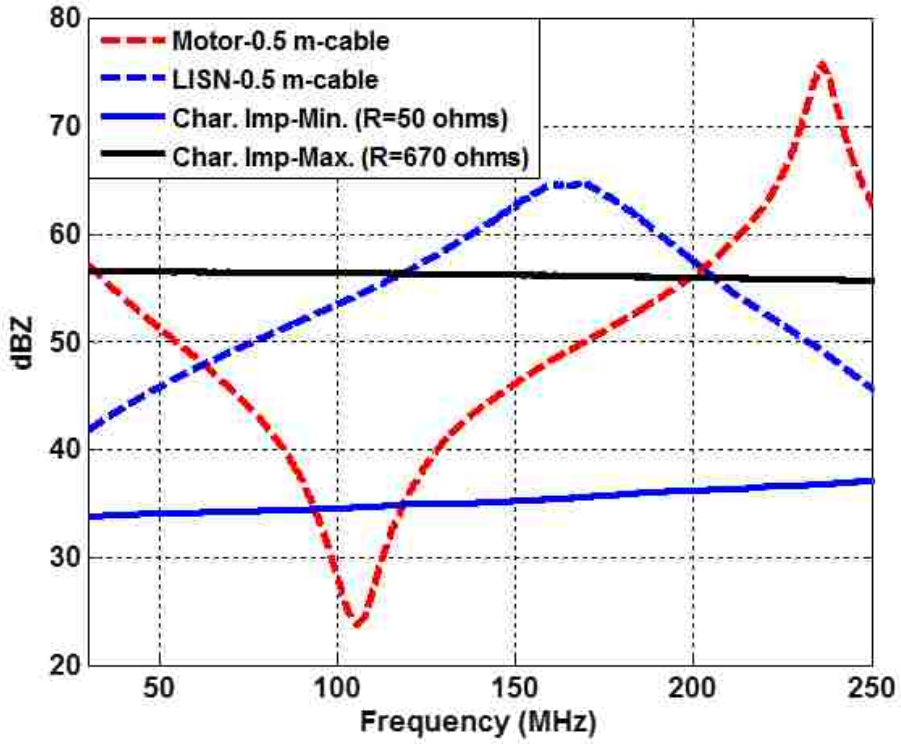

Figure 5.3 Comparison of the common mode impedance of the LISN and motor, placed 5 cm above the reference plate and the maximum and minimum characterization impedances.

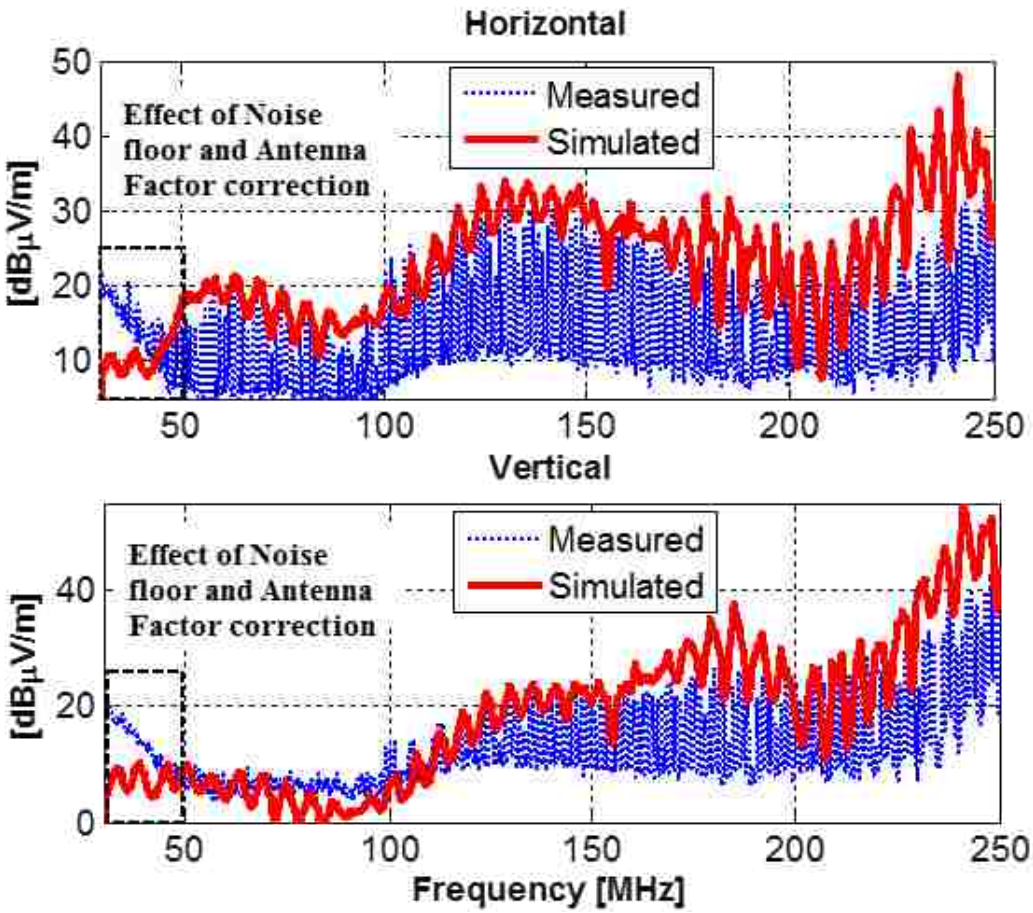

Figure 5.4 Comparison between the measured and simulated radiated EMI from the setup with the shielded buck converter circuit.

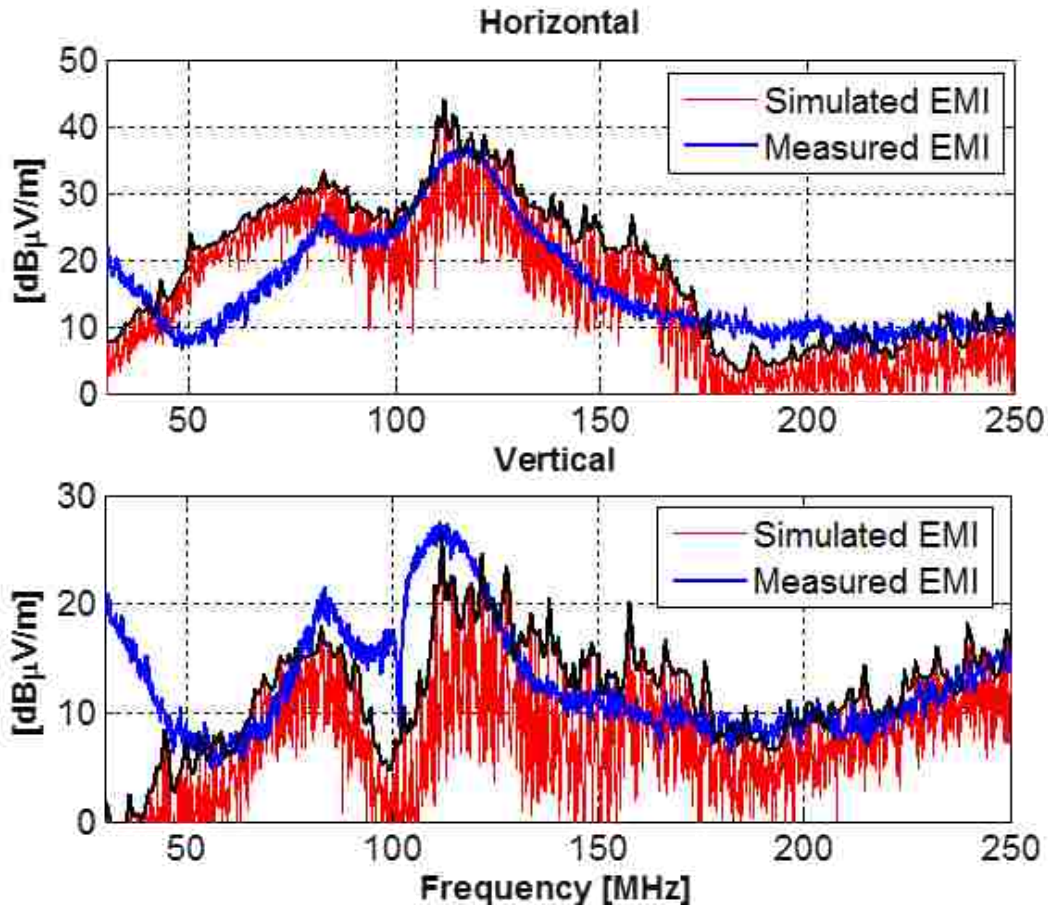

Figure 5.5 Comparison between the measured and simulated radiated EMI from the setup with the shielded boost converter circuit.

6. CONCLUSION

A methodology for the prediction of radiated emissions from shielded DC-DC converters with attached cables using a terminal equivalent model is presented. The maximized spectrum of the common mode currents is also extracted for converters with stochastic signals using a novel characterization procedure. The proposed method offers advantages over existing prediction models that require accurate modeling of circuit parasitics, complex physics based component models, extraction of PCB parasitics and computationally expensive time domain simulations. The non-linear behavior of the DC-to-DC converters is substituted with a linear model based on measured common mode currents corresponding to various common mode impedances at the terminals of the converters.

Results show that the terminal equivalent circuit model can predict the radiation providing that the actual loads are within the range of impedances used to characterize the converter. For the specific example the prediction was within 6 dB in the frequency range 30 MHz – 220 MHz under the condition that the characterization impedances are close to the impedance of the real system. Limitations of the terminal equivalent modeling include (1) direct radiation from the converters cannot be modeled, (2) the accuracy of the prediction depends on the common mode impedances of the real system/application and the characterization impedances, (3) a characterization test setup is required.

7. ACKNOWLEDGEMENTS

This material is based upon work supported by the National Science Foundation (NSF) under Grants IIP-1440110.

REFERENCES

[1] Shuo Wang, F.C. Lee, D.Y. Chen and W.G. Odendaal, “Effects of Parasitic Parameters on the Performance of EMI Filters,” Power Electronics, IEEE Transactions, Volume 19, Issue 3, May. 2004, pp. 869 –877.

[2] Z. Huibin, L. Jih-Sheng, A. R. Hefner Jr., T. Yuqing, and C. Chingchi, “Analysis of conducted EMI emissions from PWM inverter based on empirical models and comparative experiments,” in Proc. IEEE Power Electron. Spec. Conf., 1999, vol. 862, pp. 861–867.

[3] P.Xuejun, Z. Kai, K.Yong, and C. Jian, “Analytical estimation of common mode conducted EMI in PWM inverter,” in Proc. Conf. Rec. IEEE IAS Annu. Meeting, 2004, vol. 4, pp. 2651–2656.

[4] Natalia Bondarenko, et. al., “A Measurement-Based Model of the Electromagnetic Emissions from a Power Inverter”, IEEE Transactions on Power Electronics”, p-p 1, December, 2014.

[5] X. Pei, K. Zhang, Y. Kang, and J. Chen, “Prediction of common mode conducted EMI in single phase PWM inverter,” in Proc. IEEE Power Electron. Spec. Conf. (PESC’04), Aachen, Germany, Jun. 20 25, 2004, pp. 3060–3065.

[6] A. Farhadi, "Modeling, Simulation, and Reduction of Conducted Electromagnetic Interference Due to a PWM Buck Type Switching Power Supply," 13th Harmonics and Quality of Power Conf. Proc., Wollongong, NSW, 2008, pp.1-7.

[7] Henglin Chen, et al., “Determining Far-Field EMI From Near-Field Coupling of a Power Converter”, IEEE Transactions on Power Electronics, October 2014.

[8] Hyun Ho Park, et al., “A Simple Method of Estimating the Radiated Emission From a Cable Attached to a Mobile Device”, IEEE Transactions on Electromagnetic Compatibility, April 2013.

[9] Kohji Sasabe, et al., A simple method for predicting common-mode radiation from a cable attached to a conducting enclosure”, Proceedings of APMC 2001, Taipei.

[10] I. F. Kovacevic, T. Friedli, A. M. Muesing, and J. W. Kolar, “3-D electromagnetic modeling of EMI input filters,” IEEE Trans. Ind. Electron., vol. 61, no. 1, pp. 231–242, Jan. 2014.

[11] I. F. Kovacevic, T. Friedli, A. M. Musing, and J. W. Kolar, “3-D electromagnetic modeling of parasitics and mutual coupling in EMI filters,” IEEE Trans. Power Electron., vol. 29, no. 1, pp. 135–149, Jan. 2014.

[12] H. Bishnoi, P. Mattavelli, R. Burgos, and D. Boroyevich, "EMI Behavioral Models of DC-Fed Three-Phase Motor Drive Systems," Power Electronics, IEEE Transactions on, vol. 29, pp. 4633-4645, 2014.

[13] H. Bishnoi, A. C. Baisden, P. Mattavelli, and D. Boroyevich, “Analysis of EMI terminal modeling of switched power converters,” IEEE Trans. Power Electron., vol. 27, no. 9, pp. 3924–3933, Sep. 2012

[14] Q. Liu, F. Wang, and D. Boroyevich, "Modular-terminal-behavioral (MTB) model for characterizing switching module conducted EMI generation in converter systems," IEEE Trans. on Power Electronics, vol.21, no.6, pp.1804-1814, Nov.2006.

[15] Q. Liu, F. Wang, and D. Boroyevich, "Conducted-EMI Prediction for AC Converter Systems Using an Equivalent Modular-Terminal- Behavioral (MTB) Source Model," Industry Applications, IEEE Transactions on, vol. 43, pp. 1360-1370, 2007.

[16] G. Shen, V. Khilkevich, D. Pommerenke, C. Keller, H. Aichele, B. Martin “Terminal model application for characterizing conducted EMI in boost converter system”, IEEE Int. Symp. On EMC, Ottawa, August 2016.

[17] S. Shinde, A. Patnaik, T. Makharashvili, K. Masuda, D. Pommerenke, “Common Mode Current Prediction from a Power Converter with Attached Cables based on a Terminal Equivalent Circuit Model”, IEEE Int. Symp. On EMC, Ottawa, August 2016.

[18] International Standards, CISPR 16: Specification for Radio Disturbance and Immunity Apparatus and Methods, 1993.

[19] European Standards, EN55011: Limits and Methods of Measurement of Radio Disturbance Characteristics of Industrial, Scientific and Medical (ISM) Radio Frequency Equipment, 1991.

[20] International Standards, IEC22G (draft): EMC Product Standard—Including Specific Test Methods for Power Drive Systems, 1995.

[21] Keysight® E5071C-285 manual.
Available: http://cp.literature.agilent.com/litweb/pdf/5989-5478EN.pdf

[22] Shen, G; Khilkevich, V.V.; Pommerenke, "Terminal Modeling of DC-DC Converters with Stochastic Behavior," submitted to IEEE Transactions on. Electromagnetic Compatibility.

[23] S. Shinde, X. Gao, K. Masuda, V.V. Khilkevich, D. Pommerenke, "Modeling EMI Due to Display Signals in a TV", *IEEE Transactionson Electromagnetic Compatibility*, no. 99, pp. 1-10.

SECTION

2. CONCLUSIONS

This dissertation consists of four papers, which cover emissions modeling for a complex electronic product, the design and an equivalent circuit model for a frequency tunable H-field probe, measurement method for rapid detection of dissimilar and aging ICs and radiated emissions prediction using terminal equivalent modeling.

In the first paper, a combined model for predicting the most critical radiated emissions and total radiated power due to the display signals in a TV by incorporating the main processing board using the Huygens Equivalence theorem and the radiation due to the flex cable based on active probe measurements was developed.

In the second paper, a frequency-tunable resonant magnetic field probe was designed in the frequency range 900-2260 MHz for near-field scanning applications for the radio frequency interference studies by using a varactor diode providing the required capacitance and the parasitic inductance of a magnetic field loop (i.e., a parallel *LC* circuit). The measured frequency response and sensitivity over a microstrip trace using the fabricated probe showed good agreement with the simulated results of the equivalent circuit model and the full-wave simulation model.

In the third paper, a wideband microwave method was developed as a means for rapid detection of slight dissimilarities (including counterfeit) and aging effects in integrated circuits (ICs) based on measuring the complex reflection coefficient of an IC when illuminated with an open-ended rectangular waveguide probe, at K-band (18-26.5 GHz) and Ka-band (26.5-40 GHz) microwave frequencies.

In the fourth paper, a method to predict radiated emissions from DC-DC converters with cables attached on the input side to a LISN and on the output side to a DC brushless motor as load based on linear terminal equivalent circuit modeling was demonstrated. The linear terminal equivalent model was extracted using measured input and output side common mode currents for various characterization impedances connected at the input and output terminals of the converter.

VITA

Satyajeet Shinde was born in India, 1988. He received his B.E. degree in Electronics and Telecommunications Engineering, in 2010, from the University of Pune, India. From 2010 to 2011, he was a Programmer Analyst Trainee in the Communications Testing Division, Cognizant, India. Since 2011, he has been a Graduate Research Assistant in the Electromagnetic Compatibility Laboratory, Missouri University of Science and Technology. He received his M.S. degree in Electrical Engineering from the Missouri University of Science and Technology in Jan 2014. He received his PhD degree in Electrical Engineering from the Missouri University of Science and Technology in May 2017. He was a Signal Integrity summer intern (2013) at Micron Technology, Boise, ID and EMC Design summer intern (2015) at Apple Inc., Cupertino, CA. His research interests included intra-system RFI, radiated emission modeling techniques, EMC and ESD measurement methods and RF system design.